



University of Kentucky  
UKnowledge

---

Theses and Dissertations--Earth and  
Environmental Sciences

Earth and Environmental Sciences

---


2023

## Applications of Digital Terrain Modeling to Address Problems in Geomorphology and Engineering Geology

Sarah Johnson

University of Kentucky, johnsonsa39@gmail.com

Author ORCID Identifier:

 <https://orcid.org/0000-0001-7335-4959>

Digital Object Identifier: <https://doi.org/10.13023/etd.2023.167>

[Right click to open a feedback form in a new tab to let us know how this document benefits you.](#)

### Recommended Citation

Johnson, Sarah, "Applications of Digital Terrain Modeling to Address Problems in Geomorphology and Engineering Geology" (2023). *Theses and Dissertations--Earth and Environmental Sciences*. 99.  
[https://uknowledge.uky.edu/ees\\_etds/99](https://uknowledge.uky.edu/ees_etds/99)

This Doctoral Dissertation is brought to you for free and open access by the Earth and Environmental Sciences at UKnowledge. It has been accepted for inclusion in Theses and Dissertations--Earth and Environmental Sciences by an authorized administrator of UKnowledge. For more information, please contact [UKnowledge@lsv.uky.edu](mailto:UKnowledge@lsv.uky.edu).

## **STUDENT AGREEMENT:**

I represent that my thesis or dissertation and abstract are my original work. Proper attribution has been given to all outside sources. I understand that I am solely responsible for obtaining any needed copyright permissions. I have obtained needed written permission statement(s) from the owner(s) of each third-party copyrighted matter to be included in my work, allowing electronic distribution (if such use is not permitted by the fair use doctrine) which will be submitted to UKnowledge as Additional File.

I hereby grant to The University of Kentucky and its agents the irrevocable, non-exclusive, and royalty-free license to archive and make accessible my work in whole or in part in all forms of media, now or hereafter known. I agree that the document mentioned above may be made available immediately for worldwide access unless an embargo applies.

I retain all other ownership rights to the copyright of my work. I also retain the right to use in future works (such as articles or books) all or part of my work. I understand that I am free to register the copyright to my work.

## **REVIEW, APPROVAL AND ACCEPTANCE**

The document mentioned above has been reviewed and accepted by the student's advisor, on behalf of the advisory committee, and by the Director of Graduate Studies (DGS), on behalf of the program; we verify that this is the final, approved version of the student's thesis including all changes required by the advisory committee. The undersigned agree to abide by the statements above.

Sarah Johnson, Student

Dr. William C. Haneberg, Major Professor

Dr. Micheal McGlue, Director of Graduate Studies



APPLICATIONS OF DIGITAL TERRAIN MODELING TO ADDRESS PROBLEMS  
IN GEOMORPHOLOGY AND ENGINEERING GEOLOGY

---

DISSERTATION

---

A dissertation submitted in partial fulfillment of the  
requirements for the degree of Doctor of Philosophy in the  
College of Arts and Sciences  
at the University of Kentucky

By

Sarah Evelyn Johnson

Lexington, Kentucky

Director: Dr. William C. Haneberg, Professor of Earth and Environmental Sciences

Lexington, Kentucky

2023

Copyright © Sarah Johnson 2023  
<https://orcid.org/0000-0001-7335-4959>

## ABSTRACT OF DISSERTATION

### APPLICATIONS OF DIGITAL TERRAIN MODELING TO ADDRESS PROBLEMS IN GEOMORPHOLOGY AND ENGINEERING GEOLOGY

This dissertation uses digital terrain modeling and computational methods to yield insight into three topics: 1) evaluating the influence of glacial topography on fluvial sediment transport in the Teton Range, WY, 2) integrating regional airborne lidar, UAV lidar, and structure from motion photogrammetry to characterize decadal-scale movement of slow-moving landslides in northern Kentucky, and 3) applying machine learning methods to surficial geologic mapping.

The role of topography as a boundary condition that controls the efficiency of fluvial erosion in the Teton Range, Wyoming, was investigated by using existing lidar data to delineate surficial geologic units, geometrically reconstruct the depth to bedrock, and estimate the sediment volume and sediment production rate in two catchments. This data was coupled with seismic reflection data in the bay into which these catchments drain. We found that while the sediment production rate of  $0.17 \pm 0.02$  mm/yr is similar to the uplift rate of the Teton Range, only about 2.6% of the post-glacial sediment has been transported out of the catchments, and the denudation rate is just  $0.004 \pm 0.001$  mm/yr. We conclude that once the topography has been altered by glaciers, which flatten the valley bottom and steepen the valley walls, rivers are incapable of evacuating the sediment effectively. Sediment will be trapped in the valleys until the next glacial advance, or until uplift steepens the system such that rivers can once again become efficient.

Repeat digital terrain surveys can be used to quantify changes to the Earth's surface. Challenges include determining the threshold of change that can be detected when combining topographic data acquired by different platforms and of varying quality. To quantify the threshold of detectable elevation change in a slow-moving colluvial landslide in northern Kentucky over 14 years using county-wide lidar, uncrewed aerial vehicles

(UAV) structure from motion surveys (SfM) and a UAV lidar survey, we used the statistics of noise from elevation difference maps in areas outside of the landslide. We found that the threshold of detectable elevation change ranges from 0.05 to 0.20 m, depending on the survey combination, and that detectable change in the landslide was found between all surveys, including those separated by only 2 weeks.

For most users, geologic maps may convey a level of certainty which obscures the decisions and interpretations made by the mapper. The combination of machine learning and digital terrain data provides a new method for producing geologic maps which can also convey and preserve the underlying uncertainty. We test the performance of machine learning methods to accurately map the surficial geology of two quadrangles in Kentucky using 31 variables derived from lidar data, including surface roughness, slope, topographic position, and residual topography. The performance of eight machine learning methods were compared, and the importance of each variable was measured. The classifier with the highest accuracy using just the most important variables was used to produce surficial geologic maps in 6 areas, with resulting accuracies ranging from 0.795 to 0.931. The uncertainty resulting from the machine learning process is conveyed using gradations of color, which can be modified depending on the needs of the map user.

**KEYWORDS:** Digital terrain modeling, change detection, landslides, machine learning, geologic mapping, sediment budget

---

Sarah E. Johnson

---

03/08/2023

---

APPLICATIONS OF DIGITAL TERRAIN MODELING TO ADDRESS PROBLEMS  
IN GEOMORPHOLOGY AND ENGINEERING GEOLOGY

By  
Sarah Evelyn Johnson

William C. Haneberg

---

Director of Thesis

Michael M. McGlue

---

Director of Graduate Studies

03/06/2023

---

Date

## ACKNOWLEDGMENTS

When I first started at UK, my advisor Bill Haneberg said that getting a PhD should be a life-changing experience, and I can affirm that it has been. Not only did I find research that I truly enjoy, but I have made new colleagues, collaborators, and friends along the way.

I would like to thank my committee members, Bill Haneberg, Ryan Thigpen, Ed Woolery and Sebastian Bryson. It has been a privilege and a pleasure to work with each of them. Not only have they mentored me as a researcher and inspired me to do my best possible work, but they have also helped me negotiate the publication process, navigate academia, and persevere through setbacks. They have demonstrated how to inspire research teams, pursue big ideas, and have modeled leadership in the field, the Earth and Environmental Science department and the Kentucky Geological Survey. They have shown that humor and kindness compliment rigor and excellence.

I would like to thank the Kentucky Geological Survey and the University of Kentucky Earth and Environmental Sciences Department faculty, staff, and graduate students. I would particularly like to thank Matt Crawford for his contributions to the landslides research in Kentucky; Jason Dortch and Sean Gallen for coaching me to think like a geomorphologist; and Mike McGlue for showing me the ropes on Jackson Lake. I thank my fellow students Meredith Swallom, Brandon Spencer, Autumn Helfrich, and Ryan Goldsby for making three Tetons field seasons productive, memorable, and fun. I am immensely grateful for the support of the KGS EES Research Assistantship in Earth and Environmental Sciences, and for the Ferm and Brown-McFarland funds to fund field work and present research.

Finally, I would like to thank my family, Eric, Sam, and Claire Evans for their patience and love as I worked towards this degree. I would like to thank my mother Nina for inspiring me to be a life-long learner, my father Bob who I know would be so proud of me, and my sisters Glenna and Olivia for their wholehearted encouragement.

## TABLE OF CONTENTS

APPLICATIONS OF DIGITAL TERRAIN MODELING TO ADDRESS PROBLEMS IN GEOMORPHOLOGY AND ENGINEERING GEOLOGY .....	i
ABSTRACT OF DISSERTATION .....	i
ACKNOWLEDGMENTS .....	iii
TABLE OF CONTENTS .....	iv
LIST OF TABLES .....	viii
LIST OF FIGURES .....	ix
CHAPTER 1. THE INFLUENCE OF GLACIAL TOPOGRAPHY ON FLUVIAL EFFICIENCY IN THE TETON RANGE, WYOMING .....	1
1.1    Abstract.....	1
1.2    Introduction .....	1
1.2.1    Geologic Setting .....	3
1.3    Methods .....	4
1.3.1    Moran Bay seismic acquisition and sediment volume estimate .....	4
1.3.2    Geomorphologic map .....	4
1.3.3    Canyon sediment volume estimates derived from modeled bedrock DEM ....	4
1.3.4    Canyon sediment volume estimates derived from colluvial sediment production rate.....	5
1.3.5    Canyon sediment volume estimates derived from assigned thickness .....	5
1.3.6    Porosity estimates .....	7
1.3.7    Monto Carlo simulation for rock volume and erosion rate calculations .....	7
1.4    Results .....	7
1.4.1    Geomorphologic mapping of Moran and Snowshoe Canyons .....	7
1.4.2    Moran Bay seismic reflection profiling.....	11
1.4.3    Estimates of sediment volume, post-glacial sediment production, and erosion rates.....	13
1.5    Discussion.....	15
1.5.1    Moran Bay impoundment timing, geometry, and sedimentation history .....	15
1.5.2    Sediment production and erosion rate .....	15
1.5.3    Landscape, process, and equilibrium.....	17
1.5.4    Post-glacial landscape longevity .....	19

1.6	Conclusions .....	19
1.7	Acknowledgements .....	20
CHAPTER 2. MEASURING GROUND SURFACE ELEVATION CHANGES IN A SLOW-MOVING COLLUVIAL LANDSLIDE USING COMBINATIONS OF REGIONAL AIRBORNE LIDAR, UAV LIDAR, AND UAV PHOTOGRAMMETRIC SURVEYS 21		
2.1	Abstract.....	21
2.2	Introduction .....	21
2.2.1	Landslide Characteristics and Geologic Setting.....	23
2.3	Methods .....	25
2.3.1	Change Detection .....	25
2.3.2	Data Acquisition .....	27
2.3.3	Data Processing .....	28
2.3.4	Noise Maps .....	29
2.3.5	Correction for bias and tilt.....	29
2.3.6	Threshold of elevation change detection.....	30
2.3.6.1	Method I: difference map errors.....	31
2.3.6.2	Method II: individual DEM errors .....	31
2.3.7	Magnitude of vertical change .....	32
2.4	Results .....	32
2.4.1	DEM Corrections.....	32
2.4.2	Threshold of Detectable Change .....	33
2.4.3	Vertical Changes in the Landslide Surface .....	35
2.5	Discussion.....	38
2.5.1	Threshold of detection .....	38
2.5.2	Landslide deformation.....	40
2.5.3	Landslide signature.....	42
2.5.4	Thermal Expansion and Contraction .....	43
2.5.5	Influence of Vegetation .....	43
2.5.6	Spatial variability of uncertainty .....	44
2.6	Conclusions .....	44
2.7	Acknowledgments .....	45
CHAPTER 3. MACHINE LEARNING FOR SURFICIAL GEOLOGIC MAPPING ....46		
3.1	Abstract.....	46
3.2	Introduction .....	46
3.3	Geologic Setting .....	49
3.4	Methods .....	50

3.4.1	Overview .....	50
3.4.2	Surficial geologic quadrangles .....	51
3.4.3	Digital elevation maps and derivative maps.....	52
3.4.4	Geologic classes .....	53
3.4.5	Machine Learning Methods.....	54
3.4.6	Variables & dimensionality reduction.....	55
3.4.7	Quantifying model performance.....	56
3.4.8	Lithologic probability maps .....	56
3.5	Results .....	57
3.5.1	Model Accuracy and F1 scores .....	57
3.5.2	Variable Importance .....	59
3.5.3	Probability maps & F1 scores.....	60
3.5.3.1	Pitts Point.....	60
3.5.3.2	De Mossville.....	65
3.6	Discussion.....	69
3.6.1	Model performance .....	69
3.6.2	Strengths and Limitations of Machine Learning.....	69
3.6.2.1	Class imbalance .....	69
3.6.2.2	Ease of classification .....	70
3.6.2.3	Topographic control .....	70
3.6.3	ML performance inside and out of training area .....	70
3.6.4	Mapping uncertainty.....	71
3.6.5	Can ML replace human mapping? .....	71
3.6.6	Future directions .....	72
3.7	Conclusions .....	72
3.8	Acknowledgments .....	72
REFERENCES .....		73
VITA.....		87
Education .....		87
Professional Experience .....		87
Refereed Papers Published .....		87
Published Conference Abstracts.....		88
Other Presentations.....		90
Academic Scholarships & Honors.....		90





## LIST OF TABLES

Table 1.1 Moran Bay gravity core and lake bottom sample locations and descriptions. .	13
Table 1.2 Summary of area and sediment volume calculations in Moran Canyon, Snowshoe Canyon and Moran Bay. Volume analysis is based on a combination of the modeled bedrock DEM analysis, sediment production rate of colluvium and assigned thicknesses based on landform observations. ....	14
Table 2.1 Methods and dates of data acquisition. ....	28
Table 2.2 Results of noise analysis and the thresholds of elevation change detection prior to and after corrections using Method I and Method II, and the sum of elevation change in the landslide for each survey combination. Each DEM was corrected for tilt or bias so that areas outside of the landslide matched the 2012 county-wide lidar DEM. The first DEM column is the older dataset, and the second DEM is the more recent dataset. ....	33
Table 3.1 Definition of variables. ....	53
Table 3.2. Simplified lithological categories. ....	54
Table 3.3. Description of different ML models. ....	55
Table 3.4. F1 scores for each lithologic class for the Pitts Point quadrangle, and the overall accuracy for each machine learning model. ....	58
Table 3.5. F1 scores for each lithologic class for the De Mossville quadrangle, and the overall accuracy for each machine learning model. ....	58
Table 3.6. F1 scores for each class and overall accuracy results for the maps in the Pitts Point Quadrangle. ....	62
Table 3.7. F1 scores for each class and overall accuracy results for the maps in the De Mossville Quadrangle. ....	65

## LIST OF FIGURES

Figure 1.1 a) Regional map of the Teton Range which lies at the eastern edge of the Basin and Range in northwestern Wyoming. Displacement along the Teton normal fault that bounds the eastern side of the range has produced an asymmetric uplift that dips to the west. b) Moran and Snowshoe Canyons drain into Moran Bay, the westernmost portion of Jackson Lake. The terminal moraine formed by the Pinedale glacial advance ( $14.4 \pm 0.8$ ka) impounded Jackson Lake. ....	3
Figure 1.2 a) Thirty-three cross sections in the Moran catchment were used to project the bedrock surface under the sediment. Four CHIRP seismic profiles (D19, D14W, D15W and S0S) were used to estimate the volume of sediment derived from the Moran and Snowshoe catchments, and lake bottom samples and gravity cores were used to support the seismic interpretation. b) Example of bedrock surface produced in MATLAB using elevations of exposed bedrock along the valley walls to project the bedrock surface under the sediment. ....	6
Figure 1.3. Geomorphologic map of the Moran and Snowshoe catchments. The base map is a hillshade map derived from LiDAR flown in 2014. Callouts show examples of talus cones, debris fans, alluvium, glacial drift, a rock glacier, and a roche moutonnée. ....	8
Figure 1.4. Examples of landforms in the Teton Range: a) view of Moran and Snowshoe Canyons from Moran Bay, b) view of Mt. Moran, Triple Glaciers, debris fan, talus cones and a roche moutonnée in Moran Canyon, c) alluvium in a glacially-flattened valley, d) talus cones, e) view from Moran Canyon of Moran Bay and the moraine that isolates it from Jackson Lake. ....	9
Figure 1.5. Stream profiles and geomorphic units along major tributary valleys of the Moran and Snowshoe catchments. Geomorphic units in contact with the valley bottom are shown, but depths are not implied. ....	10
Figure 1.6. CHIRP seismic profiles and maps of Moran Bay. a) Seismic profile D19 showing Moran Bay is isolated from the main depocenter of Jackson Lake by a submerged bathymetric ridge. b) Moran Bay seismic profile with locations of lake bottom samples and gravity cores. c) Interpretation of the seismic profile. d) Paleobathymetric map of Moran Bay based on horizon A, the Pinedale moraine. e) Map showing the horizontal extents of horizons B and C, and the locations of seismic lines, short cores and lake bottom samples. ....	12
Figure 1.7. Erosion rates of fluvial, glacial and paraglacial catchments from Koppes and Montgomery (2009), Church and Slaymaker (1989) and Dietch et al. (2015). The erosion rate of Moran Bay of $0.004 \pm 0.001$ mm/yr plots within the typical range for small paraglacial catchments. ....	18
Figure 2.1. Location of the Taylor Mill landslide study area in northern Kentucky (39.034234, -84.512587). Cincinnati, Ohio, lies directly across the Ohio River from the study area. ....	23

Figure 2.2. Landslide in Taylor Mill, Kentucky. Oblique view of slide generated from March 11, 2019 drone UAV imagery. The scarp has exposed the road foundation, and the toe has advanced into the road leading to an apartment complex. The two-lane road is approximately 6 metres wide. Photo of the scarp was taken April, 2018; photo of the toe was taken March, 2022. ....24

Figure 2.3. Sequence of images that illustrate the changes to the slope between 2000 and 2021 (Google Earth 2000, 2005, 2006, 2008, 2010, 2021). a) Image from October 2000 showing the driveway and vegetated slope. b) Image from August 2005 showing some bare patches on the previously vegetated slope. c) Image from June 2006 showing the regraded slope. d) Image from 2008 showing a bare patch at the top of the slope that may represent added fill. e) Image from July 2010 showing added fill and the reconstructed driveway at the top of the slope. f) image from March 2021 showing drainage from the toe of the landslide into the driveway.....25

Figure 2.4. The flowchart summarizing the data acquisition and processing of the county-wide lidar, UAV-SfM imagery, and UAV-lidar; the corrections to the DEMs for bias and tilt; and the methods used to estimate the threshold of detectable change. ....27

Figure 2.5. An illustration of the two methods to estimate the threshold of detectable change. (a) Method I uses the propagated errors from the difference map to estimate the threshold. (b) Method II uses an estimate of the individual DEM errors to calculate the threshold value that must be exceeded for the overlap between the two individual DEM error distributions to remain below a specified probability.....31

Figure 2.6. Examples of noise maps and noise distributions in no-change areas above and below the landslide before and after corrections for bias and tilt. (a) Noise map and distribution showing bias between the 2012 county-wide lidar DEM and the 2021 UAV-lidar DEM. (b) Noise map and distribution after the correction. Note there is still noise in the vegetated areas below the slide, and linear features in the mowed grassy area on the other side of the driveway. (c) Noise map and distribution showing a tilt of the 2019 SfM DEM of up to  $\pm 0.20$  m dipping to the NW. (d) Noise map and distribution after correction for tilt. ....34

Figure 2.7. Threshold maps produced for the same DEM combination (the 2019 and 2020 SfM DEM) using Method I and Method II. (a) Threshold of 0.051 m calculated using Method I. (b) Threshold of 0.071 m calculated using Method II. Noise in the road and mowed area is reduced using either method, while there are more notable differences in the vegetated area below the slide and within the slide itself.....35

Figure 2.8. Elevation change maps using a gradational scale to show differences between (a) 2007 (county-wide lidar) and 2012 (county-wide lidar), (b) 2012 (county-wide lidar) and 2019 (SfM), (c) 2019 (SfM) and 2020 (SfM), (d) 2020 (SfM) and 2021 (UAV-lidar), and (e) 2012 (county-wide LiDAR) and 2021 (UAV-lidar). ....36

Figure 2.9. Topographic profiles through the landslide showing elevation change in the landslide between 2007 and 2021. The dashed profiles indicate the topography at the beginning of each time increment and the colored profiles indicate the topography at the end of each increment.....	37
Figure 2.10. The magnitude values for each DEM combination are calculated by summing the positive elevation gains with the absolute value of elevation losses for each square metre in the sample area. (a) landslide sample area (b) the sum of the positive elevation gains and the absolute value of the negative vertical losses in the landslide sample area, and annual precipitation from 2005 to 2021. (c) the sum of positive elevation gains in the landslide sample area. (d) the sum of the absolute values of negative elevation loss in the landslide sample area. ....	38
Figure 2.11. Example of threshold maps before and after corrections for DEMs flown two weeks apart in March, 2019. The toe of the landslide was being excavated during the second flight. (a) Threshold map prior to correction, using Method II, where the threshold of detectable change is 0.33 m. Only the change due to the excavation of the toe is apparent. (b) Threshold map after survey corrections, with a threshold of detectable change of 0.13 m. Small elevation changes in the body of the landslide are apparent. (c) Landslide toe being excavated during second flight. (d) Threshold map of elevation change over the course of the next year. Areas of small positive and negative changes correlate with the changes measured over two weeks.....	40
Figure 2.12. The pattern of elevation loss and gain expected for translational debris slides and rotational slumps. Interbedded shale and limestone produce an uneven slip surface, which helps generate internal deformation of the debris slide material (Fleming and Johnson 1994).....	42
Figure 3.1. Location and surficial geology of the 7.5-minute Pitts Point and De Mossville quadrangles in Kentucky, USA. ....	50
Figure 3.2. Overview of workflow .....	51
Figure 3.3. a) Distribution of accuracies for each model tested for the Pitts Point and De Mossville Quadrangles. In both cases, the Gradient Boosted Trees model produced the greatest accuracy, and the Naïve Bayes model produced the least accurate classifier.....	57
Figure 3.4. Box and whisker plot showing the mean and quartiles for the Gradient Boosted Trees model for the Pitts Point quadrangle, with each of 31 variables in the testing data perturbed in turn, and the resulting accuracy distribution. The variables that return the lowest accuracy are the most important to the classifier.....	59
Figure 3.5. Accuracy distribution of the Gradient Boosted Trees model with the original 31 variables and with the 11 most important variables for the Pitts Point and De Mossville quadrangles. ....	60

Figure 3.6. Map 1 in the Pitts Point quadrangle, which lies just outside of the training area (Fig. 3.1). The best-performing classifier (GBT) and worst performing classifier (Naïve Bayes) are compared with the hand digitized map.....	63
Figure 3.1. Maps 2 and 3 in the Pitts Point quadrangle, which lies within the training area, and 4.5 km away from the training area, respectively (Fig. 3.1).....	64
Figure 3.8. Map 1 in the De Mossville quadrangle, which lies just outside of the training area. The best-performing classifier (GBT) and worst performing classifier (Naïve Bayes) are compared with the hand digitized map.....	67
Figure 3.9. Maps 2 and 3 in the De Mossville quadrangle, which lies within the training area, and 6.0 km away from the training area, respectively (Fig. 3.1). .....	68

# CHAPTER 1. THE INFLUENCE OF GLACIAL TOPOGRAPHY ON FLUVIAL EFFICIENCY IN THE TETON RANGE, WYOMING

## 1.1 ABSTRACT

This study examines the role of topography as a dynamic boundary condition that limits the efficiency of fluvial erosion in the post-glacial Teton Range landscape. The volume of sediment currently stored in two major catchments was estimated using high-resolution LiDAR and geometric reconstructions of depth to bedrock. Seismic reflection data in Moran Bay reveals post-glacial sediment preserved behind a submerged moraine, which isolates the bay from the larger Jackson Lake depocenter. The volume of post-glacial sediment stored in the canyons and bay totals  $173.82 \pm 19.5336.0$  ( $\times 10^{-3}$  km<sup>3</sup>), which translates to a catchment-wide sediment production rate of  $0.17 \pm 0.02$  mm/yr. The rock-equivalent sediment volume in Moran Bay is  $4.4 \pm 0.9$  ( $\times 10^{-3}$  km<sup>3</sup>), only ~2.6% of the total post-glacial volume. While the estimated sediment production rate in the canyons is similar to the uplift rate, the denudation rate derived from Moran Bay sediment is  $0.004 \pm 0.001$  mm/yr, implying highly inefficient post-glacial sediment transport. The fluvial system has been disequilibrated by glacial erosion such that interglacial valley profiles lack the steepness needed to transport sediment, delaying sediment evacuation until the next glacial advance, or until uplift sufficiently steepens the fluvial system so that it regains efficiency. Furthermore, colluvial production rates in the deglaciated valleys are close to long-term denudation and uplift rates, suggesting that once topography has been equilibrated to glacial erosion processes, subsequent glaciers do not need to produce much bedrock erosion, but mainly sweep out accumulated sediment to maintain equilibrium.

## 1.2 INTRODUCTION

The relationships and feedbacks between rock uplift, denudation and topography remain enigmatic, and many studies regard topography as merely a record of the interplay between tectonic and climatic forces. The role of climate in driving fluvial and glacial processes that keep pace with (or enhance) rock uplift has been thoroughly examined (Mitchell & Montgomery, 2006; Egholm et al., 2009; Koppes & Montgomery, 2009; Whipple, 2009; Adams et al., 2020; Spotila, 2022) although a definitive consensus remains elusive. The potential role of topography itself as a dynamic boundary condition that controls the rate of denudation and sediment transport has received far less attention. This study examines how topography limits the efficiency of fluvial erosion, thus imposing a threshold that must be overcome for the fluvial system to effectively respond to uplift. As glaciers retreat, a paraglacial landscape with over-steepened valley walls produces sediment rapidly (Norton et al., 2010; Ballantyne, 2013). However, deglaciated valley bottoms typically lack the profile steepness to facilitate fluvial erosion and sediment evacuation (Dortch et al., 2011; Moon et al., 2011). Thus, if the glacial topographic conditioning is exhaustive, topography itself creates a protracted lag in fluvial response time, similar to moraine dams preventing fluvial incision in high mountains (e.g., Korup & Montgomery, 2008). The impacts of continued climate change

and glacial ablation may lead to development of numerous inefficient rivers, which can impact sediment transport and water supply (Herman et al., 2021).

Although sediment volumes or production rates have been estimated for deglaciated valleys in a number of locations (e.g., Otto et al., 2009; Tunncliffe & Church, 2011; Tranel et al., 2015; Ardelean et al., 2017), documentation of complete post-glacial catchment sediment budgets from source to sink is rare (e.g., Fame et al., 2018). Studies of fluvial transport in deglaciated catchments have focused on enhanced sedimentation in lower reaches where fluvial processes dominate (Church & Ryder, 1972; Ballantyne, 2013), in contrast to the upper paraglacial reaches where glacial drift is less abundant and rivers are smaller (Dietsch et al., 2015). Field-based denudation studies often rely on the assumption that short-term (days to years) observations of suspended sediment yields from modern rivers represent long-term ( $10^4$ - $10^6$  years) denudation rates, yet these rates can be quite variable through time (Koppes & Montgomery, 2009; Spotila, 2022). Various strategies have also been employed to model fluvial erosion, but there are few studies that directly quantify mass flux (Adams et al., 2020). These knowledge gaps lead to uncertainty in the governing relationships between uplift, denudation and topography, leading to a reliance on modeling for insight (Pedersen & Egholm, 2013).

To assess fluvial efficiency in a relict glacial landscape and address spatial-temporal data disparities, a complete post-glacial sediment budget and long-term ( $10^4$ - $10^8$  years) uplift and denudation data are necessary. The Teton Range (Wyoming, western USA, Fig. 1.1) provides an ideal natural setting to examine this problem, as fluvial sediment derived from two deglaciated catchments is trapped in a perched lacustrine basin (Moran Bay), thus allowing a post-glacial sediment budget to be constructed. Existing high-resolution light detection and ranging (LiDAR) topographic data allows detailed geomorphologic mapping of glacial and post-glacial sediment and the estimation of sediment volumes and production rates. Seismic reflection data acquired for this study in Moran Bay reveals a complete post-glacial (14.4 ka) sediment package from two major catchments in the range, from which sediment volumes can be estimated. The glacial history has been constrained by  $^{10}\text{Be}$  cosmogenic dating of glacial moraines (Pierce et al., 2018), and the uplift history is well-constrained by multiple low-T thermochronology studies (Brown et al., 2017; Thigpen et al., 2021). Here, we leverage these datasets to quantify post-glacial sediment production and flux from source to sink. We find that although hillslope sediment production rates are close to uplift rates, glacially carved valley bottom gradients limit efficient fluvial sediment flux, stalling sediment evacuation until the next glacial advance, or until uplift sufficiently steepens the system to again become efficient.



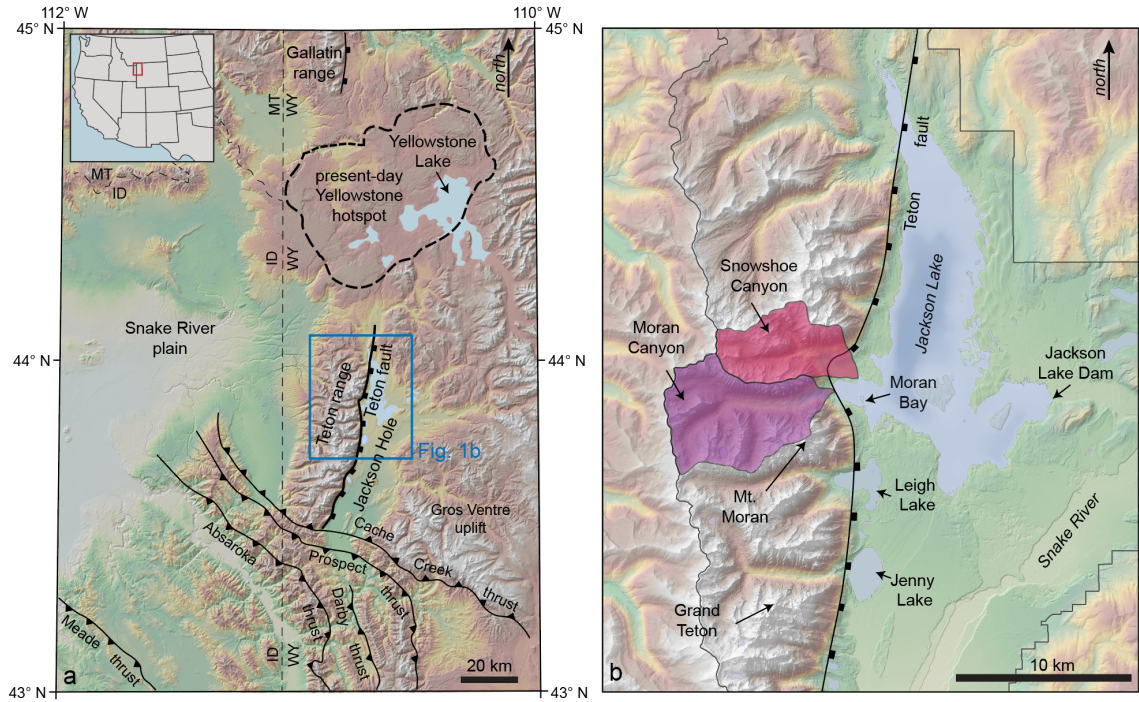


Figure 1.1 a) Regional map of the Teton Range which lies at the eastern edge of the Basin and Range in northwestern Wyoming. Displacement along the Teton normal fault that bounds the eastern side of the range has produced an asymmetric uplift that dips to the west. b) Moran and Snowshoe Canyons drain into Moran Bay, the westernmost portion of Jackson Lake. The terminal moraine formed by the Pinedale glacial advance ( $14.4 \pm 0.8$  ka) impounded Jackson Lake.

### 1.2.1 Geologic Setting

The Teton Range lies at the eastern edge of the Basin and Range in northwestern Wyoming (Fig. 1.1). Normal displacement along the Teton fault on the eastern edge of the range has produced a west-dipping asymmetric uplift (Foster et al., 2010; Brown et al., 2017). Precambrian units in the range center are unconformably overlain by west-dipping Paleozoic and Mesozoic strata (Love et al., 1992). The onset of Teton fault slip is  $\sim 10$  Ma, and displacement estimates range from 11.4-12.6 km (Thigpen et al., 2021). Although the Teton Range lies within the Intermountain Seismic Belt, the Teton fault remains quiescent, with no evidence of a major slip event in the past 5 ka (DuRoss et al., 2019).

Multiple glacial advances during the Quaternary carved the spectacular Teton relief ( $> 2$  km, Good & Pierce, 2016) and has driven range divide migration to the west (Foster et al., 2010; Zhu et al., 2021). Evidence from the most recent Bull Lake (170-130 ka) and Pinedale (20-12 ka) glaciations indicate that the Yellowstone ice cap extended into the Jackson Hole valley, and alpine glaciers in the Teton Range flowed east to join the main glacial lobe (Pierce et al., 2018). The Pinedale advance formed the terminal

moraine, which naturally impounded Jackson Lake and the multiple moraine lakes on the range front. Completion of the Jackson Lake dam in 1916 raised the natural lake level by ~12 m. Moran and Snowshoe Canyon, two major Teton catchments, both drain into Moran Bay in the western part of Jackson Lake (Fig. 1.1). They are similar to other Teton catchments that have drainage areas of  $>20 \text{ km}^2$ , and their topographic signature is typical of glaciated topography, with deeply incised canyons and elongated and flattened valley profiles (Whipple et al., 1999). Modern wind and precipitation patterns are similar to those from the last glacial maximum (LGM) while pollen studies indicate that vegetation changed from alpine meadow to mixed pine-spruce-fir forest following deglaciation (Whitlock, 1993; Foster et al., 2010).

## 1.3 METHODS

### 1.3.1 Moran Bay seismic acquisition and sediment volume estimate

Stratigraphic horizons bounding the sediment package in Moran Bay were mapped using a grid of CHIRP seismic profiles, acquired using an Edgetech SB-0512i CHIRP sub-bottom profiler. Data were acquired at a tow velocity of ~3 knots and shot points were collected at 2 s intervals across a frequency range of 0.4-4.0 kHz. Seismic data were processed in Seisware using a bandpass filter and amplitude gain. Time-depth conversions were calculated using a constant velocity of 1500 m/s, as unconsolidated sediment is in hydrostatic equilibrium with freshwater (Kindinger et al., 1994). Sediment volumes between mapped stratigraphic horizons were calculated using Trinity T3 software.

### 1.3.2 Geomorphologic map

Landforms in Moran and Snowshoe Canyons were mapped using a combination of digital terrain analysis and photo interpretation (Otto et al., 2009. Ardelean et al., 2017). Maps were produced in GIS software using a 0.5 m digital elevation model (DEM) and derivative maps produced from airborne LiDAR (National Park Service, 2014) and 0.3 m Google Earth® satellite imagery from 2013 and 2015. Moran Canyon landform interpretations were field-checked in 2021. Mapped geomorphologic units include talus cones, debris fans, talus slopes, alluvium, glacial drift, moraines, rock glaciers, and bedrock.

### 1.3.3 Canyon sediment volume estimates derived from modeled bedrock DEM

The bulk sediment volume in the main trunk of Moran Canyon and two tributary canyons was estimated by differencing a LiDAR-based surface DEM and a modeled bedrock DEM. Because glacial drift is not observed to be deposited upon or interfingering with older colluvial or alluvial deposits, we interpret that pre- and syn-Pinedale ( $14.4 \pm 0.8 \text{ ka}$ ) colluvial and alluvial deposits were evacuated from the canyon during that glacial period. If correct, mapped colluvial and alluvial deposits should have

been derived from the current interglacial period. In sediment volume estimates, it is assumed that mapped boundaries of deposits extend vertically down to bedrock, though it is acknowledged that there may be underlying glacial debris.

Cross sections of the bedrock surface beneath the canyon floor sediment were projected along 33 lines using exposures of bedrock on either side of the canyon; 12 of these cross-sections are also constrained by limited canyon floor bedrock exposures (Fig. 1.2a), which were confirmed via field checking. Prominent irregularities in the bedrock surface DEM were smoothed using the focal statistics tool in ArcGIS with a circular radius of 10 m and then sampled every 10 m to generate the cross sections. A smoothing spline function within the MATLAB curve-fitting toolbox was used to project a bedrock surface beneath the surface for each cross section; smoothing spline values ranged between 0.94 and 0.99. The smoothing spline function fits a curve piecewise to each data point; the value ranges from 0, where it produces a least-squares straight-line fit, to 1, where it produces a cubic spline interpolant. This method prevents overestimation of bedrock depth that can be produced by a polynomial function (Fig. 1.2b). The final bedrock surface DEM was generated from the projected bedrock cross sections and supplementary points in ArcGIS using the Topo to Raster tool, which uses an iterative finite difference interpolation technique. Supplementary points were added along valley walls at the contacts of colluvium and exposed bedrock, at exposed bedrock in the valley bottom, and in other locations where the modeled DEM appeared to either over-estimate sediment depth or rise above the ground surface (Fig. 1.2b). This methodology is similar to Schrott et al. (2003), although that study used polynomial functions that led to an overestimation of bedrock depth, particularly when valleys were relatively narrow. Tranel et al. (2015) used exposed bedrock slopes above talus cones in the Tetons to project the bedrock below the talus and estimate individual talus cone volumes, which produced values similar to those presented here. Lastly, we conservatively incorporate a  $\pm 20\%$  uncertainty for estimates of the total sediment volume and denudation rates in the canyons.

#### 1.3.4 Canyon sediment volume estimates derived from colluvial sediment production rate

The bulk volume of talus cones and debris fans was divided by their contributing source area to calculate a catchment-averaged colluvial production rate. Outside of the modeled bedrock DEM area, the colluvial production rate was applied to source areas of talus cones and debris fans to estimate their bulk volume.

#### 1.3.5 Canyon sediment volume estimates derived from assigned thickness

To estimate sediment volumes for areas where there are talus slopes, rock glaciers, small cirque moraines, lakes, and areas of glacial drift, sediment thicknesses were assigned based on geospatial data and field observations. To account for uncertainties associated with these estimates, total rock volume calculations and denudation rates are reported with and without these values.

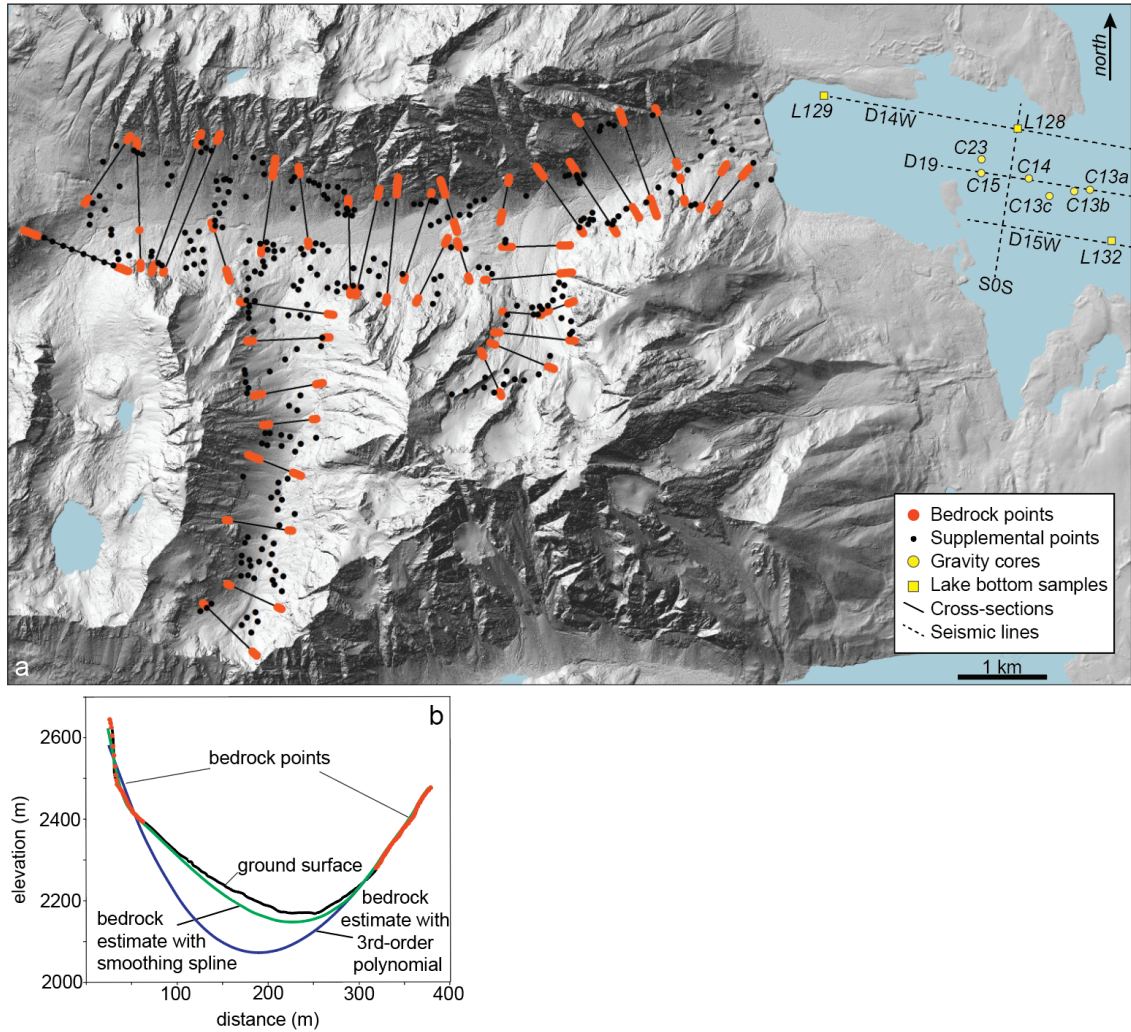


Figure 1.2 a) Thirty-three cross sections in the Moran catchment were used to project the bedrock surface under the sediment. Four CHIRP seismic profiles (D19, D14W, D15W and S0S) were used to estimate the volume of sediment derived from the Moran and Snowshoe catchments, and lake bottom samples and gravity cores were used to support the seismic interpretation. b) Example of bedrock surface produced in MATLAB using elevations of exposed bedrock along the valley walls to project the bedrock surface under the sediment.

Outside of the area covered by the bedrock DEM, glacial drift is assigned a thickness of  $2.4 \pm 1.3$  m based on the average of 65 gully depth observations. The bulk volumes of cirque moraines and rock glaciers were individually estimated by measuring their heights over the surrounding terrain and multiplying by their mapped area. The average thickness of the nine cirque moraines and eight rock glaciers is  $8.1 \pm 3.6$  m and  $12.3 \pm 6.7$  m, respectively. We have estimates of the average thickness of talus slopes and alluvium from the modeled bedrock DEM area, but to avoid overestimation, we reduce these average thicknesses in areas outside of the modeled bedrock DEM area. While talus slopes average 6.9 m thick in the modeled DEM area, for areas outside of this, we assign

an average thickness of 3.0 m. The average estimated thickness of alluvium in the main trunk of Moran Canyon is 14.3 m in the modeled bedrock DEM area. Other deposits of alluvium occupy smaller areas, and so to avoid overestimation are assigned an average thickness of 5.0 m. Sixteen small lakes in the canyons have formed upon areas of bedrock, talus, drift, and alluvium and were assigned a nominal thickness of 1.0 m.

#### 1.3.6 Porosity estimates

For each material, porosity estimates are required to convert bulk sediment volumes to solid rock volumes. Although talus porosity is generally heterogeneous, previous studies, including studies in the Tetons, calculated a narrow range (0.20-0.26) of talus porosity (Tranel et al., 2015; Otto et al., 2009; Sass & Wollny, 2001). Alluvium and glacial drift porosities span large ranges of 0.06 to 0.48 (Frings et al., 2011) and 0.01 to 0.43 (Kilfeather & van der Meer, 2008), respectively. For rock glaciers, a porosity range of 0.40 to 0.60 (Hauck et al., 2011) was used. A porosity range of 0.35-0.45 was used for Moran Bay sediments, based on porosity estimates of Moran Bay short cores and typical values for clay, silt and sand (Leopold et al., 1964).

#### 1.3.7 Monto Carlo simulation for rock volume and erosion rate calculations

A Monte Carlo simulation with 50,000 iterations was performed to calculate rock volumes and denudation rates. We assumed a normal distribution of values for the bulk sediment volume, post-glacial time, and porosities. We built in uncertainty for the bulk sediment volume by incorporating  $\pm 20\%$  range for the volume estimates, and a post-glacial time of  $14.4 \pm 0.8$  ka. The range of porosity values includes standard deviations calculated using the range rule ( $\text{range} \div 4$ ). An extreme minimum value for the volume of stored canyon sediment was also calculated by omitting volumes derived from assigned thicknesses. The post-glacial sediment production rate was calculated by dividing the post-glacial rock volume in the canyons and bay by the catchment area and the post-glacial deposition time interval; the post-glacial fluvial erosion rate was calculated by dividing the rock volume in the bay by the catchment area and post-glacial time.

### 1.4 RESULTS

#### 1.4.1 Geomorphologic mapping of Moran and Snowshoe Canyons

The geomorphologic units in Moran and Snowshoe Canyons (Fig. 1.3) include talus cones, debris fans, glacial drift, alluvium, talus slopes, rock glaciers and cirque moraines (Fig. 1.4). In the canyons, talus cones and debris fans dominate the landscape. Talus cones have linear slopes of  $\sim 25^\circ$  and range in height from 50-400 m. Debris fans have gently concave slopes averaging  $\sim 17^\circ$ , often have obvious debris flow tracks, and are up to 200 m high. Glacial drift deposits, present at higher elevations, are generally vegetated, include scattered boulders, and have either a network of gullies or are knobby



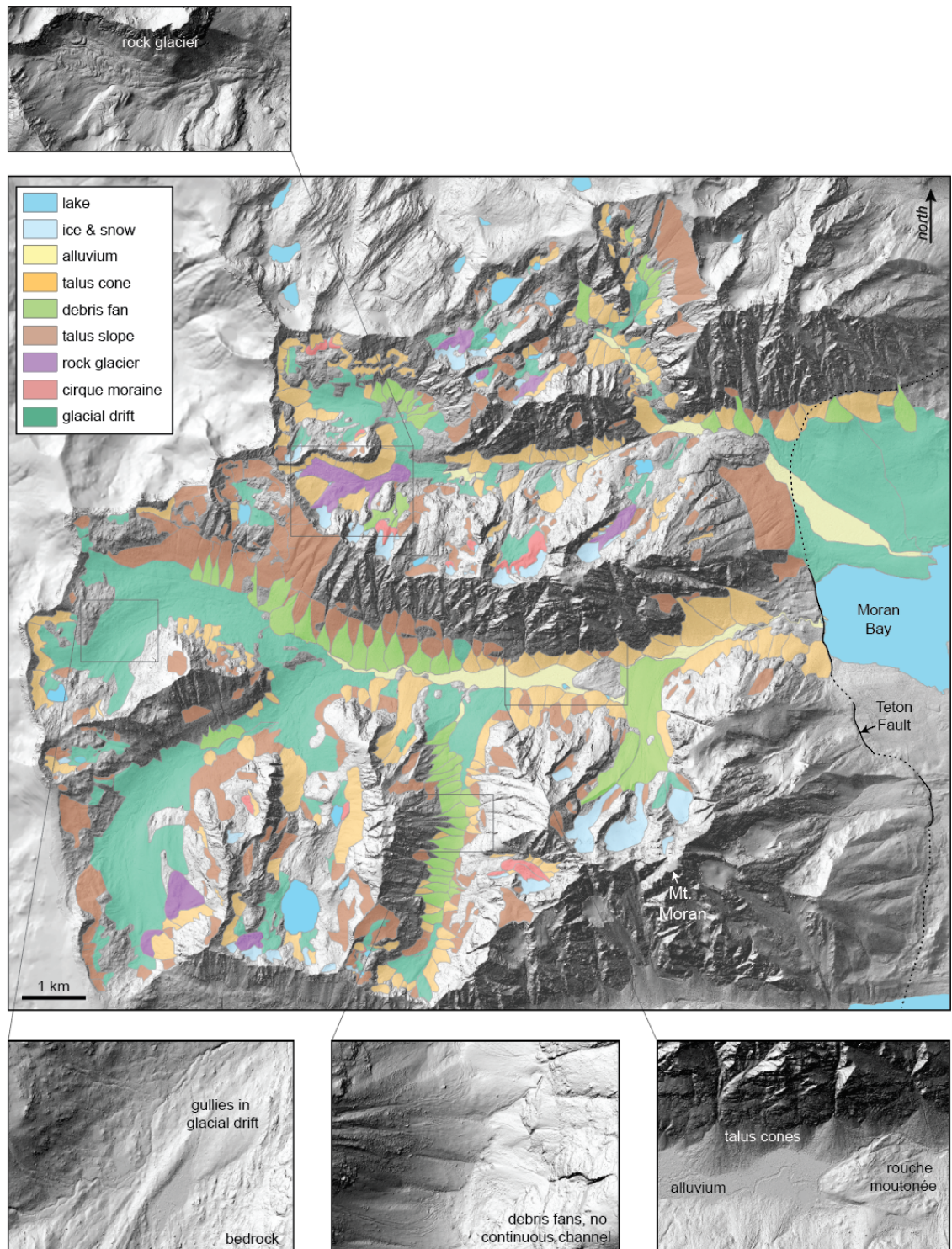


Figure 1.3. Geomorphologic map of the Moran and Snowshoe catchments. The base map is a hillshade map derived from LiDAR flown in 2014. Callouts show examples of talus cones, debris fans, alluvium, glacial drift, a rock glacier, and a roche moutonnée.



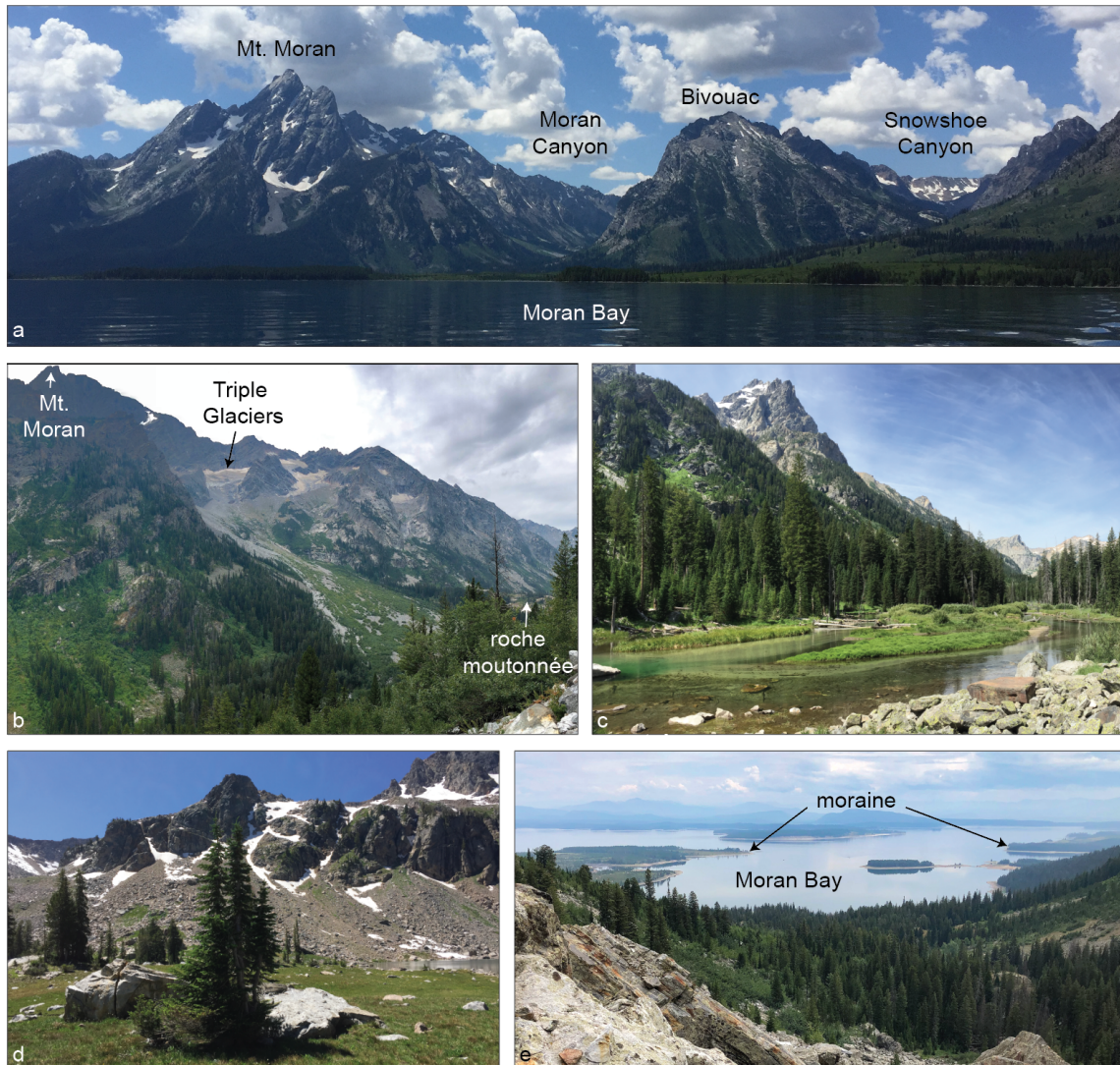


Figure 1.4. Examples of landforms in the Teton Range: a) view of Moran and Snowshoe Canyons from Moran Bay, b) view of Mt. Moran, Triple Glaciers, debris fan, talus cones and a roche moutonnée in Moran Canyon, c) alluvium in a glacially-flattened valley, d) talus cones, e) view from Moran Canyon of Moran Bay and the moraine that isolates it from Jackson Lake.

with intermittent exposures of bedrock. Slopes with talus and periglacial debris are grouped together as talus slopes. Rock glaciers, which are distinguished by their interior arcuate lobes, reach lengths as long as 1.2 km and rise up to 25 m above the surrounding terrain. Some small moraines in the upper basins have crests up to 20 m above the surrounding terrain. Alluvial deposits are distinguished by their flat topography, which is cut by sinuous stream channels and meander scars.

The 6.6 km-long main trunk of the 44.4 km<sup>2</sup> Moran catchment is a well-defined glacial trough up to 1,000 m deep (Figs. 1.3 and 1.4). The trunk canyon is joined by five

tributary canyons up to 5.5 km in length (M1-M5, Fig. 1.5). The main trunk is lined by debris fans and talus cones that, in places, are nearly joined across the valley. There is a prominent 750 m-long by 500 m-wide roche moutonnée centrally located in the main trunk; its southwestern edge aligns with a NW striking dike that crosses the valley (e.g., Love et al., 1992). Upstream of the roche moutonnée, Moran Creek has developed a relatively flat 1.8 km-long by 0.3 km-wide alluvial plain. Downstream, the valley gradient steepens where it descends through knobby bedrock to Moran Bay. The western edge of Moran Bay is defined by the modern Teton fault scarp.

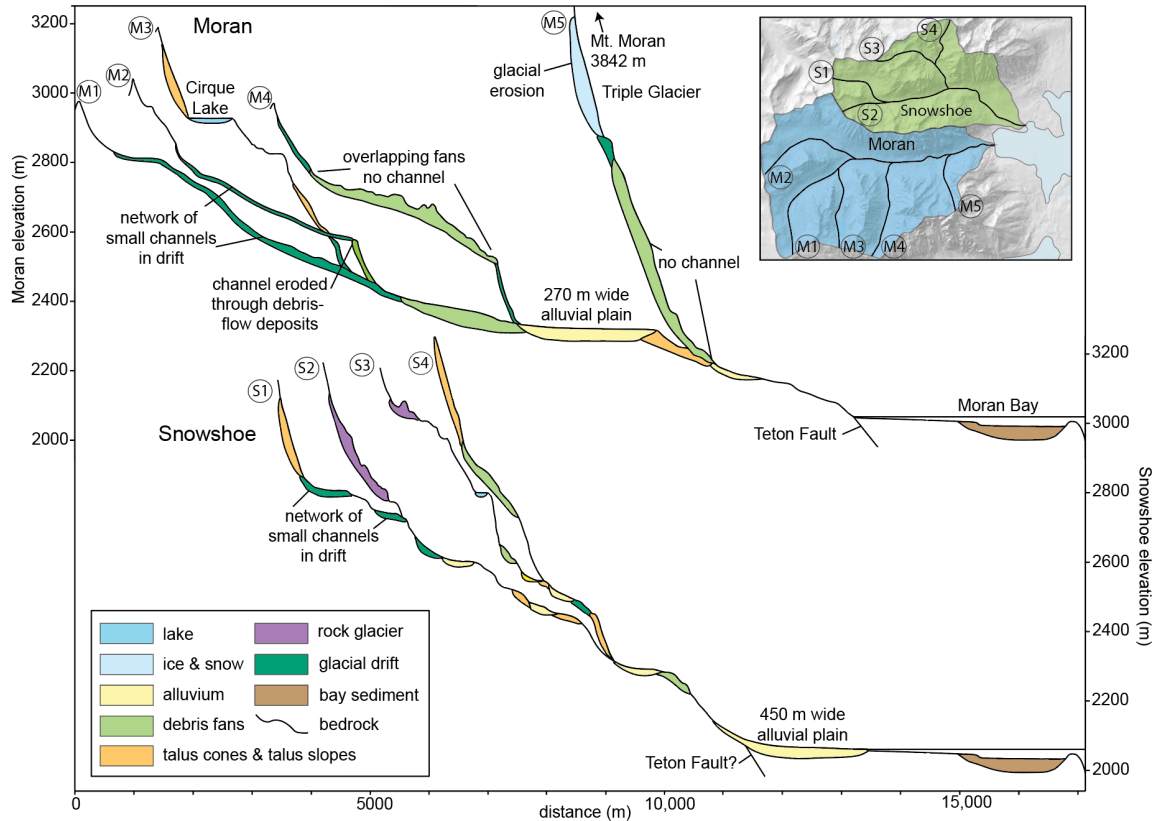


Figure 1.5. Stream profiles and geomorphic units along major tributary valleys of the Moran and Snowshoe catchments. Geomorphic units in contact with the valley bottom are shown, but depths are not implied.

Each Moran Canyon tributary displays a unique subset of landforms, longitudinal profiles, and channel characteristics (Fig. 1.5). Tributary M1 has a relatively smooth graded profile, with a valley floor lined with glacial drift and a network of gullies. Talus cones and debris fans are less prevalent here and do not extend far into the valley. Tributary M2 is similar to M1, but there is a knickpoint before it joins M1. Here the toe of a debris flow deposit has been eroded to produce an incised bedrock channel >5 m deep. Tributary M3 includes the largest lake in the catchment, Cirque Lake. M3 does not have a well-developed trough shape, and the valley floor is mostly knobby bedrock. The channel that drains the overflow from Cirque Lake flows over bedrock, glacial drift and



around the base of talus cones as it drops to join M1. Tributary M4 is dominated by talus cones and debris fans that overlap to form an irregular valley floor with no continuous channel. Where the slope steepens to join the main trunk, the valley floor is lined by glacial drift incised by a small channel. Tributary M5 drains Triple Glaciers on the northwestern flank of Mt. Moran (elev. 3842 m). Here the largest debris fan in the study area extends down the axis of the valley and across the floor of Moran Canyon (Fig. 1.4). A channel draining the glacier disappears underground partway down the fan.

The Snowshoe catchment (26.4 km<sup>2</sup>) is composed of a main trunk with tributary canyons up to 3 km in length and several small glacial basins (S1-S4, Fig. 1.5). Unlike the graded longitudinal profiles in the Moran catchment, the valleys in Snowshoe have multiple knickpoints, and the surface topography is much rougher (Figs. 1.3 and 1.5). The north wall of the main trunk is lined by talus cones and the southern side consists of multiple small glacial basins with moraines, rock glaciers, tarns, talus cones and talus slopes. Snowshoe Canyon is drained by North Moran Creek, which exits the canyon and flows across glacial drift, where it forms a 1.3 km by 0.4 km wide alluvial plain adjacent to Moran Bay.

The longitudinal profile of S1 has four knickpoints before it is joined by S3 and S4. The flat parts of the stepped valley floor are composed of either glacial drift at high elevations or alluvium at lower elevations. The steep portions of each step are composed of bedrock channels. S2 is distinguished by the largest rock glacier (~1.2-km-long) in the catchment. The upper half of S3 is composed of knobby bedrock with several tarns, rock glaciers and drift, and lacks a well-developed channel. Where it is joined by tributary S4, the valley has a trough-shape and a channel bordered by talus cones. In tributary S4 the channel flows between glacial drift and debris fans, and then over bedrock as the valley steepens to join S3.

#### 1.4.2 Moran Bay seismic reflection profiling

Seismic profile D19, which extends through the midline of Moran Bay and into the main depocenter of Jackson Lake, reveals that the bay is effectively perched above and is isolated from the main depocenter by a bathymetric ridge, essentially trapping the post-glacial sediment derived from the two catchments (Fig. 1.6). Moran Bay sedimentary packages are separated by three key horizons that are interpreted to reflect major changes in depositional character.

Horizon A, which defines the top of the acoustic basement beneath which there is no internal reflectivity, is an uneven surface with maximum and minimum depths of ~47 m and ~9 m below the modern lake surface, respectively. This surface also defines the top of the bathymetric ridge that separates Moran Bay from the main Jackson Lake depocenter (Fig. 1.6). Lake bottom gravity cores attempted along the ridge had limited penetration depth and yielded mostly sand and gravel (Table 1.1). Horizon B4 defines the top of a package of internally stratified yet pervasively deformed sediment that is overlain by an essentially undeformed sediment package. Horizon C3 defines the lake bottom.

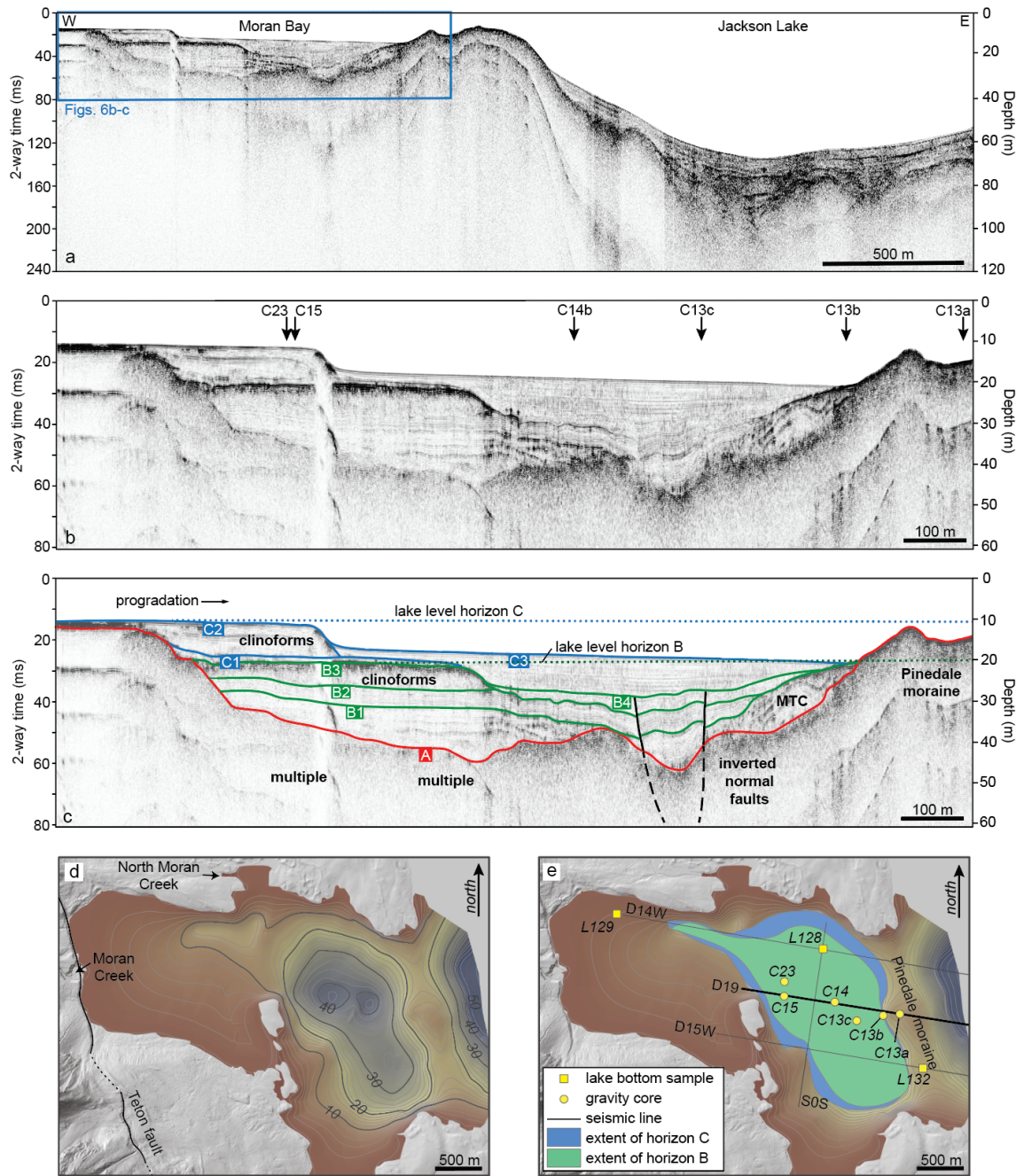


Figure 1.6. CHIRP seismic profiles and maps of Moran Bay. a) Seismic profile D19 showing Moran Bay is isolated from the main depocenter of Jackson Lake by a submerged bathymetric ridge. b) Moran Bay seismic profile with locations of lake bottom samples and gravity cores. c) Interpretation of the seismic profile. d) Paleobathymetric map of Moran Bay based on horizon A, the Pinedale moraine. e) Map showing the horizontal extents of horizons B and C, and the locations of seismic lines, short cores and lake bottom samples.

Table 1.1 Moran Bay gravity core and lake bottom sample locations and descriptions.

Horizon Sampled	Sample	Sample type	Sample ID	Location	Description
A	C13a	Gravity core	No yield	522794, 4856242	No core, sample of sand and gravel
A	C13b	Gravity core	No yield	522640, 4856234	No core, mud on top of hard surface
A	L132	Lake bottom	JL-GB-132	522987, 4855772	Brown-grey pebbly muddy medium sand with charcoal
C	C13c	Gravity core	JL19-13.5A-1G	522410, 4856188	34 cm silty and sandy clay, massive to discontinuously laminated
C	C14b	Gravity core	JL19-14B-1G	522216, 4856352	34 cm silty and sandy clay, discontinuously laminated
C	C15	Gravity core	JL19-15-1G	521772, 4856401	29 cm grey structureless mud with abundant coarse plant macrophyte fragments
C	C23	Gravity core	JL19-23-1G	521774, 4856529	32 cm silty and sandy clay, discontinuously laminated
C	L128	Lake bottom	JL-GB-128	522112, 4856812	Brown-grey sandy muddy charcoal
Landward of seismic lines	L129	Lake bottom	JL-GB-129	520288, 48571118	Brown-grey muddy sand with charcoal

Between Horizons A and B4, the pervasively deformed sediment package within which there are four distinctive subunits (Fig. 1.6c). B1 is the lowermost and is up to 9 m thick, discontinuous, with distorted internal reflectors. B2 is a set of parallel reflectors up to 14 m thick which are deformed by folding. B3 is a 6 m thick package ~20 m below the modern lake surface. B4 is a set of parallel reflectors that onlap B3. All of the reflectors between Horizons A and B are offset along two discontinuities which terminate at Horizon B. Intermediate reflectors between Horizons B4 and C3 appear mostly undeformed and three subunits can be separated (Fig. 1.6c). C1 lies atop B3, is 1 to 2 m thick and nearly horizontal. C2 is a 7 m-thick stack of two clinoforms ~12 m below the modern lake surface. It extends 450 m from the western edge of the seismic line. C3 is a low amplitude highly continuous package up to 9 m thick that onlaps the clinoforms and is ponded in the center, and the top of which gently slopes to the east. Gravity cores collected from the lake bottom and across Horizon C yield laminated silty and sandy clay with variable amounts of organic matter and muddy sand with charcoal (Fig. 1.6, Table 1.1). For the volume estimates discussed below, we consider Horizons A and C to represent the bottom and top, respectively, of the Moran Bay post-glacial sediment package.

#### 1.4.3 Estimates of sediment volume, post-glacial sediment production, and erosion rates

Monte Carlo simulations yield total post-glacial (post-  $14.4 \pm 0.8$  ka) rock volumes of  $169.38 \pm 35.09$  ( $\times 10^{-3}$  km<sup>3</sup>) for the canyon catchments, a total rock volume in

Moran Bay of  $4.44 \pm 0.90 \times 10^{-3} \text{ km}^3$ , and a total post-glacial rock volume of  $173.82 \pm 35.99 \times 10^{-3} \text{ km}^3$  (Table 1.2). These simulated volumes include uncertainties discussed in the methods section. These volume estimates yield a post-glacial sediment production rate of  $0.17 \pm 0.02 \text{ mm/yr}$  and an average catchment-wide post-glacial fluvial erosion rate of  $0.004 \pm 0.001 \text{ mm/yr}$ . Based on these estimates, the Moran Bay sediment volume represents only ~2.6% of the post-glacial sediment volume stored in Moran and Snowshoe Canyons (Table 1.2). In an end member scenario where assigned canyon sediment thicknesses were zeroed and the lower estimated volumes based on uncertainty are used, while the Moran Bay sediment column is maximized based on uncertainty (ignoring organic matter, autochthonous carbonate, and biogenic silica); the post-glacial bay sediment volume is only 4.7% of the minimum sediment estimated in the canyons.

Table 1.2 Summary of area and sediment volume calculations in Moran Canyon, Snowshoe Canyon and Moran Bay. Volume analysis is based on a combination of the modeled bedrock DEM analysis, sediment production rate of colluvium and assigned thicknesses based on landform observations.

Landform	Bulk volume ( $\times 10^{-3} \text{ km}^3$ )		Total bulk volume ( $\times 10^{-3} \text{ km}^3$ )	Rock volume ( $\times 10^{-3} \text{ km}^3$ )		Post-glacial volume (%)	
	Modeled bedrock DEM area	Outside bedrock DEM area		Including assigned thickness areas	Without assigned thickness areas	Including assigned thickness areas	Without assigned thickness areas
Talus cones & debris fans	$81.39 \pm 16.27$	$84.31 \pm 16.86$	$165.70 \pm 33.13$	$127.59 \pm 25.63$	$127.59 \pm 25.63$	73.41	89.22
Talus slopes	$5.42 \pm 1.08$	$17.23 \pm 3.45$	$22.65 \pm 4.53$	$17.45 \pm 3.50$	$4.17 \pm 0.84$	10.04	2.92
Alluvium	$9.33 \pm 1.87$	$3.73 \pm 0.75$	$13.06 \pm 2.62$	$9.53 \pm 2.36$	$6.81 \pm 1.69$	5.48	4.76
Rock glacier	-	$13.54 \pm 2.71$	$13.54 \pm 2.71$	$10.56 \pm 2.56$	-	6.08	-
Cirque moraine	-	$4.91 \pm 0.98$	$4.91 \pm 0.98$	$3.83 \pm 0.93$	-	2.20	-
Lacustrine	-	$0.55 \pm 0.11$	$0.55 \pm 0.11$	$0.42 \pm 0.11$	-	0.24	-
<b>Total post-glacial sediment in canyons</b>	$96.14 \pm 19.22$	$124.27 \pm 24.86$	$220.41 \pm 44.08$	$169.38 \pm 35.09$	$138.57 \pm 28.16$	97.45	96.90
Moran Bay	-	$7.40 \pm 1.48$	$7.40 \pm 1.48$	$4.44 \pm 0.90$	$4.44 \pm 0.90$	2.55	3.10
<b>Total post-glacial sediment in the system</b>	$96.14 \pm 19.22$	$131.67 \pm 26.34$	$227.81 \pm 45.56$	$173.82 \pm 35.99$	$143.01 \pm 29.06$	100.00	100.00
Glacial drift	$11.45 \pm 2.29$	$28.12 \pm 5.62$	$39.57 \pm 7.91$	$30.86 \pm 5.19$	$8.95 \pm 2.18$	-	-

## 1.5 DISCUSSION

### 1.5.1 Moran Bay impoundment timing, geometry, and sedimentation history

Key to making useful comparisons of different stored sediment volumes in the Moran/Snowshoe system is the necessity to demonstrate that the majority of post-glacial sediment exiting the canyons is actually deposited and remains in Moran Bay. Seismic imaging along line D19 shows that the Moran Bay sedimentary sequence is separated from the main depocenter of Jackson Lake by a submerged ridge that provides considerable bathymetric relief relative to the adjacent lake floor (Fig. 1.6), and other lines (D14W, D15W) demonstrate that this ridge is continuous to the north and south. The lack of internal seismic reflectivity in the units below Horizon A, the mapped geometry and location of the ridge, and the coarse, poorly sorted sediment sampled by the limited gravity cores along this feature (Table 1.1) informs the interpretation that the ridge is a glacial moraine. Additionally, it is positioned in the same location as the terminal moraines that impound Leigh and Jenny Lakes to the south (Fig. 1.1) and the submerged ridge is connected to the moraine units exposed at the surface (Love et al., 1992), now referred to as Pinedale-3 (Pierce et al., 2018), which partially encloses Moran Bay at present (Figs. 1.3, 1.4, and 1.6). Formation of this terminal moraine ridge likely occurred as the combined result of the Snake River Lobe flowing southward along the range front, essentially limiting the valley migration of the terminal moraine exiting Moran Canyon. Exact glacial stratigraphic relationships remain uncertain, but it is likely that this ridge/moraine formed during the Pinedale-2 and Pinedale-3 glacial advances (Pierce et al., 2018). Assuming the age of the now-submerged Moran Bay moraine is equivalent to the inner Pinedale-3 moraine of Jenny Lake, this deglacial surface mapped in this study as Horizon A yields an age of  $14.4 \pm 0.8$  ka (Pierce et al., 2018), which requires that deposits overlying this horizon are post-glacial.

### 1.5.2 Sediment production and erosion rate

Glacial processes modify the landscape to produce U-shaped valley walls and flattened and elongated valley profiles (Harbor, 1992). The de-buttressing of steep glacial valley walls upon glacial retreat results in unstable slopes of jointed rock. Rock falls and debris flows then produce the talus cones and debris fans that form the majority of sediment in Moran and Snowshoe Canyons. The basin-wide averaged rate of post-glacial sediment production in Moran and Snowshoe Canyons is  $0.17 \pm 0.02$  mm/yr, which assumes that all of the sediment was deposited after the Pinedale glaciation. This denudation rate does not include chemical weathering. The calculated sediment production rate is similar to the long-term denudation rate of 0.14 mm/yr calculated by Brown et al. (2017) using low-temperature thermochronology and the basin-wide post-glacial sediment production rate of 0.13 mm/yr calculated for Garnet Canyon via a combination of hillslope and ridge erosion by Tranel (2015). While the maximum uplift rate along the Teton Fault at Mt. Moran is 0.28 to 0.31 mm/yr (Thigpen et al., 2021), due to the asymmetric uplift of the Teton Range (Byrd et al., 1994; Foster et al., 2010), the uplift rate at the heads of the catchments, which are near the center of the range, is

approximately 0.14 to 0.16 mm/yr, such that the average uplift of the catchments is roughly 0.21 to 0.23 mm/yr. The similarity of these rates indicates that paraglacial hillslope processes are an essential contributor to the overall erosion rate of the Tetons.

While glacial erosion increased the topographic relief of the valley walls, producing conditions favorable to rockfall, the relief of the valley profile has been reduced, and it is less steep and less concave than fluvial valley profiles (Whipple et al., 1999). This gradient reduction lowers stream power and diminishes sediment transport capacity out of the canyons, producing a system that is transport-limited. While the valleys are apparently steep enough in places for the stream to erode down to bedrock, mobilized sediment may be trapped by subsequent flattened step-like sections below each bedrock reach (Fig. 1.5). In effect, Teton valleys are almost entirely encompassed in the Periglacial Domain (Hobley et al., 2010; Dietsch et al., 2015), which is characterized by U-shaped valleys dominated by glacial debris, talus, and paraglacial fans, and which lacks trunk streams with the power to transport sediment and incise gorges into their valleys. The lack of transport results in the volume of alluvium stored in the canyons being more than double the volume of sediment that has been transported and deposited into Moran Bay.

In contrast to the rate of sediment production, the catchment-wide post-glacial fluvial erosion rate is just  $0.004 \pm 0.001$  mm/yr, even lower if we constrain autochthonous sediments versus allochthonous sediments from the canyon, pointing to a disconnect between weathering production and sediment yield, a hallmark of sediment transport in deglaciated terrain (Church & Ryder, 1972; Ballantyne, 2002; Tunnicliffe & Church, 2011). Sources of Moran Bay sediment include glacial drift, periglacial debris, talus cones and debris fans, debris flows that enter the channel, and fluvial and glacial bedrock erosion (Figs. 1.3, 1.4, 1.5). In addition, lake sediments composed of sponges (biogenic silica), ostracods (carbonate), algae (biogenic silica, organic matter) contribute to accumulation patterns in Moran Bay (Rasbold et al., 2022).

Many sediment yield studies have been based on short-term (days to years) observations and thus do not necessarily reflect long-term ( $10^2 - 10^5$  years) rates (Spotila, 2022). It is, however, interesting to compare them with the long-term erosion rate for Moran Bay over the past 14.4 ka. The Moran Bay rate of  $0.004 \pm 0.001$  mm/yr is very low compared to similar-sized fluvial or glacial catchments but is similar to modern rates derived from small deglaciated basins (Fig. 1.7). In addition, it is notable that modern erosion rates of the larger ( $>1000$  km<sup>2</sup>) fluvial and paraglacial basins are similar, whereas in the smaller basins ( $<1000$  km<sup>2</sup>), paraglacial erosion rates plot well below the erosion rates of fluvial basins of the same size, suggesting that post-glacial fluvial inefficiency is not uncommon in small deglaciated basins. The difference in erosion rates for smaller catchments could imply that available discharge may play an important role in moving larger caliber debris. Reaches steep enough to erode down to bedrock followed by subsequent trapping of sediment on flattened steps were observed in Moran and Snowshoe Canyons, suggesting that the fluvial system has the discharge to move larger debris during floods but lacks the steepness to evacuate them out of the catchment.

### 1.5.3 Landscape, process, and equilibrium

The relative contributions of glacial, fluvial and colluvial processes to an equilibrium state between denudation and rock uplift change over long (multi-glacial cycle) or interglacial timescales. Numerical models suggest that glacial erosion rates can be higher than rock uplift rates when the topography is adjusting from fluvial to glacial conditions or if there is a shift in climate periodicity (e.g., Pedersen & Egholm, 2013). Once the glacial valley is carved and adjusted to glacial erosion, subsequent glaciers may not need to erode much bedrock to maintain this equilibrium (i.e., match rock uplift rates), but primarily transport the hillslope sediment deposited during the interglacial, and do a little erosion to maintain the valley shape (Herman & Braun, 2008; Leith et al., 2014), thus maintaining a glacial steady state (Deal & Prasicek, 2021). The similarity of the colluvial production rate and the long-term denudation rate in the Tetons indicates that hillslope processes are an essential contributor to the denudation of the Tetons over long timescales. In the Tetons, the larger basins ( $>20 \text{ km}^2$ ) have hosted glaciers capable of keeping pace with rock uplift and maintaining a shallow longitudinal valley profile (Foster et al., 2010). However, since the topography has adjusted to accommodate glaciation, glaciers may not produce substantial primary bedrock erosion along the valley bottoms as they do at higher elevations; thus, the mass efflux from the larger canyons is dominated by interglacial colluvial sediment production and eventual transport during the next glacial advance (Tranel et al., 2011). Hillslope processes, with glacial advances providing sediment transport, may be at least as important for attaining steady state as canyon incision (Brocklehurst & Whipple, 2007).



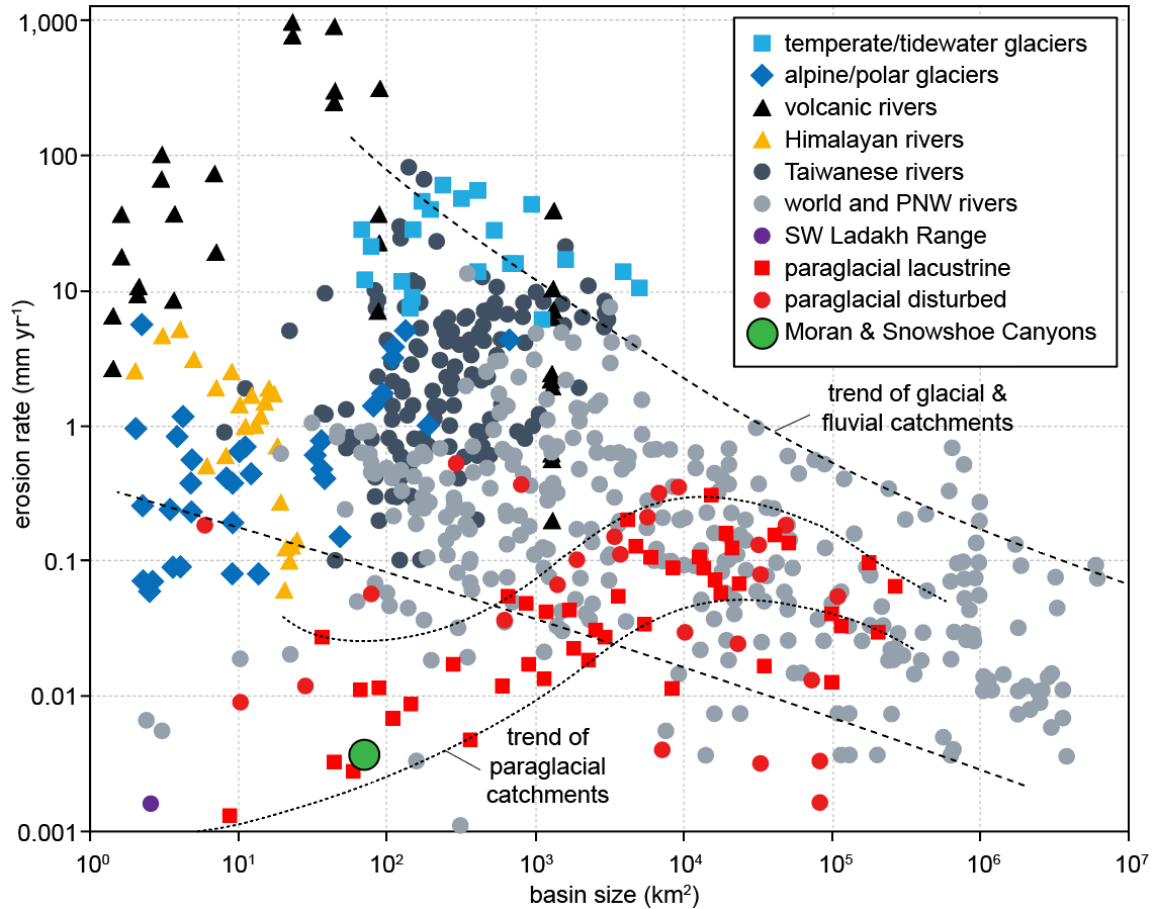


Figure 1.7. Erosion rates of fluvial, glacial and paraglacial catchments from Koppes and Montgomery (2009), Church and Slaymaker (1989) and Dietch et al. (2015). The erosion rate of Moran Bay of  $0.004 \pm 0.001$  mm/yr plots within the typical range for small paraglacial catchments.

While glacial and colluvial processes appear to have the capacity to equilibrate with uplift in the Tetons, the capacity of the fluvial system to equilibrate with uplift has been hampered because the valley profile has been flattened by glaciers. In fluvial-dominated landscapes, rivers govern the landscape response by setting local base level and controlling the hillslope angle needed for denudation rates to match rock uplift rates, which drives the channel systems toward graded equilibrium longitudinal profiles (Whipple et al., 2013). If perturbed by a change in a boundary condition, such as a change in base level due to fault slip, the fluvial system will respond by transiently adjusting to a new steady-state. For example, the longitudinal profile of a stream will work to adjust to fault slip through vertical incision and knickpoint migration (e.g. Whipple & Tucker, 1999). In the context of this study, the fluvial system has been “perturbed” by glacial erosion flattening the valley, to which the river system needs to transiently steepen to once again compete with rock uplift. Here, it is evident that the fluvial system is disequibrated by such a “glacial perturbation”, with interglacial fluvial processes yielding a post-glacial fluvial erosion rate of just  $0.004 \pm 0.001$  mm/yr, which



is far outpaced by the maximum uplift rate of 0.28 to 0.31 mm/yr for the Teton Range. The difference between sediment production in the canyons and sediment yield into the bay, means that ~97% of the canyon sediment cannot be transported until the next glacial advance, or the eventual relaxation of the catchment to a fluvial equilibrium landscape.

For rivers to respond to uplift they must have the right topographic conditions to do so effectively. Clearly, the erosive power of rivers in Moran and Snowshoe Canyons is significantly diminished by a landscape that is equilibrated for glacial (and colluvial) processes. In this paraglacial landscape, streams do not set limits on topography but instead are controlled by the post-glacial topography, thus illustrating the importance of the topographic signature as a boundary condition that governs landscape response to uplift.

#### 1.5.4 Post-glacial landscape longevity

The time required for a deglaciated valley to re-equilibrate to fluvial conditions is strongly controlled by both precipitation and catchment area (Hobley et al., 2010; Dortch et al., 2011), such that the fluvial system is too sluggish to re-equilibrate during interglacial periods. The time required to develop a classic U-shaped glacial valley that was previously dominated by fluvial processes has been estimated as < 100 ka (Harbor, 1992). However, the time required to return to a fluvially equilibrated system is far longer, requiring a minimum of 500 ka (Hobley et al., 2010) which is longer than the typical time interval between periods of ice advance (Tomkin, 2009). The lack of modern-day landscapes that are observed to be in transition from glacial to fluvial process dominance highlights the longevity of glacial landscapes (Spotila, 2022).

It is interesting to consider what the effects of a warming climate and the prolonged absence of glaciers might be on the Teton Range. Assuming footwall uplift continues due to slip on the Teton fault, the absence of major glaciers, and a consistent precipitation rate, the elevation of the Teton Range would be expected to increase until a threshold steepness is reached that yields efficient fluvial incision, perhaps eventually leaving a paleo-glacial “terrace” perched above the rejuvenated fluvial landscape. However, as past glaciers have been responsible for moving accumulated sediment out of the valleys and into the Snake River Valley, thus moving the sediment load across the Teton fault and onto the hanging wall, it is possible that the absence of major glaciers could cause a reduction in the rate of uplift, at least until fluvial processes attain the ability to move mass across the fault. Flattened valley profiles are typical of deglaciated catchments around the world. Future climate change and the loss of glaciers will produce more catchments with rivers lacking the capacity to transport sediment, which can potentially impact not only sediment flux, but uplift rates as well.

#### 1.6 CONCLUSIONS

The Teton Range is an ideal setting to quantify fluvial efficiency in a post-glacial landscape. All canyon-sourced sediment is captured in a lake formed by a glacial moraine, allowing a complete post-glacial sediment budget to be constructed. The

sediment budget was constructed using existing LiDAR data and newly acquired seismic profiles through Moran Bay. The flattened valley profiles of these catchments are typical of the Tetons, and of deglaciated catchments of similar size around the world. The catchment-wide sediment production rate of  $0.17 \pm 0.02$  mm/yr is close to the average catchment uplift rate and the long-term denudation rate of the Teton Range, illustrating the importance of hillslope processes to the overall denudation of the Tetons. This also implies that once topography is adjusted for glacial erosion, subsequent glaciers mostly transport accumulated sediment and may only need to provide some maintenance erosion of bedrock to maintain this equilibrium.

While the combination of glacial and colluvial processes can keep pace with uplift in the Tetons, the interglacial fluvial system cannot, as evidenced by the fact that only ~2.6% of the total post-glacial sediment volume has been transported to the bay. The fluvial system has been perturbed by glacial erosion flattening the valley profiles, reducing stream power and sediment transport capacity. The post-glacial fluvial erosion rate is just  $0.004 \pm 0.001$  mm/yr, which is far outpaced by the maximum uplift rate of 0.28 to 0.31 mm/yr for the Teton Range, illustrating that glacially-flattened valley profiles preclude fluvial efficiency.

Rivers require the right topographic conditions to respond to uplift. As the erosive capability of rivers in Moran and Snowshoe Canyons has been diminished by a landscape equilibrated for glacial erosion, the accumulating sediment will remain in the catchments until the next glacial advance, or until continued uplift along the Teton fault steepens the topography to make fluvial processes efficient once again. Thus, glacial topography is demonstrated to be not only a record of climate and tectonic dynamics, but an important boundary condition. It appreciably limits rates of denudation and sediment transport, and therefore the ability of the landscape to respond to uplift.

## 1.7 ACKNOWLEDGEMENTS

This work was supported by a UW-NPS seed grant and NSF-EAR 1932808, the Overcash Field Fund at UK, and UK student research grants. We would also like to acknowledge Cooper Cearly, Ryan Goldsby, Autumn Helfrich, Hillary Johnson, and Giliane Rasbold for their work in the field. Comments from two anonymous reviewers greatly improved an earlier version of this manuscript.

This work is published as:

Johnson, S. E., Swallom, M. L., Thigpen, J. R., McGlue, M. M., Dortch, J. M., Gallen, S., Woolery, E. W., Yeager, K., 2022, The influence of glacial topography on fluvial efficiency in the Teton Range, Wyoming (USA). *Earth and Planetary Science Letters* 592 (117643), <https://doi.org/10.1016/j.epsl.2022.117643>

## CHAPTER 2. MEASURING GROUND SURFACE ELEVATION CHANGES IN A SLOW-MOVING COLLUVIAL LANDSLIDE USING COMBINATIONS OF REGIONAL AIRBORNE LIDAR, UAV LIDAR, AND UAV PHOTOGRAMMETRIC SURVEYS

### 2.1 ABSTRACT

Slow-moving, chronically destructive landslides are projected to grow in number globally in response to precipitation increases from climate change, and land disturbances from wildfire, mining, and construction. In the Cincinnati and northern Kentucky metropolitan area, USA, landslides develop in colluvium that covers the steep slopes along the Ohio River and its tributaries. Here we quantify elevation changes in a slow-moving colluvial landslide over 14 years using county-wide lidar, uncrewed aerial vehicle (UAV) structure from motion (SfM) surveys, and a UAV lidar survey. Because the technology and quality differ among surveys, the challenge was to calculate a threshold of detectable change for each survey combination. We introduce two methods, the first uses propagated elevation difference errors, and the second back-calculates the individual survey errors. Thresholds of detection range from  $\pm 0.05$  to  $\pm 0.20$  m. Record rainfall in 2011 produced the largest vertical changes. Since then, the landslide toe has continued to deform, and the landslide has doubled its width by extending into a previously undisturbed slope. While this study presents a technique to utilize older datasets in combination with modern surveys to monitor slow-moving landslides, it is broadly applicable to other studies where topographic data of differing quality is available.

### 2.2 INTRODUCTION

Slow-moving landslides, which move at rates from just a few millimetres (mm) per year to several metres (m) per year (Lacroix *et al.* 2020b) are chronically destructive and permanently damage property, infrastructure, and agricultural land (Mansour *et al.* 2011; Nappo *et al.* 2019; Lacroix *et al.* 2020a). While rarely deadly themselves, they can be precursors to fast-moving catastrophic landslides (Palmer 2017; Handwerker *et al.* 2019) and thus provide a valuable opportunity to study landslide processes prior to more rapid movement. The development of slow-moving landslides may result from perturbations to a steadily creeping slope (Chau 1999). Slow-moving landslides often remain inactive for years or decades, only to experience periods of rapid movement in response to precipitation, human disturbance, or earthquakes (Lacroix *et al.* 2020b). With increases in precipitation due to climate change, and land disturbance due to wildfire, landslide activity is expected to increase in the United States (Leshchinsky *et al.* 2017; Mirus *et al.* 2017; Coe *et al.* 2018), and globally the number of landslides triggered by human activity such as construction and mining is increasing (Froude and Petley 2018). Within the United States alone, they are estimated to cost billions of dollars per year in economic losses (US Geological Survey 2005; Crawford 2014; Burns *et al.* 2017).

The purpose of the research we describe in this paper was to document and better understand decadal-scale spatial and temporal variations in the activity of a slow-moving landslide in the Cincinnati and northern Kentucky (USA) area, which necessarily included the development of an approach to integrate topographic data collected using different technologies over a period of years. Thus, this paper presents a methodology in a case study. Landslides throughout the area are well-known hazards but have not been studied intensively for nearly 30 years (Fleming and Taylor 1980; Haneberg 1991; Fleming and Johnson 1994; Haneberg and Gokce 1994; Riestenberg 1994; Baum 1994; Baum and Johnson 1996; Crawford 2014, 2012; Crawford and Bryson 2018; Glassmeyer and Shakoor 2021); perhaps because the landslides, while numerous and costly, are not deadly, and are treated largely as an ongoing maintenance problem. Thus, there are no published studies of the landslides incorporating modern remote sensing methods such as those we describe in this paper. The previous studies were also typically limited to a year or two in duration, so they did not provide information about decadal patterns of activity. This paper provides the first documentation of decadal Cincinnati and northern Kentucky area landslide movement based upon modern remote sensing techniques.

We describe a method to quantify the threshold of detectable change between digital elevation models (DEMs) produced using various remote sensing technologies. Here we use the United States Geological Survey (USGS) definition of a DEM, which is a bare-earth surface which excludes vegetation, buildings, and other surface objects. This is equivalent to a digital terrain model (DTM), as opposed to a digital surface model (DSM) which includes all surface features. After describing the method, we then use it to document changes in a slow-moving landslide near Taylor Mill in northern Kentucky over a 14-year period using a combination of (1) regional airborne lidar coverage acquired by government agencies before our study began and (2) site-specific SfM and UAV-lidar surveys acquired as part of our work. To calculate thresholds of detectable change for each pair of DEMs, we used the statistics of noise for the difference map in areas outside of the landslide, where no elevation change is reasonably inferred to have occurred. Elevation changes within the landslide are then measured relative to these no change areas. As we explain, this is a pragmatic approach useful in many cases of practical interest for which control points are limited or non-existent. We found that combinations of surveys yield a threshold of detection of  $\pm 0.05$  m to  $\pm 0.20$  m, depending on the combination, and that vertical changes in the landslide above the threshold of detection were found for every combination of surveys, even as short as SfM surveys performed two weeks apart. This approach is broadly applicable to other study areas with topographic and bathymetric data acquired using various technologies and of differing quality. Thus, this technique provides a method to utilize older survey datasets which may be regional scale and lower resolution in combination with site-specific high-resolution datasets to detect real elevation change over time.

We conclude that whereas the most significant movement of the Taylor Mill landslide—which formed on a slope altered by human activity—was triggered by record precipitation, the landslide has continued to move and expand laterally onto a previously unaltered slope. With climate change increasing precipitation regionally (EPA 2016), it is expected that landslide activity in the region will only increase, making the monitoring of slow-moving landslides a critical part of landslide mitigation.

### 2.2.1 Landslide Characteristics and Geologic Setting

The Cincinnati, Ohio and Northern Kentucky region (Fig. 2.1) is plagued by slow moving landslides that regularly threaten infrastructure (Mirus *et al.* 2017). For example, several 2019 landslides occurring along a major road cost over \$17 USD million and took two years to remediate (City of Cincinnati Transportation and Engineering 2019; Knight 2021). Landslides typical of the region include slow-moving debris slides, generally < 2m thick, that form in the colluvium, unconsolidated material weathered from the underlying bedrock, which covers the steep slopes along the Ohio River and tributary valleys (Varnes 1978; Fleming and Johnson 1994); and deeper, slow-moving slumps that occur on flatter slopes in thick colluvium, glacial deposits, or anthropogenic fill (Baum and Johnson 1996). The colluvium consists of weathered rock fragments ranging in size from granules to tabular limestone boulders in a clayey matrix. The colluvium most susceptible to landslides is derived from horizontally-bedded shale and limestone of the Ordovician Kope Formation (Fig. 2.1) which is composed primarily of weak illitic shale that slakes easily when exposed to water (Koralegedara and Maynard 2017). The landslide chosen for this study, referred to as the Taylor Mill landslide (39.034234, -84.512587), is a translational debris slide that has been active since at least 2003 and has impacted a slope and roadway leading to an apartment complex (Fig. 2.2). Attempts to mitigate the slide have included regrading the slope and rebuilding part of the roadway (Fig. 2.3). In 2012 the debris slide measured approximately 45 m wide and 70 m long and by 2021 it had more than doubled its width. If we assume a constant thickness of 1.5 m, the volume of the landslide was initially approximately 4500 m<sup>3</sup> and has expanded to 11500 m<sup>3</sup>.

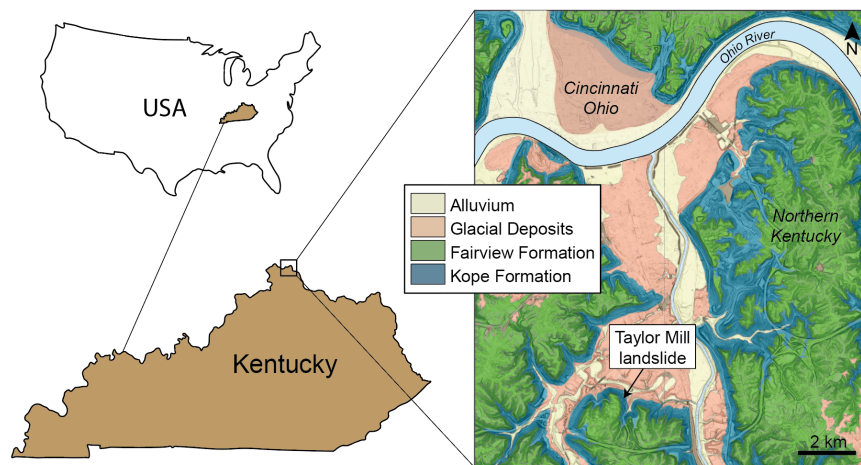


Figure 2.1. Location of the Taylor Mill landslide study area in northern Kentucky (39.034234, -84.512587). Cincinnati, Ohio, lies directly across the Ohio River from the study area.

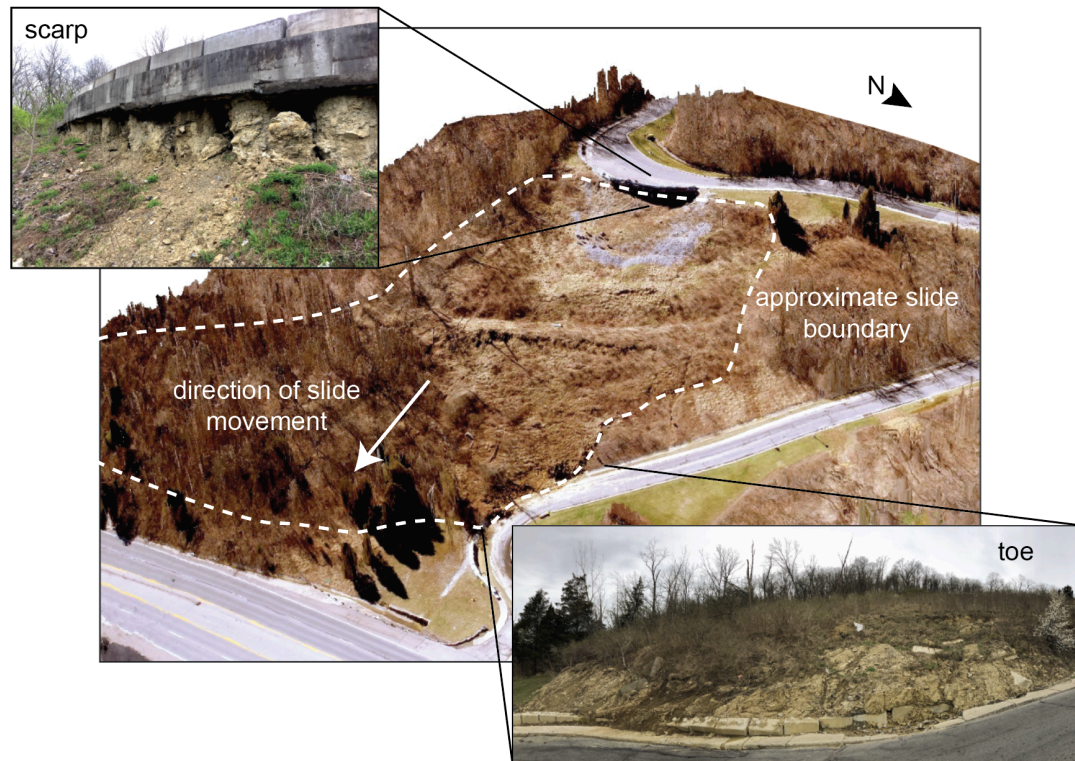


Figure 2.2. Landslide in Taylor Mill, Kentucky. Oblique view of slide generated from March 11, 2019 drone UAV imagery. The scarp has exposed the road foundation, and the toe has advanced into the road leading to an apartment complex. The two-lane road is approximately 6 metres wide. Photo of the scarp was taken April, 2018; photo of the toe was taken March, 2022.



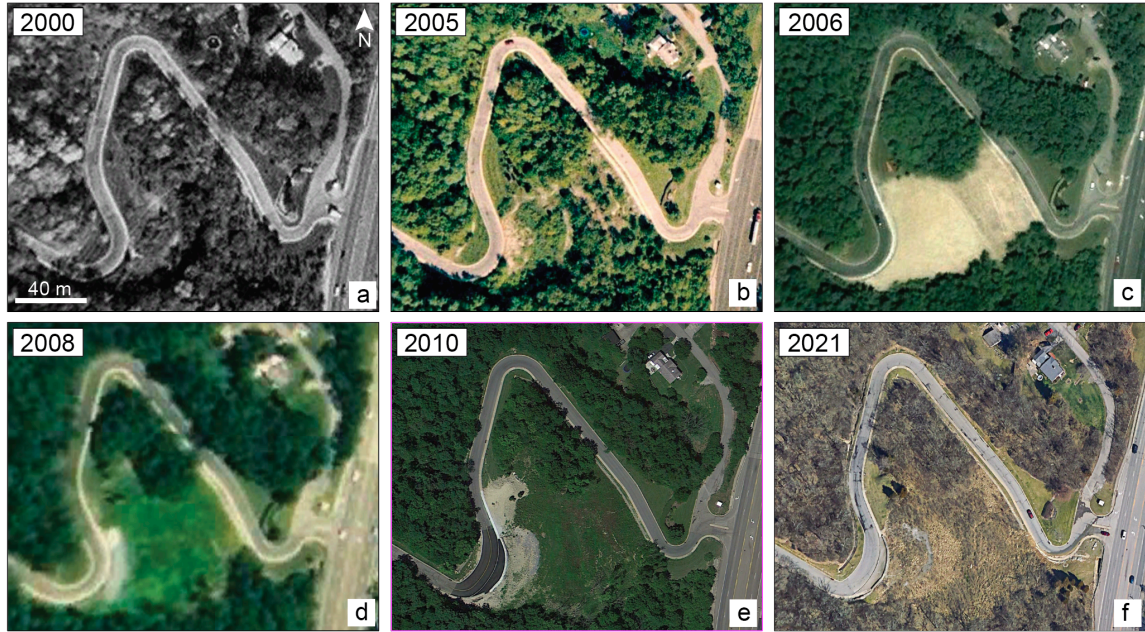


Figure 2.3. Sequence of images that illustrate the changes to the slope between 2000 and 2021 (Google Earth 2000, 2005, 2006, 2008, 2010, 2021). a) Image from October 2000 showing the driveway and vegetated slope. b) Image from August 2005 showing some bare patches on the previously vegetated slope. c) Image from June 2006 showing the regraded slope. d) Image from 2008 showing a bare patch at the top of the slope that may represent added fill. e) Image from July 2010 showing added fill and the reconstructed driveway at the top of the slope. f) image from March 2021 showing drainage from the toe of the landslide into the driveway.

## 2.3 METHODS

### 2.3.1 Change Detection

Aerial and satellite platforms have made it feasible to detect changes in slow-moving landslides with greater spatial and temporal resolution than with traditional methods such as field-based mapping or repeated surveys of benchmarks (Turner *et al.* 2015; Schulz *et al.* 2017; Okyay *et al.* 2019; Lacroix *et al.* 2020b). In particular, unoccupied aerial vehicle (UAV)-based lidar and structure-from-motion (SfM) photogrammetry have made data acquisition less expensive and easily repeatable over short time periods (Jaboyedoff *et al.* 2012). Because slow-moving landslides may be active for many decades, older elevation datasets, e.g. topographic maps, SRTM, or regional lidar, can also provide valuable past landslide information, albeit at lower spatial and temporal resolutions than site-specific SfM or lidar surveys.

A critical challenge in the study of elevation change detection, including slow-moving landslides, is addressing signal-to-noise ratios (Wheaton *et al.* 2009; Schaffrath

*et al.* 2015; James *et al.* 2017). Frequently monitored landslides often register changes so small that the elevation changes may not be greater than the survey errors, referred to as noise. There are many potential sources of digital elevation model (DEM) noise such as the incomplete density of observations, processing errors, measurement errors, and errors introduced by the interpolation of point cloud data (Wechsler 2007), all of which will propagate through derivative maps and calculations (Holmes *et al.* 2000; Haneberg 2006, 2008). Survey noise can be quantified for SfM surveys (Clapuyt *et al.* 2016; Goetz *et al.* 2018), and elevation data acquired from various spaceborne and airborne platforms (Haneberg 2006, 2008; Gonga-Saholiariliva *et al.* 2011). However, the noise for older elevation datasets may be unknown. Thus, combining surveys acquired with different technologies to detect decadal change in a landslide can be a challenge. Few studies have directly used multiple technologies acquired at different times to detect change (e.g. (Warrick *et al.* 2019)), and quantifying the minimum detectable change possible using combinations of technologies has rarely been explored (e.g. (Warrick *et al.* 2017)).

Although change detection is optimally based on comparing results obtained from remote methods with surveyed monument locations on the ground, it is not always practicably possible. For example, the study area may be inaccessible to surveyors, monuments may be vandalized or accidentally destroyed between surveys, or a study may use historical data that predate the installation of survey monuments. In our case, the first two lidar data sets were acquired 12 and seven years, respectively, before our work at the Taylor Mill site began and no historical survey monument data were available. To compensate for the lack of survey monuments, we expand upon an approach based upon the statistics of inferred areas of no change proposed by Haneberg (2017), whereby we quantify the noise in areas outside of the landslide where no elevation change has occurred, in order to calculate the threshold of detectable change. Elevation changes in the landslide above this threshold are measured relative to the no change areas outside of the landslide. If the no change area is indeed moving, then the calculated changes in the landslide are not absolute. However, they will still be very useful for understanding the movement of the landslide.

We measured changes in the landslide surface between 2007 and 2021 using differences between pairs in a series of: 1) DEMs from county-wide airborne lidar surveys conducted in 2007 and 2012, 2) SfM DEMs derived from photographs acquired by a UAV in 2019 and 2020, and 3) a lidar DEM created from a UAV-lidar point cloud acquired in 2020. Each DEM was adjusted to the 2012 lidar DEM by removing coherent noise in the form of bias (an elevation difference of the same magnitude across the map area) and tilt (a systematic change in elevation difference across the map area) as described in detail below. The 2012 lidar data set was chosen instead of the 2007 lidar data set because it has a denser point cloud and fewer obvious artifacts compared to the 2007 data. Once bias and tilt between datasets were removed, we calculated the threshold of detectable elevation change for each pair of DEMs using the statistics of errors in areas outside of the landslide where no elevation change is thought to have occurred using two methods. The methods are summarized in Figure 2.4 and described in detail in the following paragraphs.



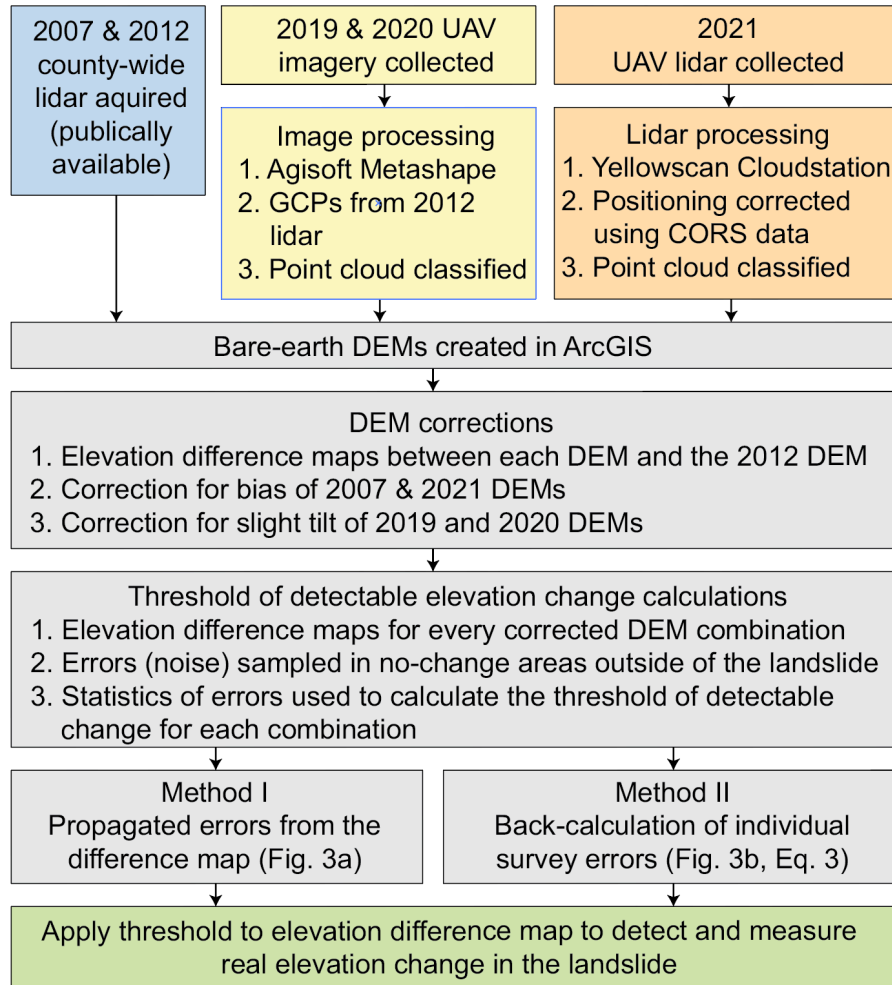


Figure 2.4. The flowchart summarizing the data acquisition and processing of the county-wide lidar, UAV-SfM imagery, and UAV-lidar; the corrections to the DEMs for bias and tilt; and the methods used to estimate the threshold of detectable change.

### 2.3.2 Data Acquisition

The county-wide lidar data and aerial photographs used in our analysis were obtained during leaf-off conditions in the winter of 2007 and 2012 (Table 2.1). The 2007 lidar data covering Northern Kentucky were obtained by the Northern Kentucky Planning Commission, and has an average point spacing of 1.6 m. The 2012 lidar data and photographs were acquired as a part of the Kentucky Aerial Photography and Elevation Data Acquisition program (KYAPED). The 2012 lidar data were collected at an average of 0.68 m point spacing or better, and a required vertical accuracy of  $\pm 0.15$  m or better. The 2012 aerial photographs have 0.15 m pixels. The 2012 and 2007 lidar data were originally delivered in Kentucky state plane coordinates in feet; we projected them from state plane coordinates to UTM Zone 16N coordinates in metres and converted the vertical units from feet to metres. The Kentucky state plane and UTM coordinate systems

both use the same horizontal datum (NAD 1983) and ellipsoid (GRS 1980), thus errors introduced by this projection are negligible.

Table 2.1 Methods and dates of data acquisition.

Date	Method	Referenced in paper as	Average point spacing (m)
Winter 2007	County-wide lidar	2007	1.6
Winter 2012	County-wide lidar	2012	0.68
March 11, 2019	UAV-SfM	2019	0.046
March 26, 2019	UAV-SfM	2019, 2nd survey	0.044
March 3, 2020	UAV-SfM	2020	0.040
December 15, 2020	UAV-lidar	2021	0.049

We acquired digital aerial photographs for the SfM surveys in 2019 and 2020 using Mavic Phantom 2 and Mavic Pro UAVs. Flights were planned with DroneDeploy software (Hinge *et al.* 2019) to ensure that the images had 75% front overlap and 70% side overlap.

Our UAV-lidar data were acquired using a Matrice 600 Pro UAV and Yellowscan Surveyor lidar system in December 2020. Flights were planned using UgCS software to follow the topography at an elevation of 40 metres. The lidar flight extended farther to the south than the 2019 and 2020 SfM surveys to include a heavily vegetated area where the SfM surveys did not produce usable results.

### 2.3.3 Data Processing

The photographs for the SfM survey were processed to produce point clouds using Agisoft Metashape (James *et al.* 2017), and georeferenced using 19 easily identifiable ground control points (GCPs) in areas outside of the landslide where no change was inferred to have occurred. GCPs were selected using the coordinates of reference points such as sewer grates and light poles visible in the KYAPED 2012 aerial photographs and the corresponding elevations from the 2012 lidar-derived DEM. After image alignment, the total residual error for the GCPs is < 0.02 m. Point clouds were classified in Metashape using the Classify Ground Points tool, using a maximum angle of 15 degrees, maximum distance of 0.5 m, and cell size of 50 m. The SfM point clouds have an average point spacing of 0.040 to 0.046 m (Table 2.1).

The UAV lidar data were post-processed using local Continuously Operating Reference Station positioning data to improve their spatial accuracy (Olsen *et al.* 2013). Point elevations were further improved using strip adjustment and classified into ground and non-ground points using Yellowscan CloudStation software. The point cloud has an average point spacing of 0.049 m.

Point clouds from the county-wide lidar, SfM, and UAV-lidar were processed using ArcGIS to produce 0.1 m DEMs using natural neighbor interpolation, a technique used to construct a surface from irregularly distributed points, in order to fill voids (Sibson 1981). Although interpolating the two county-wide lidar DEMs to 0.1 m does not add information or increase the resolution of features, it does facilitate comparison with the more detailed SfM and UAV-lidar DEMs. While geomorphological change can be quantified from digital elevation data using grid-based (DEM) or point cloud comparisons (e.g. (Qin *et al.* 2016; Okyay *et al.* 2019)), we used gridded DEMs in this research because calculating DEM differences is easily performed using map algebra within GIS software and has a long history of successful application in geomorphological change detection studies (e.g. (Okyay *et al.* 2019)). An area of interest (AOI) was used to define the processing extent so that all DEM grids would be aligned. Without this step, the DEM grid would originate at the southeasternmost point of each point cloud, and thus the grid for each dataset would be slightly different. All datasets are georeferenced in UTM Zone 16N, EPSG 26916.

#### 2.3.4 Noise Maps

Coherent noise in the forms of bias and tilt between each DEM and the 2012 DEM was visually assessed using noise maps. The 2012 DEM was chosen as the surface that all other DEMs were corrected to because it was better quality than the 2007 DEM, and also had high quality aerial photographs taken at the same time, and thus allowed ground control points to be selected for processing the SfM data. Noise maps were symbolized to show apparent elevation differences only in the range of  $\pm 0.20$  m to visualize just the noise in areas where no real elevation change between data sets is expected (no-change areas). The range of  $\pm 0.20$  m was chosen because it produces a continuous display of noise values across the map area. The noise was then quantified by sampling the distribution of noise in the road above and below the landslide.

#### 2.3.5 Correction for bias and tilt

Each of the DEMs we used required some correction of either bias (between lidar DEMs) or tilt (between SfM DEMs). Ideally, the mean elevation change in a no-change area should be zero; thus, a non-zero mean indicates a bias between the datasets. This bias was removed by adding or subtracting the calculated mean value from the DEM being corrected. To adjust the slight tilt observed in the SfM DEMs, the apparent elevation difference for each of a series of 30 points along the road above and below the landslide was used to create a correction surface using the Topo-to-Raster tool in ArcGIS, which uses an iterative finite difference interpolation technique. This correction surface was then subtracted from the DEM being adjusted to remove the tilt. The corrections for bias and tilt remove the coherent noise and the remaining random noise is then used to calculate the threshold of detectable change between the two datasets.

### 2.3.6 Threshold of elevation change detection

When two elevation surveys are noisy and are then combined to calculate an elevation change, the errors are larger than the sum of the errors in each individual survey, which is often referred to as the propagation of errors (Birge 1939). Previous researchers have used probabilistic geomorphic change detection thresholds based upon the propagation of elevation errors from each of the two DEMs being compared (Brasington *et al.* 2000; Lane *et al.* 2003; Schaffrath *et al.* 2015). However, there may be cases of practical interest in which the individual DEM elevation errors are not available. For example, it is generally not feasible to directly determine DEM errors in deep-water seafloor change detection studies based upon repeat multibeam echosounder surveys (e.g. (Haneberg 2018)). Likewise, it is not unusual to encounter situations such as the one we describe in this paper, in which some of the DEMs were produced before our research began. Even if quality assurance statistics are available for previous topographic surveys, those data are typically collected in unobstructed, smooth, and flat areas that are not representative of heavily vegetated, rough, and steep landslide terrain. Such quality assurance error statistics can be misleading because DEM errors in areas relevant to landslide studies can easily be an order of magnitude larger than those collected for quality assurance purposes (e.g. (Haneberg 2006, 2008)). To account for those difficulties, we use two methods that combine error propagation theory with geomorphologically reasonable assumptions about areas in which no change is expected to have occurred. The elevation changes in the landslide that we report are relative to the no change areas, which we assume has an elevation change of zero.

Both of our methods are based upon estimates of the propagated elevation difference error rather than the individual DEM elevation errors. This requires geomorphologically informed selection of one or more areas in which significant change can be reasonably inferred not to have occurred. We refer to those as no-change areas. Areas in the road above and below the landslide were used as no-change areas because there were no measurable elevation changes in these areas between 2007 and 2021 either due to the nearby landslide or alterations to the road such as repaving. The propagated elevation difference error is estimated by calculating the mean and standard deviation of the DEM difference values within the no-change area(s) or, if the area is large, a subset of the values within the no change area(s). In an ideal situation, the no change data would be noise- or error-free; both the mean and standard deviation would be zero. Non-zero results for a no-change area are thus an estimate of the propagated elevation error. The mean, or bias, is removed to create a zero-mean no-change dataset. The remaining non-zero standard deviation,  $\sigma_{\Delta z}$ , is an estimate of the total propagated elevation error if the no-change inference is valid. The standard deviation of the propagated elevation errors is related to the individual DEM elevation errors by

$$\sigma_{\Delta z}^2 = \sigma_{z,t1}^2 + \sigma_{z,t2}^2 \quad (1)$$

where  $\sigma_{z,t1}$  and  $\sigma_{z,t2}$ , are the standard deviations of the elevation errors in DEMs representing times  $t_1$  and  $t_2$ , respectively (e.g. (Hildebrand 1987; Brasington *et al.* 2000; Lane *et al.* 2003; Schaffrath *et al.* 2015)). Next, we calculate the threshold value of

detectable change using the propagated elevation difference error using two methods. Method I uses the statistics of errors from the difference map, while Method II uses back-calculated error estimates for each individual survey.

### 2.3.6.1 Method I: difference map errors

We assume that the DEM difference errors are normally distributed with a zero mean and heuristically adopt a threshold of  $\pm 2\sigma_{\Delta z}$ , so that probability of a calculated elevation change being noise is  $< 0.05$  (Fig. 2.5a). This is essentially the same approach taken by (Brasington *et al.* 2000; Lane *et al.* 2003; Schaffrath *et al.* 2015) except that equation (1) allows us to use the no-change area estimate of propagated error rather than the individual DEM errors. We also round the multiplier up from 1.96 to 2 for convenience.

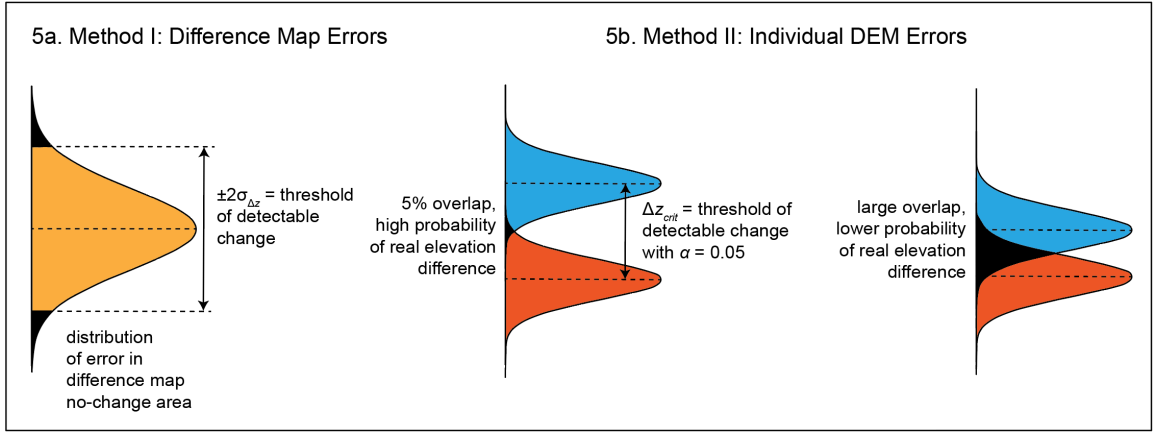


Figure 2.5. An illustration of the two methods to estimate the threshold of detectable change. (a) Method I uses the propagated errors from the difference map to estimate the threshold. (b) Method II uses an estimate of the individual DEM errors to calculate the threshold value that must be exceeded for the overlap between the two individual DEM error distributions to remain below a specified probability.

### 2.3.6.2 Method II: individual DEM errors

We calculate a threshold value that must be exceeded for the overlap between the two individual DEM error distributions to remain below a specified significance level,  $\alpha$ , as shown schematically in Fig. 2.5b. If both component error distributions are known,  $\alpha$  can be calculated numerically for any kind of distribution. For the work we describe in this paper, neither distribution is known. If it is reasonable to assume that both distributions are normal and have the same standard deviations,  $\sigma_z = \sigma_{z,t1} = \sigma_{z,t2}$  either of the cumulative distribution functions can then be evaluated at a value of one-half the threshold and the result doubled to obtain

$$\Delta z_{crit} = 2^{3/2} \sigma_z \operatorname{erfc}^{-1}(\alpha) \quad (2)$$

where  $\Delta z_{crit}$  is the elevation difference threshold that must be exceeded to ensure the overlap between the two distributions is less than  $\alpha$ ,  $\sigma_z$  is the standard deviation of the individual DEM errors, and  $\text{erfc}^{-1}$  is the inverse complementary error function. For a normal distribution of errors with a mean of 0 and a standard deviation of  $1/\sqrt{2}$ , the error function  $\text{erf } z = 2 \frac{z}{\sqrt{\pi}} \int_0^z e^{-t^2} dt$  gives the probability that the error lies within  $\pm x$ ; the inverse complimentary function  $\text{erfc}^{-1}$  uses the probability  $\alpha$  to find  $\pm x$ . Assuming that both DEM error standard deviations are equal, equation (1) can be rearranged to yield  $\sigma_z = \sigma_{\Delta z}/\sqrt{2}$  and equation (2) can be rewritten in terms of the difference map standard deviation rather than the individual DEM standard deviation:

$$\Delta z_{crit} = 2 \sigma_{\Delta z} \text{erfc}^{-1}(\alpha) \quad (3)$$

For the significance level  $\alpha = 0.05$ , or 95% confidence level, which is commonly used in many scientific studies,  $\Delta z_{crit} = 2.77 \sigma_{\Delta z}$ . Once the threshold values for each DEM combination are calculated, threshold maps are symbolized with a neutral color representing values under that threshold.

### 2.3.7 Magnitude of vertical change

We use the magnitude of vertical change between the corrected DEMs integrated over a specified sample in the center of the landslide area to quantify the amount of vertical surface deformation between each pair of DEMs. The magnitude of vertical change is the sum of the absolute value of the maximum change in each 0.1 m by 0.1 m cell in the sample area. We did not conduct a volume analysis on the landslide because unknown volumes of material have been added to and removed from the slide. An unknown volume of fill was placed on the top of the slope during road reconstruction between 2007 and 2012. As the landslide has repeatedly run out over the roadway, the toe has been excavated multiple times, removing an unknown volume of material.

## 2.4 RESULTS

### 2.4.1 DEM Corrections

Each dataset required correction to vertically align it with the 2012 DEM (Fig. 2.6, Table 2.2). The 2007 county-wide lidar DEM and the 2021 UAV-lidar DEM were corrected for a bias of 0.057 and 0.058 m, respectively. All three SfM DEMs were corrected for tilt of up to  $\pm 0.21$  m across the map area. Figure 2.6 shows examples of noise maps and noise distributions in no-change areas outside of the landslide. Figures 2.6a and 2.6b show an example of the noise map before and after correction for bias between the 2012 county-wide lidar DEM and the 2021 UAV-lidar DEM. Figures 2.6c and 2.6d show an example of the noise map and noise distribution before and after correction for the tilt between the 2019 SfM DEM and the 2012 lidar DEM.

Table 2.2 Results of noise analysis and the thresholds of elevation change detection prior to and after corrections using Method I and Method II, and the sum of elevation change in the landslide for each survey combination. Each DEM was corrected for tilt or bias so that areas outside of the landslide matched the 2012 county-wide lidar DEM. The first DEM column is the older dataset, and the second DEM is the more recent dataset.

First DEM	Second DEM	Noise before correction (m)	Threshold before correction (m)		Noise after correction (m)	Threshold after correction (m)		Magnitude of vertical change in landslide ( $\times 10^2$ m)
			Method 1 ( $\pm 2\sigma$ )	Method 2 ( $\Delta z_{\text{crit}}$ )		Method 1 ( $\pm 2\sigma$ )	Method 2 ( $\Delta z_{\text{crit}}$ )	
2007	2012	$-0.057 \pm 0.062$	$\pm 0.12$	$\pm 0.17$	$0.000 \pm 0.062$	$\pm 0.12$	$\pm 0.17$	708
	2019	$-0.027 \pm 0.068$	$\pm 0.14$	$\pm 0.19$	$-0.004 \pm 0.066$	$\pm 0.13$	$\pm 0.18$	860
	2019 2 <sup>nd</sup> survey	$-0.051 \pm 0.095$	$\pm 0.19$	$\pm 0.26$	$-0.017 \pm 0.073$	$\pm 0.15$	$\pm 0.20$	853
	2020	$0.012 \pm 0.064$	$\pm 0.13$	$\pm 0.18$	$0.003 \pm 0.061$	$\pm 0.12$	$\pm 0.17$	916
	2021	$-0.003 \pm 0.068$	$\pm 0.14$	$\pm 0.19$	$-0.004 \pm 0.068$	$\pm 0.14$	$\pm 0.19$	886
2012	2019	$0.034 \pm 0.033$	$\pm 0.07$	$\pm 0.09$	$0.000 \pm 0.031$	$\pm 0.06$	$\pm 0.09$	243
	2019 2 <sup>nd</sup> survey	$0.073 \pm 0.108$	$\pm 0.22$	$\pm 0.30$	$-0.013 \pm 0.043$	$\pm 0.09$	$\pm 0.12$	235
	2020	$0.074 \pm 0.027$	$\pm 0.06$	$\pm 0.08$	$0.007 \pm 0.025$	$\pm 0.05$	$\pm 0.07$	294
	2021	$0.058 \pm 0.026$	$\pm 0.05$	$\pm 0.07$	$0.000 \pm 0.026$	$\pm 0.05$	$\pm 0.07$	300
2019	2019 2 <sup>nd</sup> survey	$0.039 \pm 0.118$	$\pm 0.24$	$\pm 0.33$	$-0.012 \pm 0.045$	$\pm 0.09$	$\pm 0.13$	7
	2020	$0.039 \pm 0.037$	$\pm 0.08$	$\pm 0.10$	$0.007 \pm 0.026$	$\pm 0.05$	$\pm 0.07$	119
	2021	$0.023 \pm 0.037$	$\pm 0.08$	$\pm 0.10$	$0.000 \pm 0.039$	$\pm 0.08$	$\pm 0.11$	155
2019 2 <sup>nd</sup> survey	2020	$0.064 \pm 0.086$	$\pm 0.17$	$\pm 0.24$	$-0.020 \pm 0.047$	$\pm 0.09$	$\pm 0.13$	169
	2021	$0.047 \pm 0.086$	$\pm 0.17$	$\pm 0.24$	$0.012 \pm 0.050$	$\pm 0.10$	$\pm 0.14$	147
2020	2021	$-0.016 \pm 0.033$	$\pm 0.07$	$\pm 0.09$	$-0.007 \pm 0.036$	$\pm 0.07$	$\pm 0.10$	105

#### 2.4.2 Threshold of Detectable Change

Table 2.2 shows thresholds of detectable change prior to and after corrections for bias and tilt for all DEM combinations. In ten of the fifteen combinations, the threshold of detectable change was reduced by up to 0.20 m after corrections; in two combinations, the threshold of detectable change increased by  $< 0.01$  m, and in three combinations, there was no change in the threshold value. After corrections, the threshold of detectable change ranges from  $\pm 0.05$  to  $\pm 0.20$  m, with the largest thresholds resulting from combinations that include the 2007 county-wide lidar DEM.

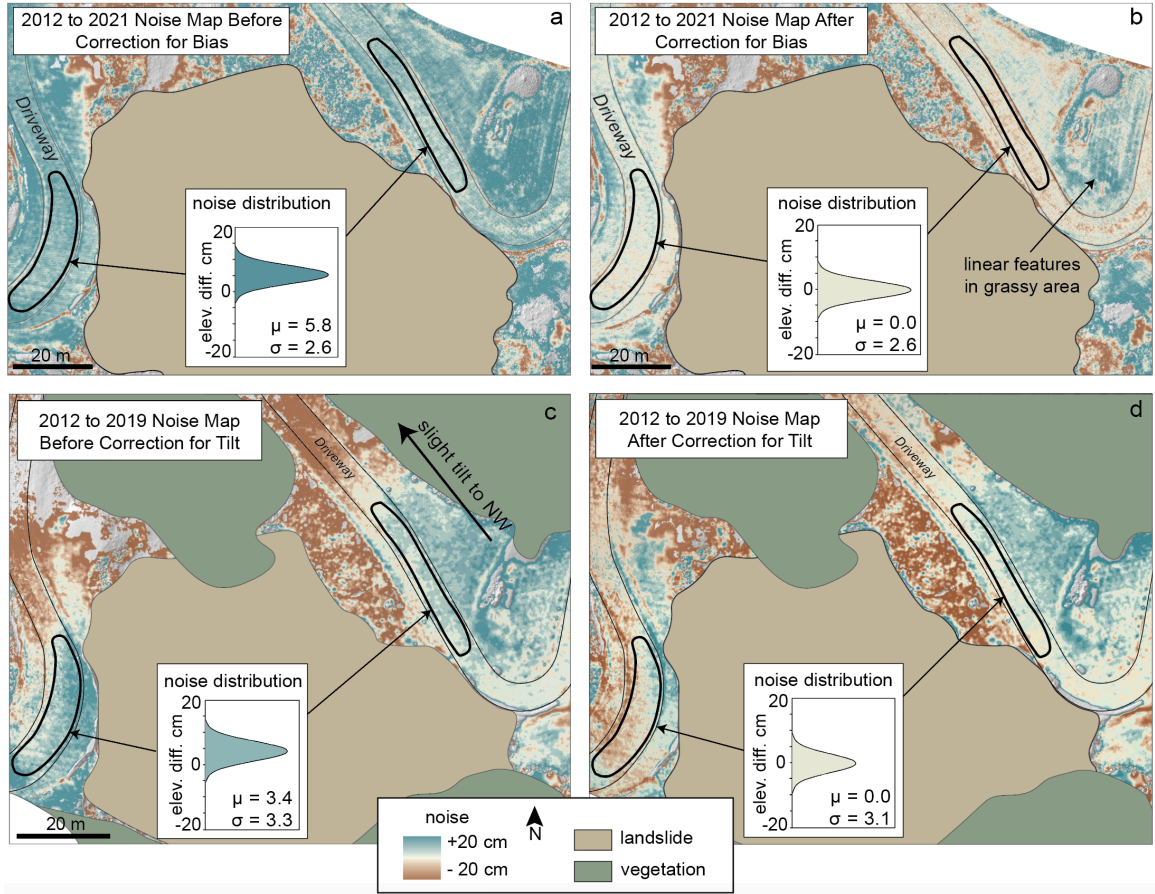


Figure 2.6. Examples of noise maps and noise distributions in no-change areas above and below the landslide before and after corrections for bias and tilt. (a) Noise map and distribution showing bias between the 2012 county-wide lidar DEM and the 2021 UAV-lidar DEM. (b) Noise map and distribution after the correction. Note there is still noise in the vegetated areas below the slide, and linear features in the mowed grassy area on the other side of the driveway. (c) Noise map and distribution showing a tilt of the 2019 SfM DEM of up to  $\pm 0.20$  m dipping to the NW. (d) Noise map and distribution after correction for tilt.

The threshold of detectable change calculated using Method I is always inherently smaller than Method II. For our datasets, the difference between the two methods ranges between 0.02 and 0.09 m, depending on the combination (Table 2.2). Threshold maps don't change underlying data, just the way it is symbolized, with a neutral color representing elevation change under the threshold value. Figure 2.7 shows an example of the threshold maps resulting from Method I (Fig. 2.7a) and Method II (Fig. 2.7b) applied to the 2019 and 2020 SfM DEMs. Method I results in a calculated threshold of 0.05 m, and Method II results in a threshold of 0.07 m.



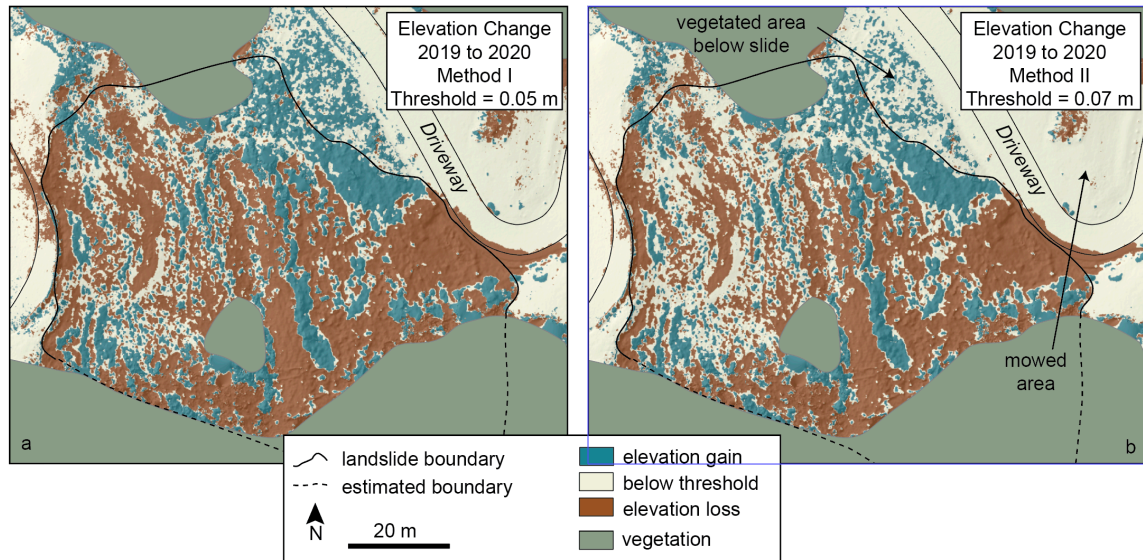


Figure 2.7. Threshold maps produced for the same DEM combination (the 2019 and 2020 SfM DEM) using Method I and Method II. **(a)** Threshold of 0.051 m calculated using Method I. **(b)** Threshold of 0.071 m calculated using Method II. Noise in the road and mowed area is reduced using either method, while there are more notable differences in the vegetated area below the slide and within the slide itself.

### 2.4.3 Vertical Changes in the Landslide Surface

Real elevation change in the landslide is detected in every combination of surveys, including those flown just two weeks apart. Elevation changes in the landslide are measured relative to the no change areas, which have an assumed elevation change of zero. Figure 2.8 shows a sequence of maps showing elevation changes in the landslide between 2007 and 2021 using a gradational scale. Elevation profiles that show the progressive elevation change between 2007 and 2021 in the landslide are shown in Fig. 2.9. Observations of elevation change in the landslide are summarized as follows:

- Between 2007 and 2012 (Figs. 2.8a, 2.9a), a landslide approximately 45 m wide and 70 m long developed in fill that had been placed on the slope. During this time, the head of the landslide dropped up to 2.2 m while the toe rose up to 1.3 m.
- Between 2012 and 2019 (Figs. 2.8b, 2.9b), most of the landslide continued to change in elevation. The top half of the slide shows some bands of elevation gain and loss that parallel the slope contours, while the toe mostly gains in elevation up to 1.2 m. In addition, a new area to the south lowered in elevation up to 1.2 m, though the lateral extent is obscured by vegetation and the topography could not be determined from the SfM data.

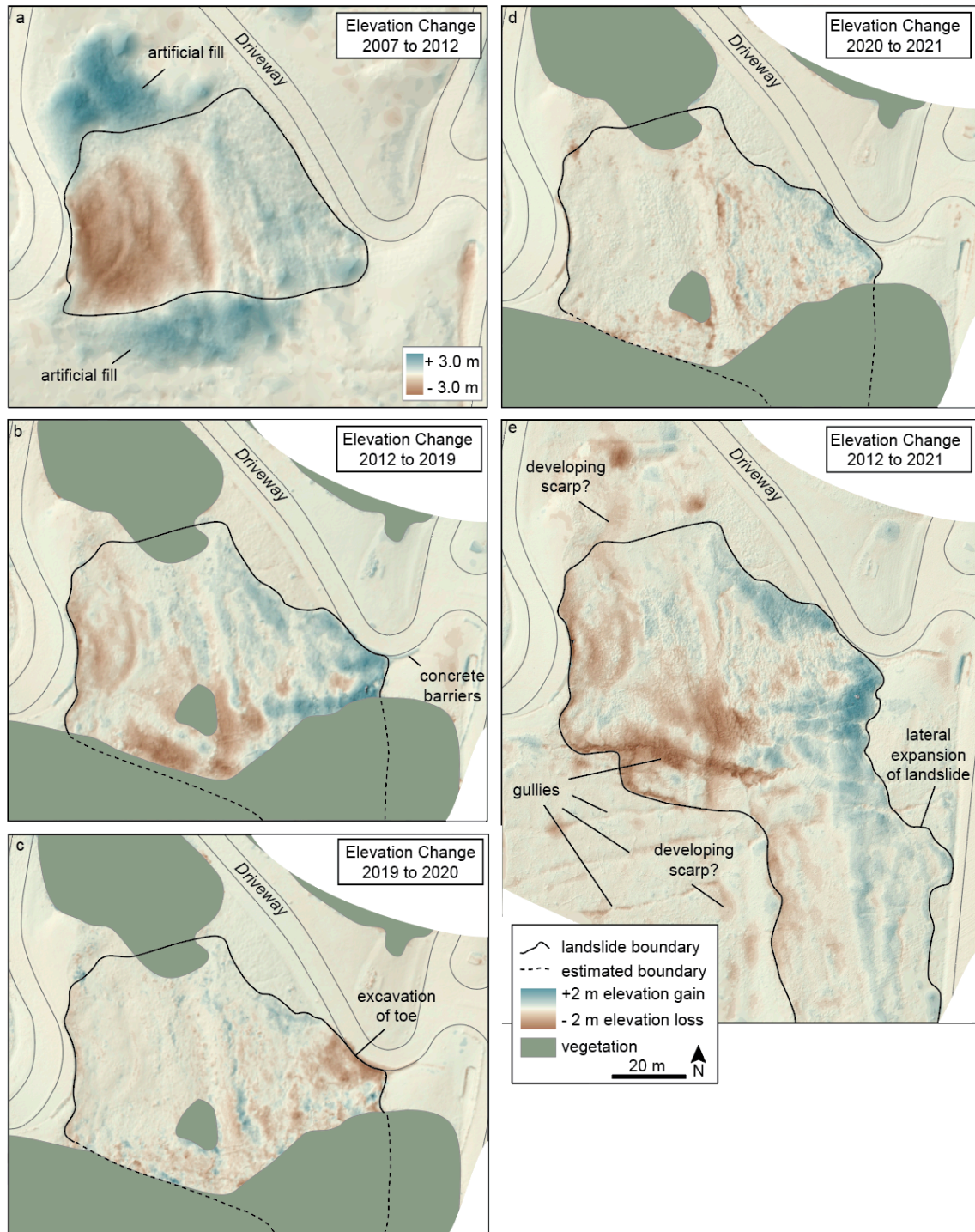


Figure 2.8. Elevation change maps using a gradational scale to show differences between (a) 2007 (county-wide lidar) and 2012 (county-wide lidar), (b) 2012 (county-wide lidar) and 2019 (SfM), (c) 2019 (SfM) and 2020 (SfM), (d) 2020 (SfM) and 2021 (UAV-lidar), and (e) 2012 (county-wide LiDAR) and 2021 (UAV-lidar).

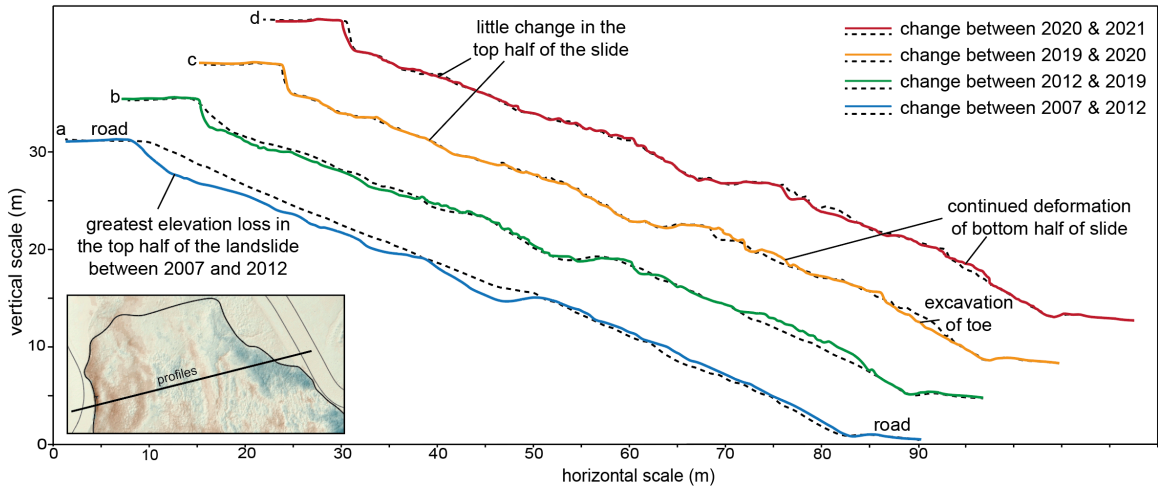


Figure 2.9. Topographic profiles through the landslide showing elevation change in the landslide between 2007 and 2021. The dashed profiles indicate the topography at the beginning of each time increment and the colored profiles indicate the topography at the end of each increment.

- Between 2019 and 2020 (Figs. 2.8c, 2.9c), the top half of the slide again shows parallel bands of small elevation gains and losses. Larger elevation changes are seen in the lower half of the slide, including the excavation of the toe near the road which lowered the elevation there up to 1.8 m, while the northern part of the toe gained elevation of up to 0.9 m.
- Between 2020 and 2021 (Figs. 2.8d, 2.9d), elevation changes of up to 1.1 m are seen in the lower half of the landslide, while the upper half of the landslide appears to have little to no vertical change.
- Difference maps showing the elevation change between lidar DEMs in 2012 and 2021 (Fig. 2.8e) allow a view of the ground beneath the vegetation and show that the landslide has extended to the south by at least 60 metres along the lower portion of the slope. Gullies can be observed above, below and across the body of the landslide. Other areas of smaller elevation changes are seen to the north of the slide boundary, and in the mid-slope area above the southern part of the slide.

The sum of the positive elevation gains and the absolute value of negative elevation losses inside the landslide sample area for each combination of DEMs is shown in Fig. 2.10, along with annual rainfall between 2005 and 2021. The rate of elevation change is greatest between 2007 and 2012, which coincides with the annual rainfall in 2011 of 1.86 m, the greatest annual rainfall since precipitation records have been collected starting in 1871. The rate of elevation change is also greater between 2019 and 2021. When positive and negative elevation changes are viewed individually (Fig. 2.10c and 2.10d), the rate of elevation gain is similar in all combinations, while the rate of elevation loss is greatest between 2007 and 2012, and between 2019 and 2021.



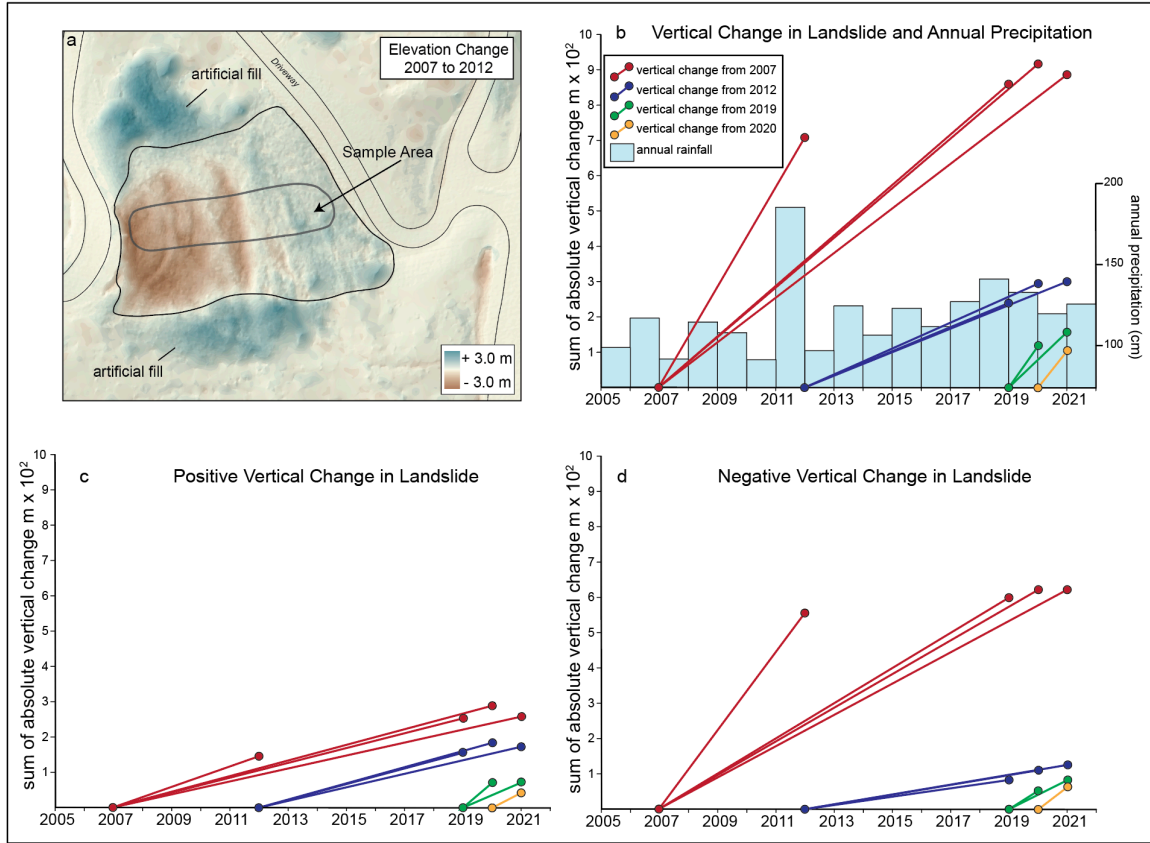


Figure 2.10. The magnitude values for each DEM combination are calculated by summing the positive elevation gains with the absolute value of elevation losses for each square metre in the sample area. (a) landslide sample area (b) the sum of the positive elevation gains and the absolute value of the negative vertical losses in the landslide sample area, and annual precipitation from 2005 to 2021. (c) the sum of positive elevation gains in the landslide sample area. (d) the sum of the absolute values of negative elevation loss in the landslide sample area.

## 2.5 DISCUSSION

### 2.5.1 Threshold of detection

Establishing thresholds of detectable change is important for two reasons. First, it provides a way to utilize older or noisy low-resolution datasets in combination with more recent higher-resolution datasets to detect real change and offer information about the behavior of slow-moving landslides over many years to decades. In this study, without the 2007 data, one might recognize a landslide from the topographic signature in the 2012 data, but we would not have information about the timing or magnitude of the change in the landslide. The methods of calculating the threshold presented here are broadly applicable to a wide range of topographic and bathymetric change detection problems using combinations of DEMs from different sources and for which limited control points

may be available. Using the statistics of noise in no-change areas from the difference map, one can simply use Method I to calculate the threshold of detectable change. Method II, which always produces a higher threshold than Method I, can also be used, however Method II uses the assumption that the standard deviation of noise is equal for both data sets. If the older data have a markedly different standard deviation of errors, Equation (1) can be used to calculate the propagated error, which would require knowledge or estimation of the standard deviations, or at least the ratio of standard deviations for each dataset. This propagated error can then be used in Equation (3) to calculate the threshold of detectable change.

Second, calculating a threshold of change can allow for more reliable and cost-effective monitoring of ongoing changes in slow-moving landslides. In this study, annual changes to the landslide are easily detectable with either SfM or lidar, and the slight corrections we demonstrated here to reduce the threshold of detection may not even be necessary to accomplish this. However, in the case where critical infrastructure may be damaged by a slow-moving landslide, monitoring for small changes may be a crucial mitigation strategy; thus, a technique to quantify and minimize the threshold of detectable change, including making the small corrections for tilt and or bias, is important.

An example of a small change in the landslide only detectable after making corrections and using the resulting threshold is provided by the combination of surveys collected just two weeks apart on March 11, 2019 and March 26, 2019. Before corrections to the individual DEMs, the threshold of detectable change was 0.33 m (Method II), in which case there was no detectable change in the slide beyond the excavation of the toe (Fig. 2.11a). Once corrections were made to each DEM, the threshold of detectable change was lowered to 0.13 m (Method II), and small changes within the landslide become apparent (Fig. 2.11b). A comparison with a combination of DEMs after an additional nine months had passed shows these small changes correlate with the pattern of elevation change over that longer time period (Fig. 2.11d).

The bias between lidar DEMs or tilt between SfM DEMs were easily identified using the noise maps. The pattern of tilt, in particular, would have been easily obscured without the noise maps. In this case, samples of noise in the road would show inconsistent distributions of errors across the map area; or if a single noise measurement was made of the area outside of the slide, errors with a large standard deviation, and thus a larger threshold of detection would be calculated.

When vertical changes in the landslide are large compared with the noise, they are easy to distinguish even without reliance on a formally calculated threshold. When the changes are small, however, minimizing the threshold of detection is critical for distinguishing real change.

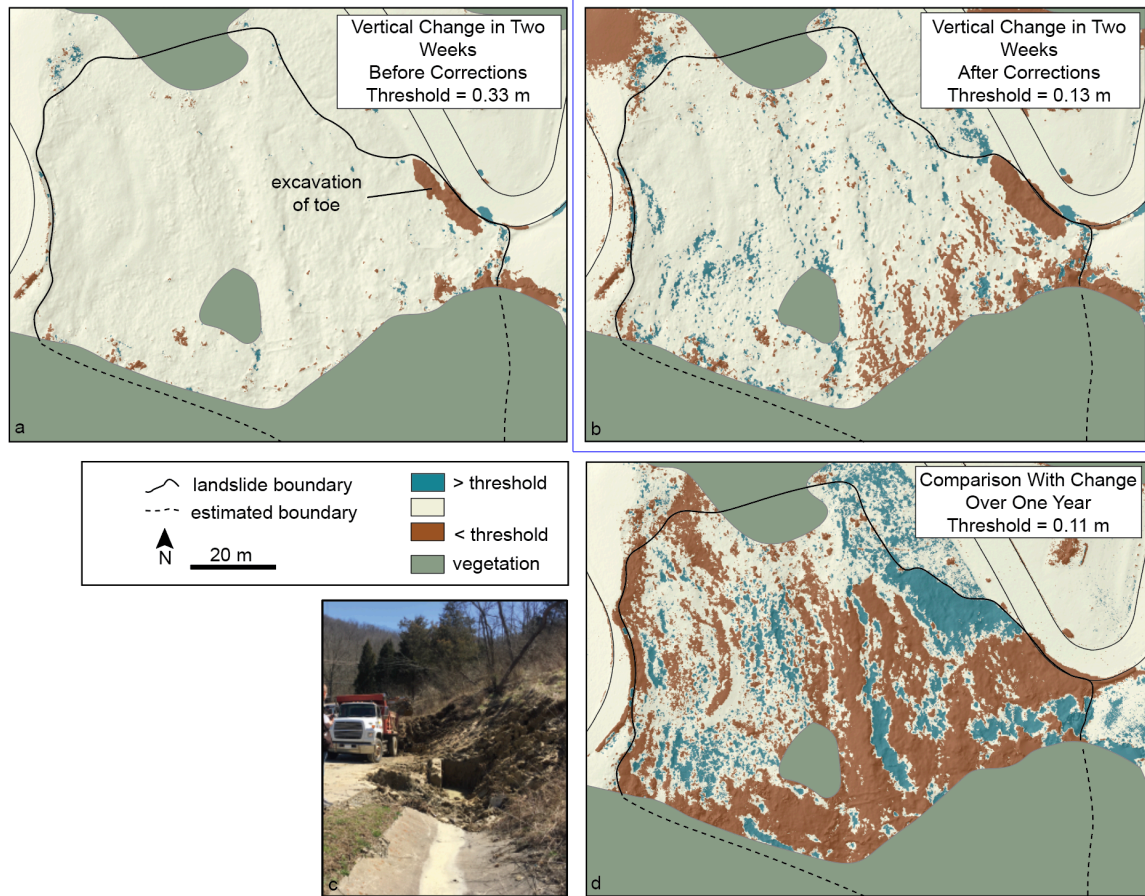


Figure 2.11. Example of threshold maps before and after corrections for DEMs flown two weeks apart in March, 2019. The toe of the landslide was being excavated during the second flight. (a) Threshold map prior to correction, using Method II, where the threshold of detectable change is 0.33 m. Only the change due to the excavation of the toe is apparent. (b) Threshold map after survey corrections, with a threshold of detectable change of 0.13 m. Small elevation changes in the body of the landslide are apparent. (c) Landslide toe being excavated during second flight. (d) Threshold map of elevation change over the course of the next year. Areas of small positive and negative changes correlate with the changes measured over two weeks.

### 2.5.2 Landslide deformation

The series of difference maps between 2007 and 2021 show that the Taylor Mill debris slide developed on a slope that had been altered by road construction, regrading, and the addition of fill. There is some evidence that a slow-moving landslide may have already existed at this location, but the most significant landslide movement occurred by 2012, likely due to record precipitation in 2011. Since 2012 the lower half of the landslide has continued to slowly deform and move out into the roadway, where it is periodically excavated, while the scarp region displays only minor elevation changes. The most significant change since 2012 is the major lateral expansion of the landslide onto the natural slope which had not been previously altered or shown any signs of

movement. This demonstrates that a landslide that arguably was staged by human activities and triggered by record rainfall can lead to the destabilization of adjacent undisturbed slopes. This is important for the Cincinnati and northern Kentucky region because there are numerous other slow-moving landslides in the area which are similarly sensitive to changes in precipitation (Sparling 2019). Regional precipitation has increased 5 to 10% over the past 50 years due to climate change (EPA 2016), and an increase in landslide activity is expected (Coe *et al.* 2018; Leschinsky *et al.* 2017; Mirus *et al.* 2017). Furthermore, these landslides can potentially expand laterally onto previously undisturbed slopes, as seen at in this study, causing additional damage to property and infrastructure.

Imagery accessed via Google Earth prior to the first lidar survey of 2007 indicates that a landslide may have already existed on the slope, as imagery from 2003 and 2005 shows some bare patches in the otherwise vegetated slope, and the vegetation was cleared and slope regraded by June of 2006 (Fig. 2.3). The county-wide lidar DEM and imagery from 2007 shows this regraded slope, and there is no evidence of the landslide at that time. Between May 2007 and October 2008 fill was added to the upper slope, and between October 2008 and July 2010, the upper curve of the driveway was reconstructed, and fill again added to the upper slope (Fig. 2.3).

The major elevation changes within the landslide between 2007 and 2012 (Figs. 2.8a, 2.9a) were likely triggered by the record rainfall of 2011 (Fig. 2.10b). The magnitude of elevation loss in the scarp area (up to 2.2 m) is much larger than the magnitude of positive elevation gain in the lower half of the slope (up to 1.3 m), as can be seen in the elevation profiles and the magnitude of vertical change (Figs. 2.9a and 2.10). The topographic profiles, mapped elevation changes, and magnitude of vertical change between 2007 and 2012 all indicate that more material was lost at the scarp than gained at the toe. Because the landslide toe extended into the road, this material was excavated and moved off-site.

Between 2012 and 2019 elevation changes continued to occur throughout the landslide, but the changes had a smaller magnitude (maximum of 1.2 m elevation change) than those that had occurred between 2007 and 2012 (Fig. 2.8b, 2.9b). Parallel bands of elevation gain and loss that roughly parallel contours indicate either internal deformation of the slide material as it moves over an irregular slip surface, or small internal slumps. Between 2019 and 2021 elevation changes have been greatest in the lower half of the slide, which has continued to advance into the driveway, and where debris has been periodically excavated (Figs. 2.8c, 2.8d, 2.9c, 2.9d). Elevation changes in the upper half of the slide appear to be confined to small slides or erosion. Between 2020 and 2021, the upper half of the slide appears quiescent (Figs. 2.8d, 2.9d).

By 2019 the landslide had also expanded laterally to the south. Though the full extent of this expansion was obscured by vegetation in the SfM surveys in 2019 and 2020, the lidar DEM in 2021 revealed that the landslide had laterally expanded by at least 60 m thereby more than doubling its width (Fig. 2.8e). The landslide is possibly expanding to the north as well. Some of this expansion appears to involve the fill placed on the slope before the 2012 lidar survey but has extended significantly beyond that. The

2021 lidar DEM (Fig. 2.8e) also shows that several gullies had developed on the slope which were not observed in the 2012 lidar, indicating the contribution of surface water to the landslide. Thus, the mobilization of the landslide by 2012 was followed by continued deformation of the toe, and a significant lateral expansion into a formerly undisturbed natural slope.

### 2.5.3 Landslide signature

This pattern of elevation change seen in the Taylor Mills landslide is characteristic of a debris slide, which ideally has an even loss of elevation in the scarp area, internal deformation in the body of the slide, and elevation gain in the toe (Fig. 2.12). Interbedded shale and limestone produce an uneven slip surface, which helps generate internal deformation of the debris slide material (Fleming and Johnson 1994). A slump, in contrast, would have the greatest elevation drop at the scarp, which would progressively diminish to the axis of rotation of the slide where the change should be zero, and then a gradual increase in elevation towards the toe (Fig. 2.12). Thus, we observe that the mapped elevation change signature reveals the nature of the slide.

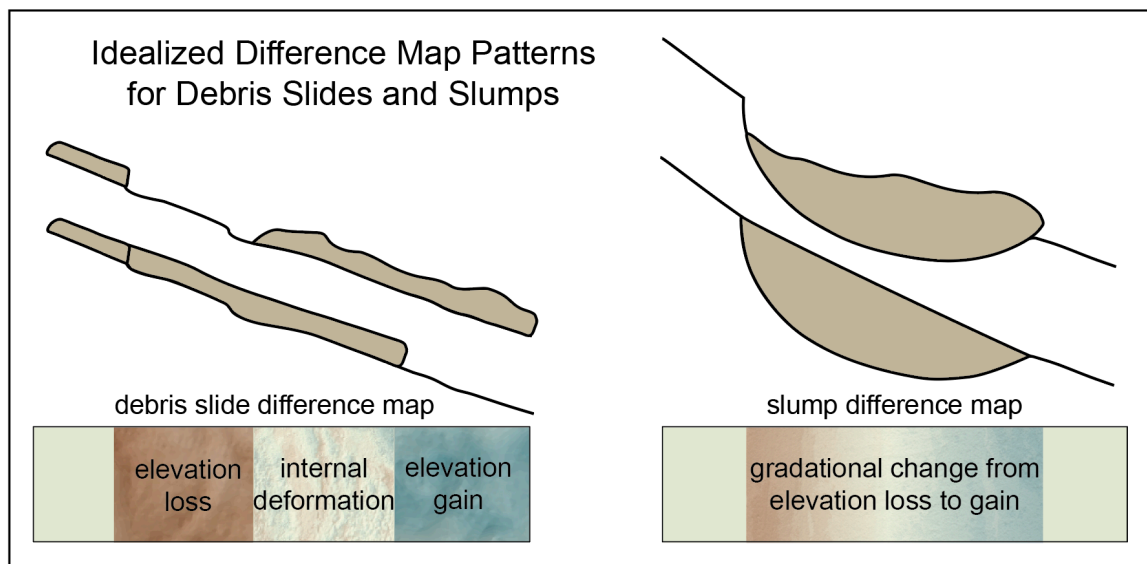


Figure 2.12. The pattern of elevation loss and gain expected for translational debris slides and rotational slumps. Interbedded shale and limestone produce an uneven slip surface, which helps generate internal deformation of the debris slide material (Fleming and Johnson 1994).

Because the landslide toe where it has run out over the road has been excavated periodically, we do not observe as much elevation gain in the toe as might be expected for a pristine debris slide. Typical debris-slide thickness are up to 2m for landslide in the region (Fleming and Johnson 1994; Baum and Johnson 1996), and the slightly higher elevation loss values observed in the scarp may be due to the regrading of the slope in 2006, and the additional fill material that was added to this slope between 2007 and 2010.



While differencing two DEMs produces a map of vertical change, this does not necessarily imply that the ground only deformed vertically. Elevation change in a landslide could be produced by vertical change but also by horizontal movement, or a combination of the two. In a translational debris slide, for example, there could be significant horizontal movement of the slide down the slope, while the vertical changes may not appear significant (Fig. 2.12). Ongoing work on landslides in the Cincinnati and northern Kentucky region will address the horizontal component of movement, in addition to the vertical changes reported here.

#### 2.5.4 Thermal Expansion and Contraction

The amount of expansion and contraction for diurnal or seasonal temperature changes will depend on the soil characteristics, moisture conditions, and the temperature conditions. A recent study on a loess slope in China found that the soil expanded and contracted with an amplitude of about 1 mm over the course of a year due to temperature variations (Lan *et al.* 2021). In a lab study of bentonite clay under thermal loading, the heating and cooling resulted in expansion and contraction with a volumetric strain of approximately 1.0% (Tang *et al.* 2008). If we consider a hypothetical 2-meter-thick volume of bentonite which is only allowed to expand vertically as a result of thermal loading, an elevation change of approximately 0.02 m would result. The clayey soils in the northern Kentucky area likely fall somewhere between these two examples, thus expansion and contraction values, while non-zero, would lie below the threshold values calculated for this study, the smallest of which is 0.05 m.

#### 2.5.5 Influence of Vegetation

The influence of vegetation on SfM DEMs is well-documented (Cook 2017; Zekkos *et al.* 2018) and is significant when comparing elevation maps over longer time spans when changes to vegetation can be expected. However, we found that in SfM DEMs conducted close in time and prior to the growing season, very little change to vegetation has occurred. Therefore, any vertical change to the landslide will change the vegetation as well, and vertical changes in the vegetation reflect real vertical change in the landslide. The combination of DEMs over a two-week period was able to detect small elevation changes in the body of the slide, and the locations and magnitudes of these changes were confirmed in the survey of the following year (Fig. 2.11).

It is sometimes assumed that vegetation is completely removed in bare earth DEMs derived from lidar, when in fact vegetation may still influence the DEM. For example, elevation changes between two lidar DEMs are seen in the mowed area across the road from the landslide, which reflects the differing grass heights during these two surveys (Fig. 2.6b).

### 2.5.6 Spatial variability of uncertainty

There is spatial variability in uncertainty related to terrain characteristics such as roughness (Podobnikar 2016), slope (Xiong *et al.* 2018), point density and vegetation (Clapuyt *et al.* 2016), and combinations of terrain characteristics (Carlisle 2005). In this study we used errors in the apparently stable and smooth roadways outside of the landslide. If no road or other smooth surface was available, we expect that thresholds of detectable change would be higher. For example, for the combination of the 2012 county-wide lidar DEM and the SfM DEM of March 11, 2019, the road areas had a distribution of noise of  $0.034 \pm 0.033$  m, and threshold values of 0.06 m (Method I), and 0.09 m (Method II). In contrast, the distribution of noise in the grassy area below the landslide was  $-0.074 \pm 0.072$  m, which produced threshold values of  $\pm 0.14$  m (Method I), and  $\pm 0.20$  m (Method II).

## 2.6 CONCLUSIONS

Slow-moving landslides are chronically destructive and can permanently damage property and infrastructure. The purpose of this study was to better understand decadal-scale spatial and temporal variations in a slow-moving debris slide in northern Kentucky over 14 years. To accomplish this, we needed to integrate existing county-wide lidar data acquired before our study began, along with site-specific SfM and UAV-lidar surveys. Because the technology and quality differ among surveys, the challenge was to devise a method to quantify survey noise so that a threshold of detectable change could be calculated. To reduce the threshold of detectable change, bias between lidar DEMs and tilt between SfM DEMs was first corrected to produce a zero mean elevation difference in areas outside of the landslide where no change is inferred to have occurred. The threshold of detectable change was then calculated from the remaining random noise using two methods, each of which use the propagated elevation difference errors for the DEM combination. Method I used the errors from the difference map, and Method II used back-calculated estimates of the individual DEM errors. The thresholds of detectable change range from  $\pm 0.05$  to  $\pm 0.20$  m, depending on the DEM combination and method used, with Method II producing a larger threshold value.

The series of difference maps between 2007 and 2021 show the landslide developed on a slope that had been altered by road construction, regrading, and the addition of fill. The greatest change in the landslide occurred between 2007 and 2012 and was likely triggered by the record rainfall of 2011. Since 2012 the lower half of the slide has continued to slowly deform while the upper half of the slide has been generally quiescent. The most significant change since 2012 is that the landslide has expanded laterally by at least 60 m into a previously unaltered slope which had previously shown no signs of movement, demonstrating that a landslide that was staged by human activity can lead to the destabilization of adjacent slopes.

The region has numerous other slow-moving landslides, and with precipitation increasing due to climate change, landslide activity is only projected to increase. Thus, monitoring these slow-moving landslides is a critical part of landslide mitigation. We found real change occurred in the landslide in all DEM combinations, including in SfM

DEMs separated in time by just two weeks. Thus, in addition to providing a way to utilize older or noisy low-resolution datasets to document the behavior of a landslide over many years to decades, the methods of calculating a threshold of detectable change presented here can also provide a reliable method of monitoring ongoing changes in a slow-moving landslide. This technique for calculating a threshold of detectable change is widely applicable to other change detection studies where various survey technologies have been used to capture elevation data, including older regional or low-resolution surveys that might predate a particular investigation.

## 2.7 ACKNOWLEDGMENTS

We thank Jason Dortch, Ryan Thigpen, Yichuan Zhu, Roger Olsen, and Rachel Noble-Varney for their contributions to the preparation of this manuscript.

This work is published as:

Johnson, S.E., Haneberg, W. C, Crawford, M., Bryson, S., 2023, Measuring ground surface elevation changes in a slow-moving colluvial landslide using combinations of regional airborne lidar, UAV lidar, and UAV photogrammetric surveys. *Quarterly Journal of Engineering Geology and Hydrogeology*. <https://doi.org/10.1144/qjegh2022-078>.

## CHAPTER 3. MACHINE LEARNING FOR SURFICIAL GEOLOGIC MAPPING

### 3.1 ABSTRACT

Geologic maps provide a valuable contribution to society and industry. However, geologic maps may convey a level of certainty that obscures the fact that we are unable to directly observe geologic variables at every point, and thus there is uncertainty inherent to any geologic map. In this study we examine the combination of machine learning and digital terrain data to provide a new method for producing surficial geologic maps which can also convey and preserve the underlying uncertainty. We measured the performance of eight supervised machine learning methods using data from two quadrangles in Kentucky by comparing the overall model accuracy and the F1 scores for each geologic unit, which includes residuum, colluvium, alluvial and lacustrine terraces, high level alluvial deposits, and modern alluvium. The importance of 31 geomorphic variables derived from lidar data including slope, roughness, residual topography, curvature, normalized topographic position, and the standard deviation of elevation, was reduced to 11 variables by perturbing each variable in turn and measuring the resulting loss of accuracy. The Gradient Boosted Trees model produced the classifier with the greatest overall accuracy, producing maps with overall accuracies of 86.5% to 93.1% in areas of simple geology, and 78.3% to 79.5% in areas with more complex geology. The model produced high F1 scores for colluvium (up to 96.3%), but was not as good at distinguishing between units found in the same geomorphic position, such as high level alluvium and residuum, both of which are found on ridgelines. Uncertainty values are conveyed in the map using gradations of color while eliminating the need for drawn boundaries between units. We conclude that machine learning may be used to create accurate surficial geologic maps in areas of simple geology; in more complex areas, additional information obtained in the field is necessary, but ML classification provides a base map highlighting where areas of geologic uncertainty lie.

### 3.2 INTRODUCTION

The making of geologic maps is a fundamental contribution of geologists to society and industry. However, formatting limitations require geologists and cartographers to make decisions about what information to display and omit, as well as how to show boundaries and areas of geologic uncertainty or transition. Traditionally, there have been few options to communicate the nuance and uncertainty in the mapping process. Perhaps not fully understood by many map users is that geologic maps may convey a level of certainty which obscures the myriad of decisions and interpretations made by the mapper. The combination of machine learning with surface, geophysical, and remote sensing data provides a new tool for producing geologic maps which can also convey the underlying uncertainty intrinsic to any geologic map.

The utility of geologic maps in locating natural resources and for engineering projects has been recognized since the first widely published geologic map of England by William Smith (Smith 1815; Winchester 2009). In addition to geologic information in

support of mineral, energy and water resource exploration, geologic maps contribute to decision making processes in other areas including natural hazards such as landslides, rockfall, flood, earthquakes, and karst; land-use planning, climate change, environmental impact evaluations, identifying health hazards, and in locating, and building infrastructure such as roads, buildings, dams, and utilities (Bernknopf et al. 1993; GSA 2022; Derouin 2021). The economic value of geologic maps includes not only resource development, but the prevention of economic loss due to poor land-use decisions, and documented benefit-to-cost ratio for geologic mapping ranges from 4:1 to >100:1 (Berg, MacCormack, and Russell 2019).

A map of geologic units and boundaries may convey a certainty to the user that the map gives exact and perfect information about the geology at every map location. In reality, mapped geological boundaries are inherently uncertain for several reasons: the boundary may be gradational as opposed to a sharp contact, the width and position of boundaries are generalized and dependent on the scale of the map, and boundaries may be obscured in the field (Lark et al. 2015). As we are unable to directly observe geologic variables at every point, we use models— either mental or computational—to fill in the gaps (Kirkwood 2022). Individual mappers might use different models and thus produce different maps of the same location. In addition, decisions mappers used to define boundaries might be poorly documented, and the depth of information that went into the creation of a map may not be conveyed in the final product (Kirkwood 2022). As there are many potential models to interpolate between direct observations, uncertainty is integral to geologic maps.

Technological advances throughout history have facilitated changes in geologic mapping: GPS, GIS, aerial photography, satellite imagery, lidar, geophysical and geochemical datasets. Over the past decade, the expanded deployment of traditional sensors and the development of new data sources such as lidar and satellite data have increased the amount of data available to geoscientists (Bergen et al. 2019). The availability of these large datasets, in combination with advances in computational capacity, have made machine learning increasingly applicable to modeling a variety of Earth processes. Advantages of ML specific to geologic mapping are the ability to process datasets with numerous variables (high-dimensionality datasets) in order to replicate human mapping performance, to produce maps more quickly than humans can, to produce maps using a consistent well-documented model across large regions, to provide uncertainty estimates resulting from the model, and to convey that uncertainty as part of the final map (Bergen et al. 2019; Cracknell and Reading 2013). There are two main types of machine learning (ML); supervised classification requires labeled examples to learn to distinguish patterns and then make predictions or classify previously unseen data, while unsupervised classification techniques learn to distinguish patterns in data without any labels provided. A ML map can document the probability for each class at any point on the map and provide a consistent and well-documented mapping process. Thus the map user can obtain information about the range of geological properties they might encounter at any particular location (Kirkwood 2022).

While there are examples of geologic maps of bedrock produced using ML methods, there is also great potential for ML in mapping surficial geology. Maps of

bedrock geology in New South Wales, Australia were produced from dispersed geologic data in conjunction with geophysical and remote sensing data (Cracknell and Reading 2014), and in the Eastern Goldfields of Australia using only geophysical data (Kuhn, Cracknell, and Reading 2018). Geochemical maps in England were generated using sparse geochemical data in combination with geophysical and remote sensing data (Kirkwood et al. 2016; 2022). However, fewer maps have been created of surficial geology using ML, such as regolith mapping in West Africa using airborne geophysics and remote sensing data (Metelka et al. 2018), though there are examples of surficial geologic hazards identified utilizing ML such as landslide-susceptibility maps produced using landslide inventories and lidar data in Kentucky (Crawford et al. 2021) and Japan (Dou et al. 2019), and the identification of sinkholes in Kentucky (Zhu and Pierskalla 2016). Given the dramatic increase in the number of geophysical and other datasets publicly available, there is great potential for the expansion of ML to geologic mapping applications throughout the world which may be particularly useful where ground information is sparse or non-existent.

In this study we examine the utility of machine learning to the process of mapping the surficial geology of Kentucky using the characteristics of the terrain derived solely from lidar-based digital elevation models (DEMs). Our goal was to automate the process of mapping surficial geologic units and produce maps where classification uncertainty is conveyed. The Commonwealth of Kentucky, USA is the first state with bedrock fully mapped at a scale of 1:24,000. The cost of mapping bedrock for all 707 quadrangles was initially justified by the economic development of coal, oil, natural gas, and minerals; today the use of maps for management of land, water and the environment has supplanted their use for natural resource development (Bhagwat and Ipe 2000). To address these needs, geologic mapping of surficial deposits began in 2004 and continues today (KGS 2021). Mapping the surficial geology of each quadrangle using traditional means requires multiple steps: contacts between surficial units are mapped based on topographic features derived from lidar data, these initial maps are used in the field to view unclear features, contacts and units, and observe and collect soils and other samples to inform and update the maps, and final maps are produced, with the process taking approximately one year (Hammond et al. 2017). To test the utility of ML to create surficial geologic maps, we first test eight different ML models and 31 terrain variables to determine the best performing model and the key variables needed to produce maps efficiently. The Gradient Boosted Trees model generated the highest overall accuracy (up to 92%), and with few exceptions the highest F1 scores for each individual map unit, and provided robust estimates of uncertainty which can be conveyed in the resulting geologic maps. We conclude that maps generated from this model could be used either as an initial step to identify areas of geologic uncertainty where additional field observations or sampling are needed, or, in areas where the geologic units are relatively simple and uncertainty values are low, could produce near-final maps. This method has the potential to be used not only throughout the state, which has lidar data available for its entirety, but other regions where lidar data is available.

### 3.3 GEOLOGIC SETTING

The two quadrangles used for this study are both situated within the Outer Bluegrass physiographic region of Kentucky, which is characterized by a dissected terrain that has formed in gently dipping Paleozoic carbonates and shales (McDowell 1986). A dendritic drainage system contributes to the larger river valleys, which are entrenched 60-90 m below the ridges and hold a sequence of lacustrine and alluvial terraces above the modern floodplain. The De Mossville Quadrangle (Massey 2017) is in Pendleton County, KY, about 21 miles south of Cincinnati, OH, and the Ohio River (Fig. 3.1). The Pitts Point Quadrangle (Massey et al. 2019) is in Bullitt County, approximately 100 miles to the southeast of the De Mossville quadrangle, and 30 miles south of Louisville, KY. The Licking River meanders north towards the Ohio River through the De Mossville quadrangle and the Salt River flows to the Ohio River 9 miles to the north through the Pitts Point quadrangle.

Bedrock has weathered to produce ridgetops of residuum, and moderate to steep slopes of colluvium. In both quadrangles, the residuum of the ridgetops is interrupted by high-level alluvial and lacustrine deposits or terraces that date to the Pliocene or early Pleistocene (KGS 2023; Massey et al. 2019; Massey 2017). These deposits record the presence of an ancestral river system which predates the downcutting of the Ohio River to its current level. (Potter 2007; McDowell 1986). As the Laurentide ice sheet advanced and blocked this ancestral river system, the Ohio River valley was formed (Durrell 1982; Granger and Smith 1998). The former plateau was dissected in a dendritic pattern as the landscape eroded to meet this new base level. Subsequent glacial advances and their deposits blocked drainages, forming lakes, their presence recorded by extensive lacustrine terraces (middle to late Pleistocene) found along the river valleys, including both quadrangles in this study. These lacustrine terraces have been dissected by late-Pleistocene alluvial terraces into which the modern floodplain is entrenched.

Surficial geologic units in both quadrangles form both natural resources as well as hazards. Outwash and alluvial terraces form resources of sand and gravel for building materials and freshwater aquifers. (McDowell 1986; Potter 2007). The steep slopes of colluvium developed from shale-rich bedrock form numerous damaging landslides (Baum and Johnson 1996; Crawford 2012; Johnson et al. 2023).



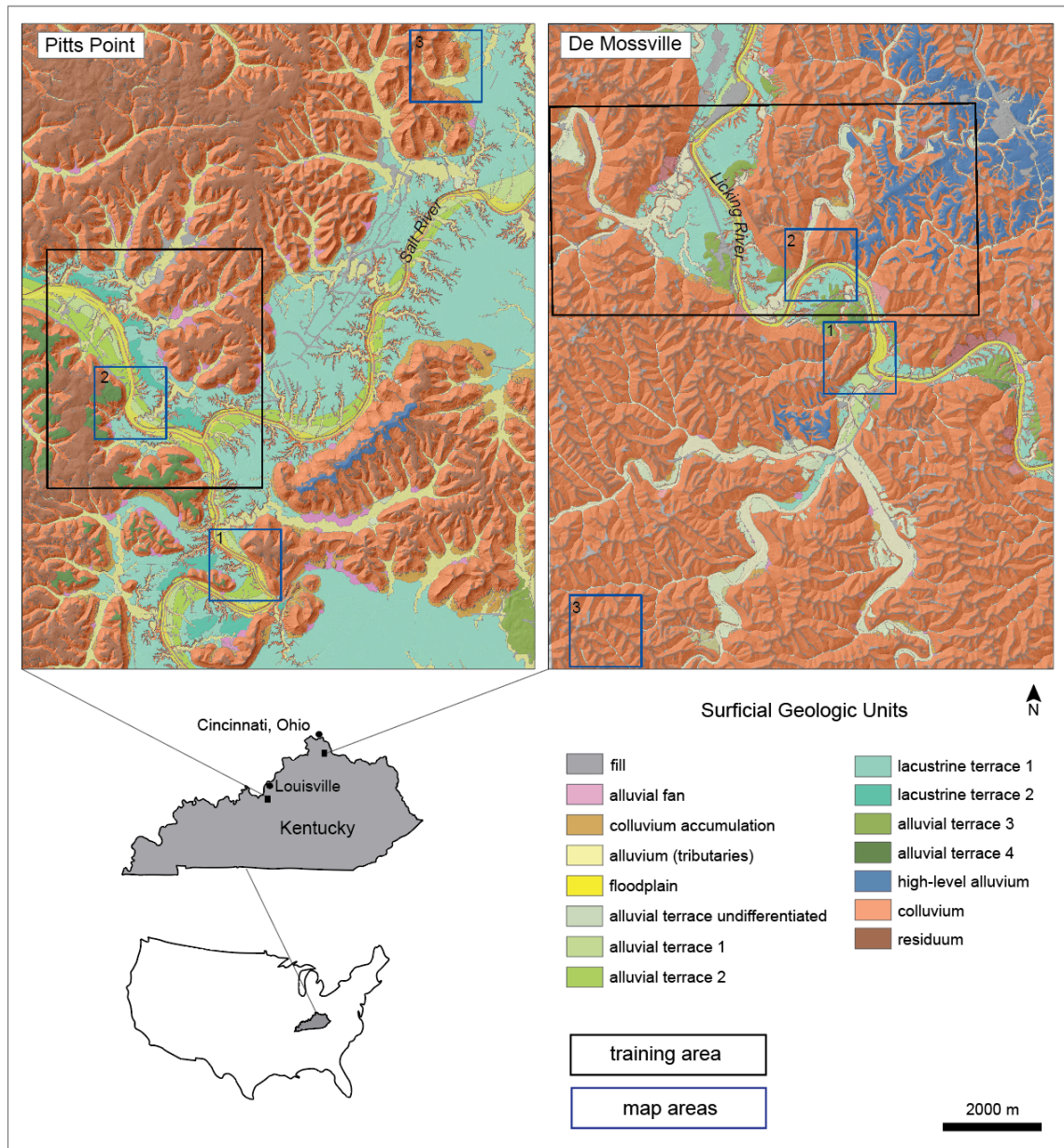


Figure 3.1. Location and surficial geology of the 7.5-minute Pitts Point and De Mossville quadrangles in Kentucky, USA.

### 3.4 METHODS

#### 3.4.1 Overview

The utility of machine learning (ML) for mapping surficial geology in Kentucky was assessed by training and testing eight ML methods using publicly available digital elevation models (DEMs) and surficial geologic maps for two quadrangles in Kentucky.

A summary workflow is shown in Fig. 3.2, and each step is described in detail in the following paragraphs.

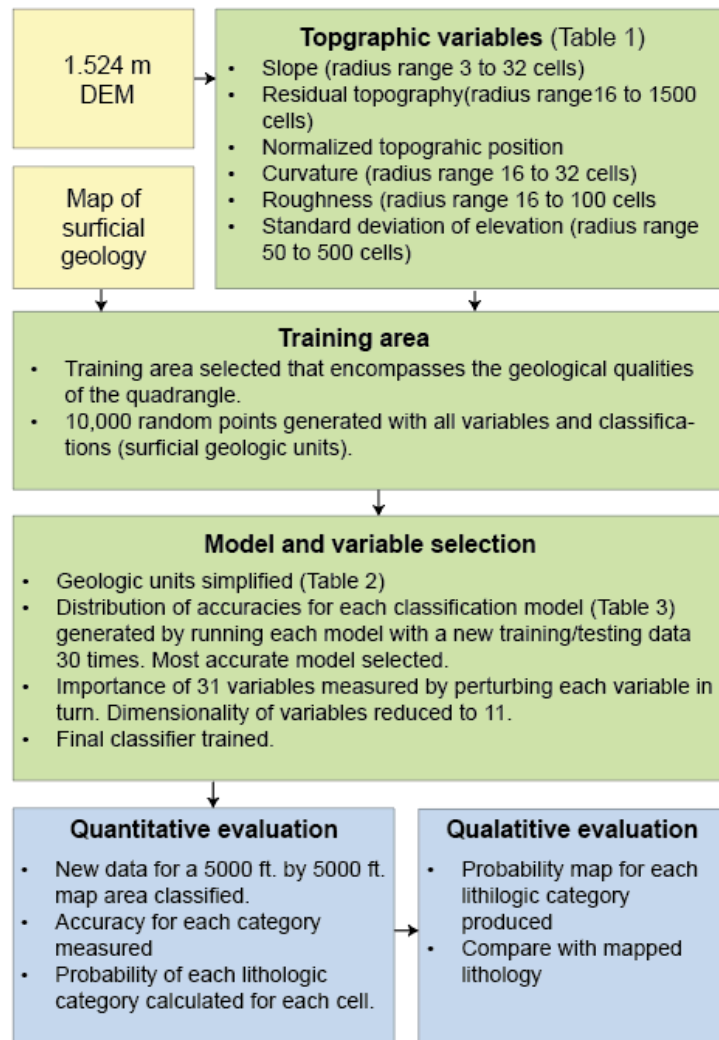


Figure 3.2. Overview of workflow

### 3.4.2 Surficial geologic quadrangles

Machine learning methods were applied to two surficial geologic maps published as 7.5-minute quadrangles by the Kentucky Geological Survey (KGS). These were created using traditional field-based and digital mapping methods. One quadrangle from each region, Pitts Point (SE corner 85° 45', 37° 52' 30") and De Mossville (SE corner 84° 22' 30", 38° 45') were each chosen to include a diverse set of surficial geologic units including residuum and colluvium derived from bedrock units, high-level pre-glacial alluvial deposits, a sequence of alluvial and lacustrine terraces, modern alluvial deposits, and fill.

### 3.4.3 Digital elevation maps and derivative maps

The DEMs for the Pitts Point and De Mossville Quadrangles are publicly available through KyFromAbove, the state's elevation data and aerial photography program, which is accessible digitally at [kyfromabove.ky.gov](http://kyfromabove.ky.gov). The maps were derived from lidar data and have a 5 ft. (1.524 m) cell size. To test which geomorphic variables are the most important for the ML models, a series of 31 derivative maps were made from the DEMs using GIS software (Table 3.1). The derivative maps represent geomorphic attributes independent of their specific location (i.e. latitude, longitude and elevation). They measure qualities of the geomorphology ranging from local scale (1.5 to 12.2 m) to landscape scale (760 m to 2740 m). Thus, each cell has information about its local vicinity as well as a comparison to or measure of the surrounding terrain.

A series of smoothed DEMs were produced using a focal statistics tool in GIS, which calculates a statistic for a defined region around a particular cell, in this case the mean elevation within a circular radius around each cell ranging from 16 cells to 1500 cells (49 m to 2740 m). Slope maps were made from the original unsmoothed DEM and smoothed DEMs. Residual topographic maps were produced by subtracting each smoothed DEM from the elevation for each cell, thus allowing the position of a cell relative to its surroundings to be represented, with positive values representing ridges or peaks, negative values representing depressions or valleys, and values close to zero representing an even slope or flat area (Weiss 2001; De Reu et al. 2013; Haneberg et al. 2005). A normalized topographic position map was produced by dividing the difference between the elevation of each cell and the minimum elevation of the quadrangle, by the range of elevation for the quadrangle. Curvature represents the slope of the slope and was calculated using GIS for a radius ranging between 16 to 32 cells. Positive curvature values indicate an upwardly convex surface, and a negative value indicate an upwardly concave surface. Roughness maps were produced using the focal statistics tool to calculate the standard deviation of the slope angles derived from the original DEM within a circular radius ranging from 16 to 150 cells (Grohmann, Smith, and Riccomini 2011). The standard deviation of elevations from the unsmoothed original DEM was produced using the focal statistics tool, using a radius ranging from 100 to 500 cells (Grohmann, Smith, and Riccomini 2011).

Table 3.1 Definition of variables.

Variable	Description
Elevation	Mean height of cell measured from mean sea level.
Smoothed DEM	Mean elevation within a radius ranging from 16 to 1500 cells. Not used directly, but used to calculate the residual topography and produce slope maps.
Slope	Slope original DEM, using a 3 by 3 cell moving window.
Slope radius 16, 24, 32	Slope of the smoothed DEM.
Residual Topography (RT), radius 16, 24, 32, 50, 100, 150, 200, 500, 1000, 1500	The elevation of the original DEM minus the smoothed DEM.
Normalized Topographic Position (NTP)	Elevation values normalized using the maximum and minimum elevation values in the quadrangle.
Curvature radius 16, 24, 32	The second derivative of the surface, or the slope of the slope.
Roughness radius 16, 24, 32, 50, 100, 150	Standard deviation of the slope angles derived from the original DEM within a radius of 16, 24, 32, 50, 100, and 150 cells.
DEM Standard Deviation, radius 100, 150, 200, 250, 500	Standard deviation of the elevation values from the original DEM, within a circle of radius 100, 150, 200, 250, and 500 cells.

#### 3.4.4 Geologic classes

The geologic units were simplified to avoid under-sampling smaller-scale features such as alluvial fans, colluvium accumulation zones, landslides, small-scale remnants of lacustrine and alluvial terraces, and different varieties of fill (Table 3.2). Colluvium is defined to include landslides and colluvium accumulation zones found at the base of some slopes. Alluvium is defined to include alluvial fans, alluvium in tributaries, old alluvium, and undifferentiated alluvial terraces. The lacustrine and alluvial terraces in the Pitts Point quadrangle are extensive and well-preserved (Fig. 3.1) and were divided into three terrace units: alluvial terraces 3 & 4 are at the highest level; lacustrine terraces 1 & 2 lie below this; and alluvial terraces 1 & 2 are at a lower level nearest the modern floodplain. Some of these same terraces are found in the De Mossville quadrangle, but are not as well-preserved or extensive, thus all terraces in this instance were grouped together as one terrace unit. Modern floodplain deposits were mapped as a separate unit in the Pitts Point quadrangle but were included with the other alluvial deposits in the De Mossville quadrangle. Fill includes engineered and other artificial fill.

Table 3.2. Simplified lithological categories.

<b>Pitts Point</b>	<b>De Mossville</b>
Residuum	Residuum
Colluvium (includes landslides and colluvial accumulation at the base of slopes)	Colluvium (includes landslides and colluvial accumulation at base of slopes)
High-level alluvium (high-elevation pre-glacial river system deposits)	High-level alluvium (high-elevation pre-glacial river system deposits)
Alluvial Terrace 3 & 4	
Lacustrine Terraces 1 & 2	Terraces (lacustrine terrace 1 and alluvial terraces 1, 3, and 4)
Alluvial Terraces 1 & 2	
Floodplain (main river valley)	Alluvium (includes alluvial fans, floodplain, alluvium in tributaries, old alluvium, undifferentiated alluvial terraces)
Alluvium (includes alluvial fans, alluvium in tributaries, old alluvium, undifferentiated alluvial terraces)	
Artificial fill (engineered and other fill)	Artificial fill (engineered and other fill)

### 3.4.5 Machine Learning Methods

Supervised machine learning methods use training data that has a known classification, in this case the mapped geologic unit, to train a classifier which is then used to classify previously unobserved data. To build the classifier and measure how well it performs, the data set is randomly divided into a training set, which is used to train the model, and a testing set which is used to measure the performance of the model. Each time the model is run, the data may be divided into different training and testing sets, and thus the resulting model performance will be slightly different.

We measured the performance of eight supervised machine learning methods in Mathematica using a dataset of 10,000 random points within a training area for each quadrangle (Fig. 3.1), with 75% of the points used to train the model, and the remaining 25% used to test the model. The eight machine learning methods tested represent the main types of supervised learning algorithms and are available in the software used for the analysis (Bergen et al. 2019; “Mathematica” 2022): Logistic Regression (Cox 1958), Nearest Neighbor, Support Vector Machine (Vapnik 1998), Decision Tree, Naïve Bayes, Neural Network, Random Forest (Breiman 2001), and Gradient Boosted Trees (Table 3.3). Because the performance of the model varies depending on the randomly selected training and testing set values, each model was run 30 times to build a distribution of accuracies for each model. The model that produced the greatest overall accuracy and F1 scores was then used for further analysis. For comparison, the model that produced the lowest overall accuracy and F1 scores was also used for further analysis.

Table 3.3. Description of different ML models.

<b>Machine Learning Method</b>	<b>Algorithm Type</b>	<b>Description</b>
Logistic Regression	Binary classifier	Uses a logistic function to estimate the probability that a data point belongs to one of two classes.
Support Vector Machine	Binary classifier	Finds a hyperplane that separates training data into two classes. A multiclass classification is reduced to a set of binary classification problems.
Nearest Neighbor	Instance-based	Infers the class of each example by comparing to the nearest neighbor in the feature space and picking the commonest class or average value.
Decision Tree	Decision Tree	A branching tree-like structure where each node represents a test on each feature, each branch represents the outcome of a test, each leaf represents a prediction or class probability.
Random Forest	Ensemble	An ensemble of weaker decision trees independently trained on a subset of the training data. Predictions are combined.
Gradient Boosted Trees	Ensemble	An ensemble of weaker decision trees is trained sequentially, compensating for the weaknesses of previous trees.
Naïve Bayes	Bayesian	Applies Bayes's theorem which assumes that features are independent given the class, regardless of possible correlations between features.
Neural Network	Neural Network	Consists of stacked layers each of which performs a single computation and passes that value to the next layer.

### 3.4.6 Variables & dimensionality reduction

A total of 31 variables were initially used to train the eight machine learning models. The dimensionality of the dataset was then reduced to the 11 most important variables to lessen the computing power necessary to perform further classifications of larger map areas. We evaluated variable importance by randomly permuting each variable in turn, and comparing the resulting accuracy compared with the unaltered values (Breiman 2001; Antonov 2016; Zhu and Pierskalla 2016; Crawford et al. 2021). Each of the 31 variables was tested by training a classifier with all variables, then permuting the values for one of the variables in the testing data and measuring the resulting accuracy produced by the trained classifier. The lower the resulting accuracy, the more important that particular variable is to the classifier. This process was repeated for each variable in turn. Again, as the results will vary depending on the training and testing sets, this was repeated 20 times using different randomly selected training/testing sets. The resulting range of accuracies, those generated by the perturbed variables, was then plotted versus a baseline accuracy generated by the unaltered variables. The 11 variables that had the greatest impact on the overall classifier accuracies were selected as the most important. A comparison of the distributions of classifier accuracy with all 31 variables versus a model trained with just the 11 selected variables was performed to measure the change to the accuracy by running each version of the model 20 times.

### 3.4.7 Quantifying model performance

The performance of eight machine learning methods was evaluated by comparing their overall accuracy and the F1 scores for each geologic unit. Accuracy is defined as the fraction of correctly classified examples:

$$Accuracy = \frac{TP + TN}{TP + TN + FP + FN}$$

Where TP = the number of true positive predictions, TN = the number of true negative predictions, FP = the number of false positive predictions (Type I errors), and FN = the number of false negative predictions (Type II errors). Accuracy is a useful metric for comparing the models which all use the same data. However, as the distribution of classes is not even (e.g., there are many more samples of colluvium than high-level alluvium or fill), accuracy is not a good way to measure model performance for each geologic unit (Forman and Scholz 2010). For example, a good performance of the model to predict colluvium might overshadow its poor performance in predicting fill. The F1 score, on the other hand, accounts for class imbalance through the metrics of Precision and Recall for each class:

$$Precision = \frac{TP}{TP + FP}$$

$$Recall = \frac{TP}{TP + FN}$$

$$F1 = 2 * \frac{Precision * Recall}{Precision + Recall}$$

### 3.4.8 Lithologic probability maps

Qualitative evaluations of the best and worst models were produced by creating maps for three 1.5 km x 1.5 km areas for each quadrangle. Map 1 for both the Pitts Point and De Mossville quadrangles is just outside of the training area. Map 2 is within the training area, and Map 3 is 4.5 to 6 km away from the training area boundary for the Pitts Point and De Mossville quadrangles, respectively (Fig. 3.1). The probability of every cell belonging to each geological unit was calculated using the ML model. These probabilities were then brought into GIS software, and probability map layers were produced for each unit. These maps were symbolized so that the darkest shade represents a probability of  $\geq 80\%$ , the middle tone represents probabilities of 60% to 80%, the lightest tone represents probabilities of 40% to 60%, and probabilities of  $< 40\%$  are completely transparent. In this way each map layer preserves the underlying uncertainty, and



different map users could change the symbology according to their purpose. Map layers are rendered as semi-transparent, so that the multiple lithologies may be viewed at one time, and areas where two or more lithologies are probable, each will be visible.

## 3.5 RESULTS

### 3.5.1 Model Accuracy and F1 scores

Of the eight models tested, the Gradient Boosted Trees (GBT) model produced the classifier with the greatest overall accuracy in the training area for both the Pitts Point and De Mossville Quadrangles, with an overall accuracy of  $0.921 \pm 0.006$  and  $0.904 \pm 0.008$ , respectively (Fig. 3.3, Tables 3.4 and 3.5), and the Naïve Bayes model produced the least accurate classifier in both cases, of  $0.792 \pm 0.008$  and  $0.819 \pm 0.008$ , respectively. The GBT model also produced the highest F1 scores for all geologic units for both quadrangles. In the Pitts Point quadrangle, the colluvium, residuum, alluvial terraces 1&2, lacustrine terraces 1&2, and floodplain have F1 scores of 90% or greater, while the fill, alluvium, and alluvial terrace 4 have lower F1 scores (Table 3.4). In the De Mossville quadrangle, the colluvium and terraces have F1 scores of 90% or greater, while the fill, alluvium, high-level alluvium, and residuum have lower F1 scores (Table 3.5).

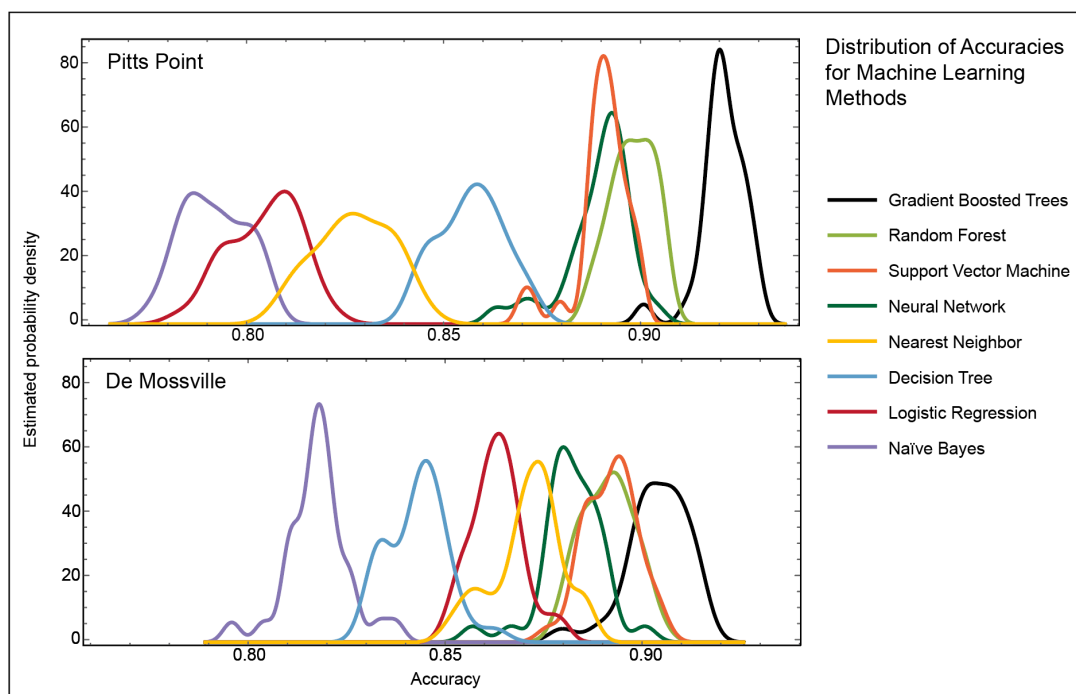


Figure 3.3. a) Distribution of accuracies for each model tested for the Pitts Point and De Mossville Quadrangles. In both cases, the Gradient Boosted Trees model produced the greatest accuracy, and the Naïve Bayes model produced the least accurate classifier.

Table 3.4. F1 scores for each lithologic class for the Pitts Point quadrangle, and the overall accuracy for each machine learning model.

Pitts Point Geologic Unit	# sampl es	Gradient Boosted Trees	Random Forest	Support Vector Machine	Neural Network	Nearest Neighbors	Decision Tree	Logistic Regression	Naïve Bayes
Fill	144	0.449 ± 0.067	0.084 ± 0.049	0.360 ± 0.120	0.411 ± 0.113	0.192 ± 0.073	0.215 ± 0.069	0.224 ± 0.058	0.179 ± 0.070
Flood- plain	526	0.905 ± 0.021	0.876 ± 0.021	0.823 ± 0.023	0.843 ± 0.024	0.744 ± 0.023	0.796 ± 0.026	0.675 ± 0.035	0.690 ± 0.025
Alluvium	1013	0.837 ± 0.018	0.814 ± 0.015	0.809 ± 0.015	0.808 ± 0.011	0.758 ± 0.020	0.728 ± 0.019	0.719 ± 0.019	0.632 ± 0.015
Alluvial terraces 1&2	893	0.916 ± 0.015	0.882 ± 0.013	0.836 ± 0.021	0.840 ± 0.029	0.655 ± 0.028	0.819 ± 0.022	0.547 ± 0.060	0.762 ± 0.015
Lacustrine terraces 1&2	1713	0.938 ± 0.008	0.924 ± 0.008	0.834 ± 0.011	0.910 ± 0.013	0.833 ± 0.012	0.894 ± 0.015	0.808 ± 0.017	0.878 ± 0.010
Alluvial terrace 4	539	0.881 ± 0.017	0.784 ± 0.031	0.794 ± 0.033	0.774 ± 0.062	0.555 ± 0.055	0.749 ± 0.031	0.551 ± 0.043	0.579 ± 0.044
Colluvium	3696	0.948 ± 0.005	0.941 ± 0.004	0.942 ± 0.005	0.941 ± 0.005	0.929 ± 0.006	0.915 ± 0.006	0.917 ± 0.006	0.882 ± 0.007
Residuum	1576	0.943 ± 0.007	0.915 ± 0.010	0.813 ± 0.018	0.910 ± 0.014	0.862 ± 0.014	0.892 ± 0.012	0.852 ± 0.011	0.843 ± 0.015
Overall Accuracy	10000	0.921 ± 0.006	0.898 ± 0.005	0.890 ± 0.007	0.889 ± 0.009	0.831 ± 0.009	0.857 ± 0.008	0.804 ± 0.009	0.792 ± 0.008

Table 3.5. F1 scores for each lithologic class for the De Mossville quadrangle, and the overall accuracy for each machine learning model.

De Mossville Geologic Unit	# sampl es	Gradient Boosted Trees	Random Forest	Support Vector Machine	Neural Networ k	Nearest Neighbors	Decision Tree	Logistic Regression	Naïve Bayes
Fill	349	0.311 ± 0.064	0.095 ± 0.052	0.231 ± 0.060	0.227 ± 0.065	0.017 ± 0.025	0.237 ± 0.052	0.123 ± 0.033	0.139 ± 0.027
Alluvium	1054	0.883 ± 0.011	0.869 ± 0.019	0.866 ± 0.015	0.851 ± 0.020	0.821 ± 0.022	0.797 ± 0.017	0.841 ± 0.016	0.736 ± 0.018
Alluvial & lacustrine terraces	1518	0.907 ± 0.012	0.892 ± 0.012	0.889 ± 0.010	0.873 ± 0.015	0.857 ± 0.014	0.851 ± 0.014	0.867 ± 0.012	0.828 ± 0.013
High-level alluvium	738	0.875 ± 0.023	0.842 ± 0.023	0.839 ± 0.019	0.828 ± 0.023	0.801 ± 0.021	0.777 ± 0.037	0.751 ± 0.025	0.770 ± 0.019
Colluvium	5678	0.942 ± 0.005	0.937 ± 0.006	0.938 ± 0.005	0.934 ± 0.004	0.932 ± 0.005	0.910 ± 0.005	0.920 ± 0.004	0.900 ± 0.007
Residuum	663	0.848 ± 0.018	0.798 ± 0.017	0.806 ± 0.022	0.797 ± 0.028	0.761 ± 0.027	0.745 ± 0.024	0.753 ± 0.021	0.726 ± 0.024
Overall Accuracy	10000	0.904 ± 0.008	0.892 ± 0.006	0.893 ± 0.006	0.883 ± 0.008	0.872 ± 0.009	0.844 ± 0.007	0.864 ± 0.006	0.819 ± 0.008

### 3.5.2 Variable Importance

The 31 variables tried were reduced to the 11 most important variables for each quadrangle. (Fig. 3.4). The variables that have the greatest contribution to model accuracy for the Pitts Point Quadrangle were the NTP, slope, slope radius 4 and 32; RT radius 200, 500, 1000, and 1500; roughness radius 100, dem std radius 250 and 500 (Fig. 3.4). The variables that have the greatest contribution to model accuracy for the De Mossville Quadrangle were the NTP, slope, slope radius 4, 8, and 16; RT radius 100, 500, and 1500, roughness radius 16; dem std radius 250 and 500.

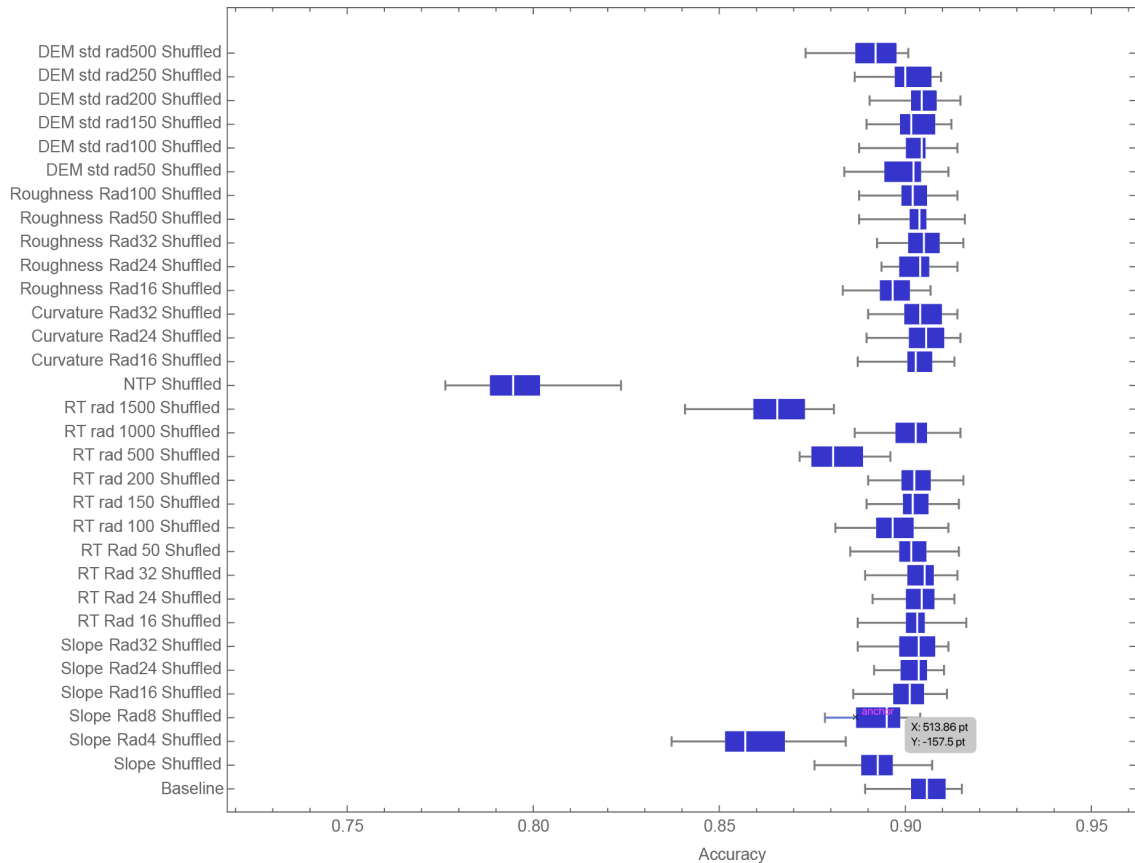


Figure 3.4. Box and whisker plot showing the mean and quartiles for the Gradient Boosted Trees model for the Pitts Point quadrangle, with each of 31 variables in the testing data perturbed in turn, and the resulting accuracy distribution. The variables that return the lowest accuracy are the most important to the classifier.

Once the 11 most important variables were identified, a new classifier was built using only these variables. A distribution of the resulting accuracies using just the important variables is compared with that from the original classifier in Figure 3.5. The mean accuracy using all variables for the Pitts Point and De Mossville Quadrangles is 0.921 and 0.903, respectively, and the mean accuracy by using just the most important

variables is 0.914 and 0.895. The loss of accuracy then is 0.007 and 0.008, respectively, or <1%.

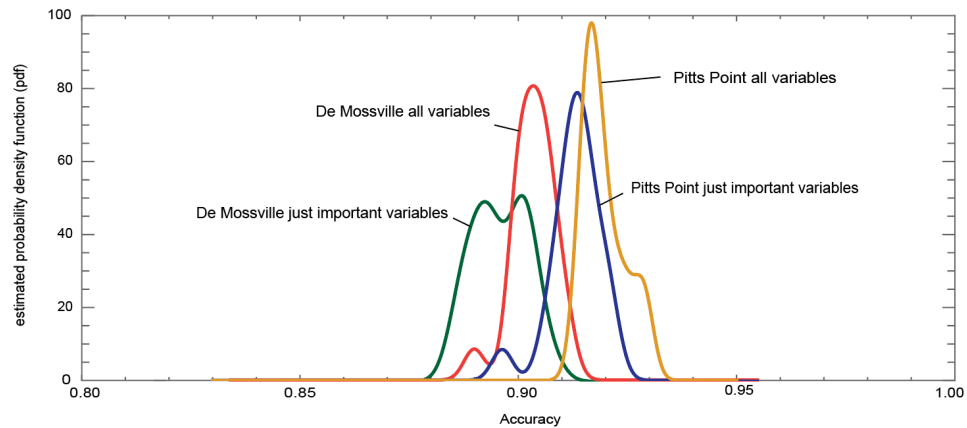


Figure 3.5. Accuracy distribution of the Gradient Boosted Trees model with the original 31 variables and with the 11 most important variables for the Pitts Point and De Mossville quadrangles.

### 3.5.3 Probability maps & F1 scores

The most accurate classifier (GBT) with the 11 most important variables was used to classify all cells in three 1.5 km x 1.5 km map areas for each quadrangle (Fig. 3.1) and a surficial geologic map was produced using the results. The overall accuracy and F1 scores for each geologic unit are presented in Tables 3.6 and 3.7, and the resulting probability maps are presented in Figures 3.6 to 3.9. For comparison, the worst classifier (NB) is also used to classify Map 1 for each quadrangle (Fig 3.6 and 3.8).

#### 3.5.3.1 Pitts Point

For the Pitts Point quadrangle, the overall accuracy in the training area is 0.921. This is reduced in Map 1 (just outside the training area) to 0.795 using the GBT classifier, and to 0.645 using the NB classifier. The overall accuracy for Map 2 (within the training area) is 0.911 and for Map 3 approximately 4.5 km away from the training area, it is 0.865. F1 scores are above 0.89 in all map areas for the colluvium and are lowest for the fill and alluvium. The F1 scores for most lithologies are higher in Map 2 than the other two map areas.

The best classifier (GBT) does an excellent job of mapping the colluvium in Map 1 (Fig. 3.6). The boundaries between the terraces and the colluvium are well-defined, and in the correct locations. The boundary between the lacustrine and alluvial terraces does not exactly match the boundary in the original map but is reasonably close. The classifier's accuracy is weakest where it misclassifies some of the residuum in the NE quadrant as alluvial terrace 4, and some of the alluvial terrace 4 as residuum in the SW quadrant. Some of these areas have lower probability values (shown as lighter colors). In

addition, some areas of the floodplain in the SE quadrant are mis-classified as alluvium, alluvial terrace, and fill. One feature not mapped in the original map, a roadway that trends NW/SE on the east side of the floodplain, was recognized by the classifier as fill.

The worst-performing classifier (NB) misclassifies the residuum and alluvial terrace 4 to a greater extent in Map 1, even showing a high probability for the incorrect classification for the alluvial terrace 4 in the SW quadrant, which it misclassifies as residuum. There are extensive areas of the floodplain that are misclassified as fill and alluvium. Much of the alluvial terrace 1&2 is mapped with low confidence or misclassified as lacustrine terrace.

The classifications in Map 2 from Pitts Point (Fig. 3.7) are much more accurate across the board. The delineation of the colluvium is excellent, and the boundary between the lacustrine and alluvial terraces is sharp and in the correct location. There is a small area where alluvial terrace 4 is incorrectly classified as residuum. While most of the floodplain and alluvium is accurately mapped, some of floodplain is misclassified as alluvium, and vice-versa. One of the alluvial fans (which are grouped together with alluvium for the classification) in the SW quadrant is mapped as alluvium, and the other is classified as a combination of colluvium and lacustrine terrace. The areas of fill in the NW quadrant are well identified. Two isolated remnants of lacustrine terrace preserved in the central area of the map are partially misclassified as fill.

In Map 3 from Pitts Point (Fig. 3.7), the boundary between the colluvium and residuum, and the residuum itself, is accurately delineated. The boundary of the lacustrine terrace and alluvium is correct in part of the map, but is misclassified as alluvium along its western edge. The areas of colluvium accumulation (which are grouped together as colluvium for the classification) are mapped as a splotchy combination of colluvium and alluvium. Fill is misclassified as alluvium and lacustrine terrace, and the heads of tributaries consisting of alluvium are misclassified as lacustrine terrace along the eastern edge of the map.

Table 3.6. F1 scores for each class and overall accuracy results for the maps in the Pitts Point Quadrangle.

Pitts Point Geologic Unit	F1 scores in training area	Map 1 (just outside training area)			Map 2 (within training area)		Map 3 (4.5 km distant)	
		# of samples	F1 score GBT	F1 score Naïve Bayes	# of samples	F1 score GBT	# of samples	F1 score GBT
Fill	0.449	1470	0.022	0.009	15439	0.700	10933	0.000
Floodplain	0.905	129278	0.624	0.375	109501	0.899	0	-
Alluvium	0.837	30504	0.402	0.199	70806	0.770	100549	0.585
Alluvial Terraces 1&2	0.916	149391	0.671	0.234	133296	0.888	0	-
Lacustrine Terraces 1&2	0.939	152551	0.780	0.663	256506	0.955	213565	0.874
Alluvial Terrace 4	0.881	8166	0.383	0.006	111024	0.953	0	-
Colluvium	0.948	426752	0.914	0.895	265195	0.919	656125	0.933
Residuum	0.943	101846	0.890	0.782	38197	0.898	18810	0.874
Overall Accuracy	0.921		0.795	0.645		0.911		0.865

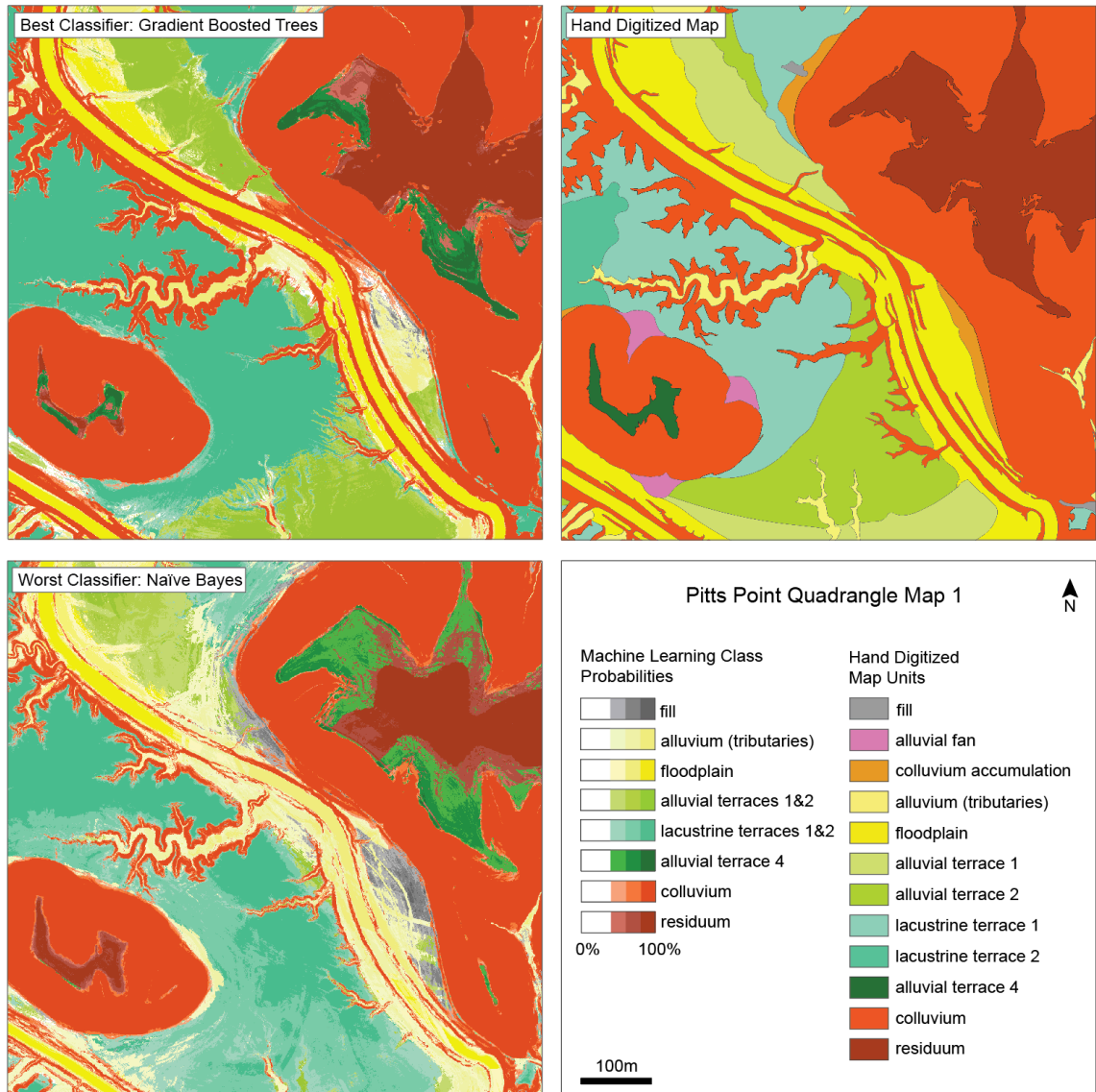


Figure 3.6. Map 1 in the Pitts Point quadrangle, which lies just outside of the training area (Fig. 3.1). The best-performing classifier (GBT) and worst performing classifier (Naïve Bayes) are compared with the hand digitized map.



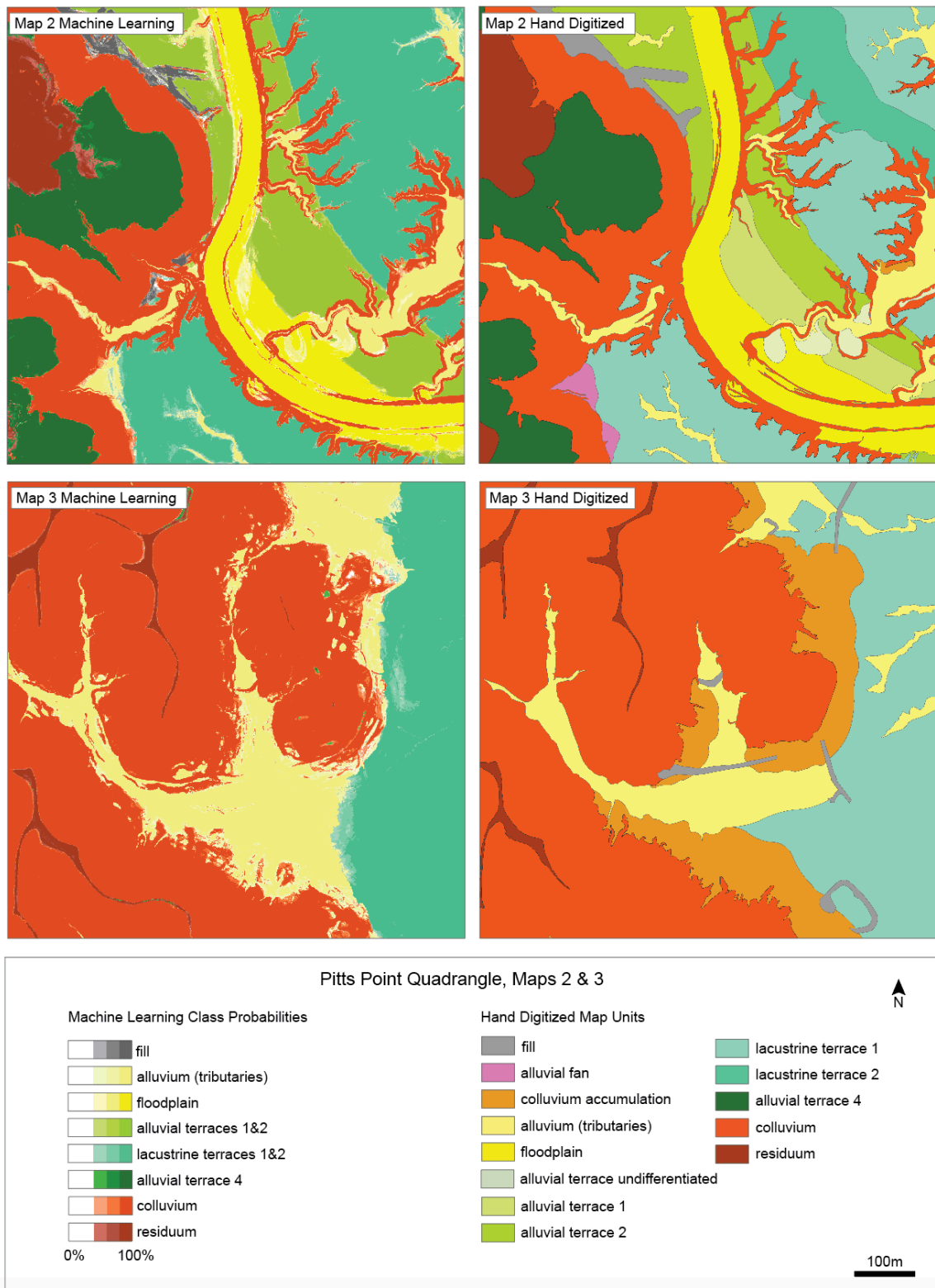


Figure 3.7. Maps 2 and 3 in the Pitts Point quadrangle, which lies within the training area, and 4.5 km away from the training area, respectively (Fig. 3.1).

### 3.5.3.2 De Mossville

For the De Mossville quadrangle, the overall accuracy in the training area is 0.898. For Map 1 (just outside the training area), this is reduced to 0.783 using the GBT classifier, and to 0.756 using the NB classifier. The overall accuracy for Map 2 (within the training area) is 0.881; and for Map 3, it is 0.931. F1 scores are above 0.87 in all map areas for the colluvium, and lowest for the fill and alluvium. The F1 scores for the residuum and colluvium are higher in Map 3 than the other two map areas. The F1 scores for the residuum and high-level alluvium are low for Map 1 using either classifier, and for Map 2.

Table 3.7. F1 scores for each class and overall accuracy results for the maps in the De Mossville Quadrangle.

Pitts Point Geologic Unit	F1 scores in training area	Map 1 (just outside training area)			Map 2 (within training area)		Map 3 (4.5 km distant)	
		# of samples	F1 score GBT	F1 score Naïve Bayes	# of samples	F1 score GBT	# of samples	F1 score GBT
Fill	0.255	43851	0.146	0.177	17626	0.181	13540	0.080
Alluvium	0.857	162757	0.881	0.812	173819	0.901	14400	0.369
Lacustrine & alluvial terraces	0.896	243511	0.799	0.767	248731	0.921	0	-
High-level alluvium	0.851	4437	0.000	0.000	27939	0.302	0	-
Colluvium	0.940	454821	0.891	0.875	492653	0.922	778603	0.963
Residuum	0.842	92573	0.403	0.595	39172	0.492	193540	0.878
Overall Accuracy	0.898		0.783	0.756		0.881		0.931

The probability maps for Map 1 show that the best classifier (GBT) does an excellent job of mapping the colluvium (Fig. 3.8). The boundaries between the terraces and the colluvium are quite sharp, and in the correct locations. The boundary between the terraces and the alluvium or colluvium are well-defined, save for the south-central map area where portions of the terrace are misclassified as alluvium and fill. The classifier is weakest on the ridgetops, where it misclassifies much of the residuum as high-level alluvium. In addition, the alluvial terrace 4 is also misclassified as high-level alluvium. Both the areas classified as residuum and high-level alluvium have significant areas where the probabilities are <0.80, and the boundary between residuum and colluvium appears gradational. Some of the areas of fill in the SW quadrant have been correctly classified, but larger areas of fill in the SE quadrant have not been classified correctly. Areas of colluvium accumulation in the NW quadrant have been incorrectly classified as

a combination of residuum and high-level alluvium. Overall, there is a lot of uncertainty in classifying the units for the NW quadrant of Map 1.

The worst-performing classifier (NB) also misclassifies the residuum, high-level alluvium, and alluvial terrace 4, though it maps as having a lower probability than the best classifier. The boundary between the terrace and colluvium which leads down to the alluvium is misclassified as fill throughout the map.

In Map 2 from the De Mossville quadrangle (Fig. 3.9), which is within the training area, the classifications are much more accurate overall than for Map 1. The delineation of the colluvium and terraces are well defined and in the correct location. Some of the high-level alluvium along the eastern edge of the map has been correctly classified, but some has been misclassified as residuum. Residuum along the ridgetops has a gradational contact with the colluvium. An area of residuum adjacent to the tributary stream has been misclassified as a terrace. Some of the fill has been correctly classified, particularly in the NE quadrant along the ridgetops and colluvial valleys but was not recognized within the terrace area.

In Map 3 from De Mossville (Fig. 3.9), the boundary between the colluvium and residuum, and the residuum itself, are quite close to the original map, though the ends of the ridges have a lower probability of being residuum, and grade into the colluvium. In one valley in the SW quadrant, the alluvium in the valley bottom is not recognized by the classifier. Areas of fill within the colluvial valleys are correctly classified but fill along ridgetops is not, and there are some areas that are classified as fill but were not included on the original map. There are a few small areas along the ridgetops that are incorrectly classified as high-level alluvium.

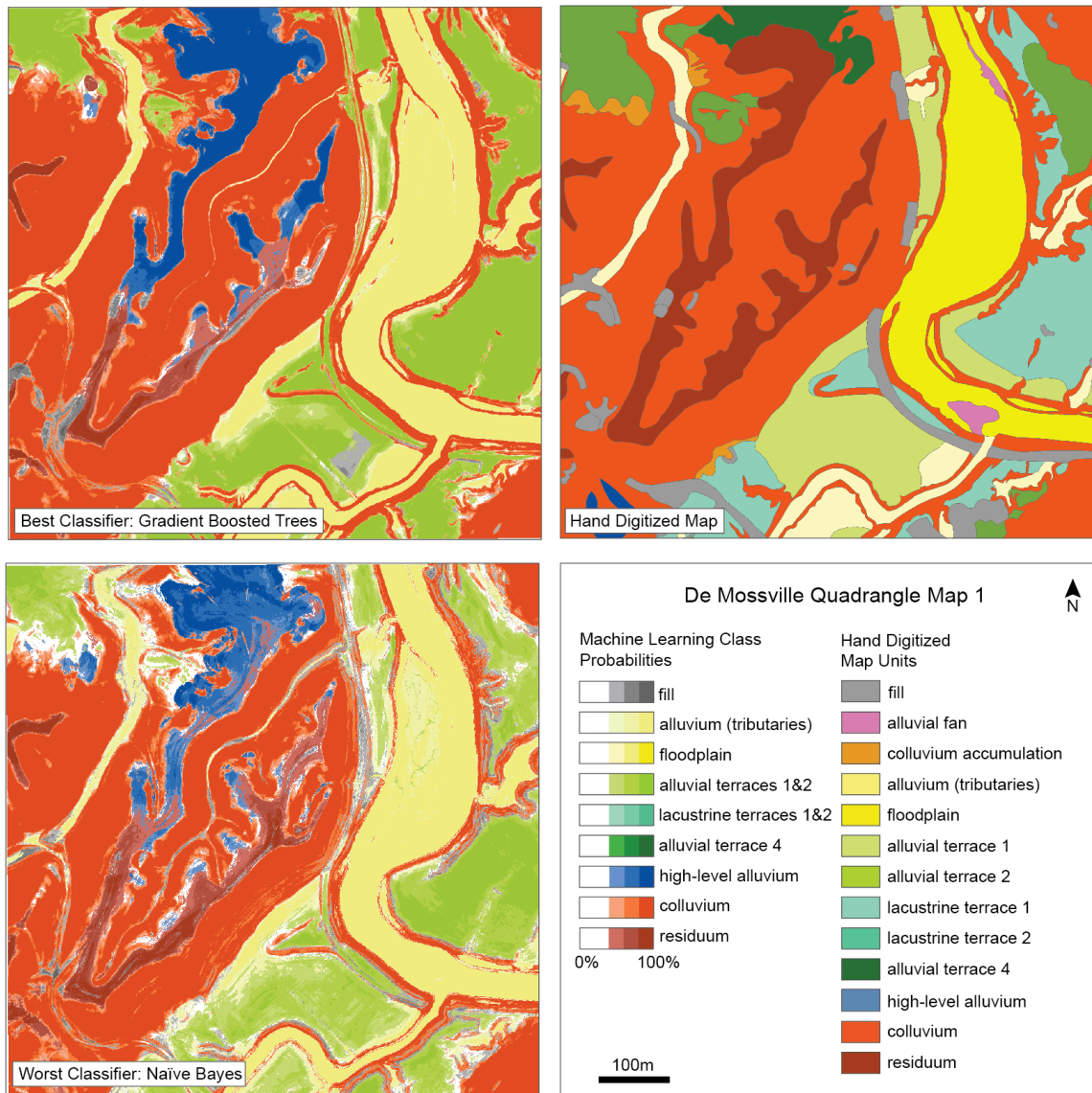


Figure 3.8. Map 1 in the De Mossville quadrangle, which lies just outside of the training area. The best-performing classifier (GBT) and worst performing classifier (Naïve Bayes) are compared with the hand digitized map.

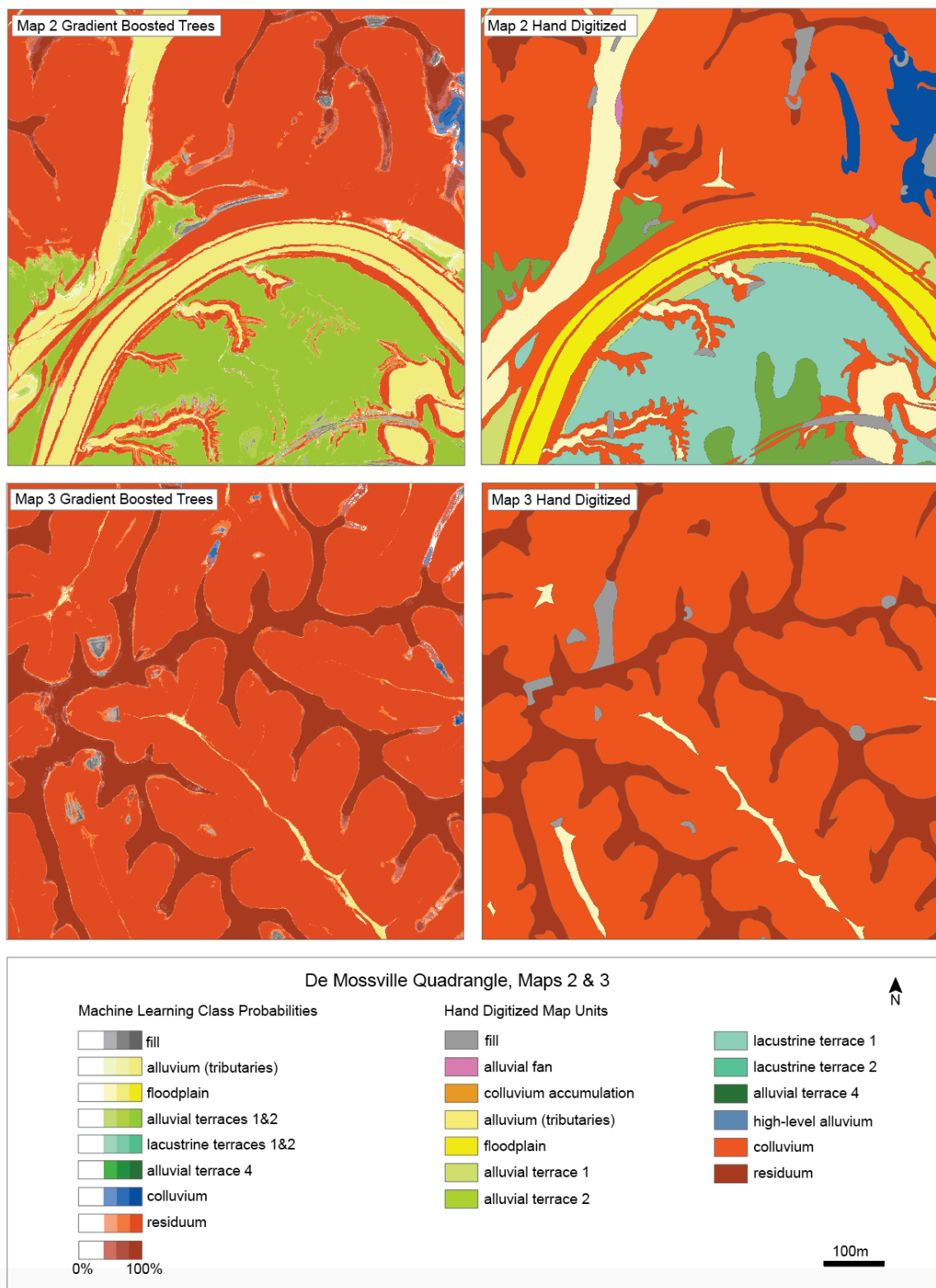


Figure 3.9. Maps 2 and 3 in the De Mossville quadrangle, which lies within the training area, and 6.0 km away from the training area, respectively (Fig. 3.1).

## 3.6 DISCUSSION

### 3.6.1 Model performance

The Gradient Boosted Trees model produced the classifier with the highest overall accuracy for each map area, and with some exceptions, the highest F1 score for each class. The Random Forest (RF) model produced the next-highest performing model. While GBT and the RF methods both utilize independent decision trees, GBT uses boosting to combine, or ensemble, individual trees in a sequence, while RF uses individual trees and combines them in parallel (Dhingra 2020). Ensemble methods have been shown to work well with sparse ground-truth data, and it gives robust estimates of the uncertainty of predicted lithology (Bergen et al. 2019; Kuhn, Cracknell, and Reading 2018). In GBT each decision tree is evaluated in terms of its loss, which is high when the classification and prediction do not agree, and each new tree corrects the errors of the previous tree. GBT can thus model more complex relationships and decision boundaries than a random forest model (Friedman 2001).

The Naïve Bayes model produced the classifier with the lowest overall accuracy for each map area, and with a few exceptions, the lowest F1 scores for each class. The Naïve Bayes model is a probabilistic method based on Bayes Theorem, which assumes that all the variables in the dataset are independent of each other, and do not affect each other (i.e. they are naïve). It is a simpler model than either of the ensemble methods described above. This type of model is often used for things like spam filtering and recommendation systems (Gandhi 2018). In this study, because the variables are not independent but correlate with each other (e.g. the terraces are at a lower elevation and have lower roughness than the residuum), this method did not perform as well as others.

### 3.6.2 Strengths and Limitations of Machine Learning

#### 3.6.2.1 Class imbalance

The selection of the training area from which the 10,000 points were randomly chosen influences the depiction or representation of each geologic unit, and also impacts the imbalance between the classes. While an effort was made to include archetypical areas of all map units in the training area, there is a preponderance of certain units. For example, in the Pitts Point and De Mossville quadrangles, 37% and 57% of the sample points, respectively, were colluvium. It is not surprising then that the colluvium had, with two exceptions, the highest F1 scores in all maps in both quadrangles (up to 0.933 and 0.963, respectively), with the lowest F1 score of 0.875 using the worst-performing classifier. This study did not attempt to map geologic units with only a small areal extent, such as the alluvial fans or colluvial accumulation areas, as these regions were not adequately represented in the training area data used to build the classifiers. A future study might include a different sampling strategy whereby the number of samples for each class are balanced. This might take the form of a series of key map areas with

exemplars of each class, instead of a single contiguous rectangular training area as used in the current study.

#### 3.6.2.2 Ease of classification

In addition to class imbalance having an impact on the ability of ML to correctly classify units, there may be some units that are easier to classify than others based on how unique their characteristics are in the topographic data. For example, colluvium is well recognized by ML, perhaps not only because it has the greatest representation in the training data, but also because it is found exclusively on slopes, as opposed to the units found on ridge tops or in the valleys. There is a persistent confusion between residuum and high-level alluvium and terrace deposits, which occupy a similar geomorphic position. It may be that distinguishing between these two deposits is beyond the capacity allowed by using just topographic information and may need additional data such as a description of the soil itself, or, as the high-level alluvium is related to the ancient Teays river system, information about the location of that system. That fill does not have high F1 scores in any map is not too surprising. While the naturally occurring surficial geologic units have a particular genesis that defines them, fill may be placed in a variety of locations that don't conform to a general origin, such as roads along ridgetops, terraces or slopes, dams in small valleys in the uplands or lowlands, and as the foundations for buildings and other infrastructure. However, there are still examples of locations where fill has been correctly identified, though perhaps with not a great degree of confidence, but a number of dams and roads are at least sketchily mapped in the correct locations (e.g., figs. 3.7 & 3.9)

#### 3.6.2.3 Topographic control

There is a strong correlation between elevation and the landforms, with residuum residing solely on ridgetops, lacustrine terraces in the valley, and so on. In addition, the ridges, as they are the remnants of a plateau, are confined to a small range of elevations. It would be informative to use this method in an area of more complex and varied terrain where the elevation does not have as clear a relationship with the surficial deposits.

### 3.6.3 ML performance inside and out of training area

Map areas within the training areas (Map 2 for both quadrangles) have an overall accuracy that is only slightly lower than that of the classifier, a drop of 0.010 and 0.017 for the Pitts Point, and De Mossville, respectively. The F1 scores for some units, such as the colluvium and terraces, are even higher than in the training area for both quadrangles. Map 3 in both quadrangles lies 4.5-6 km away from the training area and has a relatively simple geology. The overall accuracy is just 0.056 lower than the classifier for the Pitts Point quadrangle, and 0.033 higher than the classifier for the De Mossville quadrangle. Map 3 from the De Mossville quadrangle has a very high F1 score for colluvium of 0.963, and residuum, of 0.878. These somewhat overshadow the fact that the alluvium has a much lower F1 score of 0.369. Map 1 in both quadrangles lies just outside of the

training area and has a more complex geology than Map 3. There is a 0.126 and 0.115 drop for the Pitts Point and De Mossville quadrangles, respectively, using the GBT classifier. There is a corresponding drop in all F1 scores for all units in Map 1 in the De Mossville quadrangle, and, with the exception of alluvium, a drop in all F1 scores for Map 1 in the Pitts Point quadrangle. This indicates that the classifier is being trained on samples that do not fully depict each class, suggesting a different training strategy might be useful. In the Pitts Point quadrangle, the main culprits appear to be the disagreement on the boundary between the lacustrine and alluvial terrace, and the confusion between residuum and alluvial terrace 4 on the ridgetops, and the misclassification of some of the floodplain as terrace, alluvium, and fill. In the De Mossville quadrangle, the main culprit is the misclassification of residuum as high-level alluvium. Then again, it may be that some of these areas of confusion or misclassification do in fact reflect actual geological uncertainty.

#### 3.6.4 Mapping uncertainty

An advantage of using ML for mapping is that it communicates uncertainty in any mapped unit, and eliminates boundary lines which have their own uncertainty issues (Lark et al. 2015). If a boundary between units is desired, the user could apply a threshold for which a boundary can be applied. In addition, it may be that the uncertainty itself is useful or may coincide with lithologic transitions of key geological importance (Cracknell and Reading 2013). For example, most of the maps in this study show a gradational boundary between the residuum and colluvium, and this might be useful for the user to know so that this uncertainty could be incorporated into their plan to evaluate a site for potential slope mitigation.

Areas of uncertainty may also point to areas of geologic complexity. For example, in Map 3 for the Pitts Point quad (Fig. 3.7), there are significant areas of colluvium accumulation, which in this study we have defined as colluvium. In these areas the ML model has classified this as a patchy combination of colluvium and alluvium. According to the Kentucky Geologic Map Service, colluvium accumulation zones consist of a combination of colluvium, alluvium, lacustrine deposits, alluvial terraces, and fans. Thus, the classifier has pointed to the multigenetic origins of these deposits.

#### 3.6.5 Can ML replace human mapping?

For some geologic units, such as the colluvium, ML appears to do an excellent job of classifying. There are extensive areas outside of the two quadrangles used in this study, where the geology is dominated by colluvium and residuum with some valley alluvium and fill. In these areas of simple geology, ML produced maps with overall accuracies of 86.5% to 93.1%. This work demonstrates the strong potential for ML to quickly create accurate surficial geologic maps in geologically simple areas that can closely match human mapping. In more complex areas, particularly where some units, such as terraces, are not well preserved, or there are high-level alluvial deposits on the ridgetops, additional information obtained in the field is necessary. In such areas ML



could not create an accurate map without additional human mapping but could instead provide a base map highlighting where areas of geologic uncertainty lie. There is also the potential for ML performance to be enhanced by including other data sets such as soil samples or well log data which could help in distinguishing these geologic units from one another.

### 3.6.6 Future directions

This study used supervised machine learning algorithms, which use human classifications of geologic units as their basis for measuring model performance. A future line of inquiry is to use unsupervised machine learning, in which no classifications are provided, and the algorithm defines its own classification model. Another line of inquiry is to train a classifier using samples which equally sample all geologic units, thereby eliminating class imbalance. This may allow smaller features like alluvial fans, and colluvial accumulation zones to be mapped. However, it may be that some of these features, as they are an amalgamation of multiple types of deposits, may not be classified very well in any case. This study relied solely on the digital elevation model and derivative maps. Other data derived from the original lidar data could potentially be used as variables, including lidar intensity, existing county soils maps, and imagery. Furthermore, there is the potential for automatic feature selection from topographic data using a deep neural network (Kirkwood 2022).

## 3.7 CONCLUSIONS

This study demonstrates that machine learning can be a valuable tool for surficial geologic mapping. It can produce a near-final map in areas of simple geology, and a base map where the geology is more complex. A great benefit in using ML is that uncertainty for each geologic unit can be conveyed. This can be used to highlight areas where additional fieldwork is required, and also communicate to the end user the real geologic uncertainty between units. The Gradient Boosted Trees method produced the best performing classifier for both map areas tested. It produced very accurate maps of colluvium but had difficulty distinguishing between some units in the same topographic position such as residuum and high-level alluvial deposits. This method has the potential to be used in mapping any region where lidar data is available.

## 3.8 ACKNOWLEDGMENTS

We thank Max Hammond and Rachel Noble-Varney for their contributions to the preparation of this manuscript.

## REFERENCES

### References Chapter 1

- Adams, B. A., Whipple, K. X., Forte, A. M., Heimsath, A. M., & Hodges, K. V. (2020). Climate controls on erosion in tectonically active landscapes. *Science Advances*, 6(42), eaaz3166. <https://doi.org/10.1126/sciadv.aaz3166>
- Ardelean, A. C., Onaca, A., Urdea, P., & Sărășan, A. (2017). Quantifying postglacial sediment storage and denudation rates in a small alpine catchment of the Făgăraș Mountains (Romania). *Science of The Total Environment*, 599–600, 1756–1767. <https://doi.org/10.1016/j.scitotenv.2017.05.131>
- Ballantyne, C. K. (2013). Permafrost and periglacial features | Paraglacial Geomorphology. In *Encyclopedia of Quaternary Science* (pp. 553–565). Elsevier. <https://doi.org/10.1016/B978-0-444-53643-3.00089-3>
- Binnie, S. A., & Summerfield, M. A. (2013). 7.6 Rates of Denudation. In *Treatise on Geomorphology* (pp. 66–72). Elsevier. <https://doi.org/10.1016/B978-0-12-374739-6.00149-4>
- Brocklehurst, S. H., & Whipple, K. X. (2007). Response of glacial landscapes to spatial variations in rock uplift rate. *Journal of Geophysical Research*, 112(F2), F02035. <https://doi.org/10.1029/2006JF000667>
- Brown, S. J., Thigpen, J. R., Spotila, J. A., Krugh, W. C., Tranel, L. M., & Orme, D. A. (2017). Onset Timing and Slip History of the Teton Fault, Wyoming: A Multidisciplinary Reevaluation: Timing of Onset of the Teton Fault. *Tectonics*, 36(11), 2669–2692. <https://doi.org/10.1002/2016TC004462>
- Church, M., & Ryder, J. M. (1972). Paraglacial Sedimentation: A Consideration of Fluvial Processes Conditioned by Glaciation. *Geological Society of America Bulletin*, 83(10), 3059. [https://doi.org/10.1130/0016-7606\(1972\)83\[3059:PSACOF\]2.0.CO;2](https://doi.org/10.1130/0016-7606(1972)83[3059:PSACOF]2.0.CO;2)
- Deal, E., & Prasicek, G. (2021). The Sliding Ice Incision Model: A New Approach to Understanding Glacial Landscape Evolution. *Geophysical Research Letters*, 48(1). <https://doi.org/10.1029/2020GL089263>
- Dietsch, C., Dortch, J. M., Reynhout, S. A., Owen, L. A., & Caffee, M. W. (2015). Very slow erosion rates and landscape preservation across the southwestern slope of the Ladakh Range, India. *Earth Surface Processes and Landforms*, 40(3), 389–402. <https://doi.org/10.1002/esp.3640>
- Dortch, J. M., Owen, L. A., Schoenbohm, L. M., & Caffee, M. W. (2011). Asymmetrical erosion and morphological development of the central Ladakh Range, northern India. *Geomorphology*, 135(1–2), 167–180. <https://doi.org/10.1016/j.geomorph.2011.08.014>

- DuRoss, C. B., Gold, R. D., Briggs, R. W., Delano, J. E., Ostenaar, D. A., Zellman, M. S., Cholewinski, N., Wittke, S. J., & Mahan, S. A. (2019). Holocene earthquake history and slip rate of the southern Teton fault, Wyoming, USA. *GSA Bulletin*. <https://doi.org/10.1130/B35363.1>
- Egholm, D. L., Nielsen, S. B., Pedersen, V. K., & Lesemann, J.-E. (2009). Glacial effects limiting mountain height. *Nature*, 460(7257), 884–887. <https://doi.org/10.1038/nature08263>
- Fame, M. L., Owen, L. A., Spotila, J. A., Dortch, J. M., & Caffee, M. W. (2018). Tracking paraglacial sediment with cosmogenic  $^{10}\text{Be}$  using an example from the northwest Scottish Highlands. *Quaternary Science Reviews*, 182, 20–36. <https://doi.org/10.1016/j.quascirev.2017.12.017>
- Foster, D., Brocklehurst, S. H., & Gawthorpe, R. L. (2010). Glacial-topographic interactions in the Teton Range, Wyoming. *Journal of Geophysical Research*, 115(F1). <https://doi.org/10.1029/2008JF001135>
- Frings, R. M., Schüttrumpf, H., & Vollmer, S. (2011). Verification of porosity predictors for fluvial sand-gravel deposits: Porosity Prediction. *Water Resources Research*, 47(7). <https://doi.org/10.1029/2010WR009690>
- Good, J. E. G., & Pierce, K. L. (2016). *Interpreting the Landscapes of Grand Teton and Yellowstone National Parks: Recent and Ongoing Geology*. Grand Teton National History.
- Harbor, J. (1992). Numerical modeling of the development of U-shaped valleys by glacial erosion. *Geological Society of America Bulletin*, 12.
- Hauck, C., Böttcher, M., & Maurer, H. (2011). A new model for estimating subsurface ice content based on combined electrical and seismic data sets. *The Cryosphere*, 5(2), 453–468. <https://doi.org/10.5194/tc-5-453-2011>
- Herman, F., & Braun, J. (2008). Evolution of the glacial landscape of the Southern Alps of New Zealand: Insights from a glacial erosion model. *Journal of Geophysical Research*, 113(F2), F02009. <https://doi.org/10.1029/2007JF000807>
- Herman, F., De Doncker, F., Delaney, I., Prasicek, G., & Koppes, M. (2021). The impact of glaciers on mountain erosion. *Nature Reviews Earth & Environment*, 2(6), 422–435. <https://doi.org/10.1038/s43017-021-00165-9>
- Hobley, D. E. J., Sinclair, H. D., & Cowie, P. A. (2010). Processes, rates, and time scales of fluvial response in an ancient postglacial landscape of the northwest Indian Himalaya. *Geological Society of America Bulletin*, 122(9–10), 1569–1584. <https://doi.org/10.1130/B30048.1>

- Kilfeather, A. A., & van der Meer, J. J. M. (2008). Pore size, shape and connectivity in tills and their relationship to deformation processes. *Quaternary Science Reviews*, 27(3–4), 250–266. <https://doi.org/10.1016/j.quascirev.2006.12.015>
- Kindinger, J. G., Davis, J. B., & Flocks, J. G. (1994). *High-resolution single-channel seismic reflection surveys of Orange Lake and other selected sites of north central Florida* (Report No. 94–616; Open-File Report). USGS Publications Warehouse. <https://doi.org/10.3133/ofr94616>
- Koppes, M. N., & Montgomery, D. R. (2009). The relative efficacy of fluvial and glacial erosion over modern to orogenic timescales. *Nature Geoscience*, 2(9), 644–647. <https://doi.org/10.1038/ngeo616>
- Korup, O., & Montgomery, D. R. (2008). Tibetan plateau river incision inhibited by glacial stabilization of the Tsangpo gorge. *Nature*, 455(7214), 786–789. <https://doi.org/10.1038/nature07322>
- Leith, K., Moore, J. R., Amann, F., & Loew, S. (2014). Subglacial extensional fracture development and implications for Alpine Valley evolution: *Journal of Geophysical Research: Earth Surface*, 119(1), 62–81. <https://doi.org/10.1002/2012JF002691>
- Leopold, L. B., Wolman, M. G., & Miller, J. P. (1964). *Fluvial Processes in Geomorphology*. W. H. Freeman & Co.
- Love, J. D., Reed, J. C., & Christiansen, A. C. (1992). *Geologic Map of Grand Teton National Park, Teton County, Wyoming* (Map I-2031) [Map]. USGS.
- Mitchell, S. G., & Montgomery, D. R. (2006). Influence of a glacial buzzsaw on the height and morphology of the Cascade Range in central Washington State, USA. *Quaternary Research*, 65(1), 96–107. <https://doi.org/10.1016/j.yqres.2005.08.018>
- Moon, S., Page Chamberlain, C., Blisniuk, K., Levine, N., Rood, D. H., & Hilley, G. E. (2011). Climatic control of denudation in the deglaciated landscape of the Washington Cascades. *Nature Geoscience*, 4(7), 469–473. <https://doi.org/10.1038/ngeo1159>
- Norton, K. P., Abbühl, L. M., & Schlunegger, F. (2010). Glacial conditioning as an erosional driving force in the Central Alps. *Geology*, 38(7), 655–658. <https://doi.org/10.1130/G31102.1>
- Otto, J.-C., Schrott, L., Jaboyedoff, M., & Dikau, R. (2009). Quantifying sediment storage in a high alpine valley (Turtmanntal, Switzerland). *Earth Surface Processes and Landforms*, 34(13), 1726–1742. <https://doi.org/10.1002/esp.1856>
- Pedersen, V. K., & Egholm, D. L. (2013). Glaciations in response to climate variations preconditioned by evolving topography. *Nature*, 493(7431), 206–210. <https://doi.org/10.1038/nature11786>

Pierce, K. L., Licciardi, J. M., Good, J. M., & Jaworowski, C. (2018). *Pleistocene glaciation of the Jackson Hole Area, Wyoming* (Report No. 1835; Professional Paper, p. 68). USGS Publications Warehouse. <http://pubs.er.usgs.gov/publication/pp1835>

Rasbold, G. G., Pinheiro, U., Domingos-Luz, L., Dilworth, J., Thigpen, J. R., Pessenda, L. C. R., & McGlue, M. M. (2022). First evidence of an extant freshwater sponge fauna in Jackson Lake, Grand Teton National Park, Wyoming (USA). *Inland Waters*, 1–33. <https://doi.org/10.1080/20442041.2022.2035190>

Sass, O., & Wollny, K. (2001). Investigations regarding Alpine talus slopes using ground-penetrating radar (GPR) in the Bavarian Alps, Germany. *Earth Surface Processes and Landforms*, 26(10), 1071–1086. <https://doi.org/10.1002/esp.254>

Schrott, L., Hufschmidt, G., Hankammer, M., Hoffmann, T., & Dikau, R. (2003). Spatial distribution of sediment storage types and quantification of valley fill deposits in an alpine basin, Reintal, Bavarian Alps, Germany. *Geomorphology*, 55(1–4), 45–63. [https://doi.org/10.1016/S0169-555X\(03\)00131-4](https://doi.org/10.1016/S0169-555X(03)00131-4)

Spotila, J. A. (2022). Glacially-Influenced Tectonic Geomorphology: The Impact of Glacial Erosion on Topography and Orogenic Systems. In *Treatise on Geomorphology* (pp. 671–694). Elsevier. <https://doi.org/10.1016/B978-0-12-818234-5.00116-4>

Thigpen, R., Brown, S. J., Helfrich, A. L., Hoar, R., McGlue, M., Woolery, E., Guenther, W. R., Swallom, M. L., Dixon, S., & Gallen, S. (2021). Removal of the Northern Paleo-Teton Range along the Yellowstone Hotspot Track. *Lithosphere*, 2021(1), 1052819. <https://doi.org/10.2113/2021/1052819>

Tomkin, J. H. (2009). Numerically simulating alpine landscapes: The geomorphologic consequences of incorporating glacial erosion in surface process models. *Geomorphology*, 103(2), 180–188. <https://doi.org/10.1016/j.geomorph.2008.04.021>

Tranel, L. M., Spotila, J. A., Binnie, S. A., & Freeman, S. P. H. T. (2015). Quantifying variable erosion rates to understand the coupling of surface processes in the Teton Range, Wyoming. *Geomorphology*, 228, 409–420. <https://doi.org/10.1016/j.geomorph.2014.08.018>

Tranel, L. M., Spotila, J. A., Kowalewski, M. J., & Waller, C. M. (2011). Spatial variation of erosion in a small, glaciated basin in the Teton Range, Wyoming, based on detrital apatite (U-Th)/He thermochronology: Spatial variation of erosion in a small, glaciated basin in the Teton Range, Wyoming. *Basin Research*, 23(5), 571–590. <https://doi.org/10.1111/j.1365-2117.2011.00502.x>

Tunncliffe, J. F., & Church, M. (2011). Scale variation of post-glacial sediment yield in Chilliwack Valley, British Columbia. *Earth Surface Processes and Landforms*, 36(2), 229–243. <https://doi.org/10.1002/esp.2093>

Whipple, K. X. (2009). The influence of climate on the tectonic evolution of mountain belts. *Nature Geoscience*, 2(2), 97–104. <https://doi.org/10.1038/ngeo413>

Whipple, K. X., DiBiase, R. A., & Crosby, B. T. (2013). 9.28 Bedrock Rivers. In *Treatise on Geomorphology* (pp. 550–573). Elsevier. <https://doi.org/10.1016/B978-0-12-374739-6.00254-2>

Whipple, K. X., Kirby, E., & Brocklehurst, S. H. (1999). Geomorphic limits to climate-induced increases in topographic relief. *Nature*, 401(6748), 39–43. <https://doi.org/10.1038/43375>

Whipple, K. X., & Tucker, G. E. (1999). Dynamics of the stream-power river incision model: Implications for height limits of mountain ranges, landscape response timescales, and research needs. *Journal of Geophysical Research: Solid Earth*, 104(B8), 17661–17674. <https://doi.org/10.1029/1999JB900120>

Whitlock, C. (1993). Postglacial Vegetation and Climate of Grand Teton and Southern Yellowstone National Parks. *Ecological Monographs*, 63(2), 27.

Zhu, Y., Dortch, J. M., Massey, M. A., Haneberg, W. C., & Curl, D. (2021). An intelligent swath tool to characterize complex topographic features: Theory and application in the Teton Range, Licking River, and Olympus Mons. *Geomorphology*, 387, 107778. <https://doi.org/10.1016/j.geomorph.2021.107778>

## References Chapter 2

Baum, R.L. 1994. *Contribution of Artesian Water to Progressive Failure of the Upper Part of the Delhi Pike Landslide Complex, Cincinnati, Ohio*. Report **2059D** U.S. Geological Survey Bulletin, <https://doi.org/10.3133/b2059D>.

Baum, R.L. and Johnson, A.M. 1996. *Overview of Landslide Problems, Research, and Mitigation, Cincinnati, Ohio, Area*. Report **2059A** U.S. Geological Survey Bulletin, <https://doi.org/10.3133/b2059A>.

Birge, R.T. 1939. The Propagation of Errors. *American Journal of Physics*, 7, 351–357, <https://doi.org/10.1119/1.1991484>.

Brasington, J., Rumsby, B.T. and Mcvey, R.A. 2000. Monitoring and modeling morphological change in a braided gravel-bed river using high resolution GPS-based survey. *Earth Surface Processes and Landforms*, 25, 973–990.

Burns, W.J., Calhoun, N.C., Franczyk, J.J., Koss, E.J. and Bordan, M.G. 2017. Estimating losses from landslides in Oregon. In: *Landslides: Putting Experience, Knowledge and Emerging Technologies into Practice: De Graff, Jerome V. and Shakoor, Abdul (Eds.)* – 3rd North American Symposium on Landslides. 994.

Carlisle, B.H. 2005. Modelling the Spatial Distribution of DEM Error. *Transactions in GIS*, 9, 521–540, <https://doi.org/10.1111/j.1467-9671.2005.00233.x>.

Chau, K.T. 1999. Onset of natural terrain landslides modelled by linear stability analysis of creeping slopes with a two-state variable friction law. *International Journal for Numerical and Analytical Methods in Geomechanics*, **23**, 1835–1855, [https://doi.org/10.1002/\(SICI\)1096-9853\(19991225\)23:15<1835::AID-NAG2>3.0.CO;2-2](https://doi.org/10.1002/(SICI)1096-9853(19991225)23:15<1835::AID-NAG2>3.0.CO;2-2).

City of Cincinnati Transportation and Engineering. 2019. *2019 Columbia Parkway Landslide Evaluation and Report*.

Clapuyt, F., Vanacker, V. and Van Oost, K. 2016. Reproducibility of UAV-based earth topography reconstructions based on Structure-from-Motion algorithms. *Geomorphology*, **260**, 4–15, <https://doi.org/10.1016/j.geomorph.2015.05.011>.

Coe, J.A., Bessette-Kirton, E.K. and Geertsema, M. 2018. Increasing rock-avalanche size and mobility in Glacier Bay National Park and Preserve, Alaska detected from 1984 to 2016 Landsat imagery. *Landslides*, **15**, 393–407, <https://doi.org/10.1007/s10346-017-0879-7>.

Cook, K.L. 2017. An evaluation of the effectiveness of low-cost UAVs and structure from motion for geomorphic change detection. *Geomorphology*, **278**, 195–208, <https://doi.org/10.1016/j.geomorph.2016.11.009>.

Crawford, M.M. 2012. Using LiDAR to Map Landslides in Kenton and Campbell Counties, Kentucky. *Kentucky Geological Survey Report of Investigations 24 Series XII*, 18, <https://doi.org/10.13023/kgs.ri24.12>.

Crawford, M.M. 2014. Kentucky Geological Survey Landslide Inventory: From Design to Application. 22.

Crawford, M.M. and Bryson, L.S. 2018. Assessment of active landslides using field electrical measurements. *Engineering Geology*, **233**, 146–159, <https://doi.org/10.1016/j.enggeo.2017.11.012>.

EPA. 2016. What Climate Change Means for Ohio.

Fleming, R. and Johnson, A. 1994. *Landslides in Colluvium*. Report **2059B** U.S. Geological Survey Bulletin, <https://doi.org/10.3133/b2059B>.

Fleming, R. and Taylor, F. 1980. *Estimating the Costs of Landslide Damage in the United States*. Circular **832** Geological Survey Circular.

Froude, M.J. and Petley, D.N. 2018. Global fatal landslide occurrence from 2004 to 2016. *Natural Hazards and Earth System Sciences*, **18**, 2161–2181, <https://doi.org/10.5194/nhess-18-2161-2018>.

Glassmeyer, M.P. and Shakoor, A. 2021. Factors Contributing to Landslide Susceptibility of the Kope Formation, Cincinnati, Ohio. *Environmental and Engineering Geoscience*, **27**, 307–318, <https://doi.org/10.2113/EEG-D-20-00077>.



- Goetz, J., Brenning, A., Marcer, M. and Bodin, X. 2018. Modeling the precision of structure-from-motion multi-view stereo digital elevation models from repeated close-range aerial surveys. *Remote Sensing of Environment*, **210**, 208–216, <https://doi.org/10.1016/j.rse.2018.03.013>.
- Gonga-Saholiariliva, N., Gunnell, Y., Petit, C. and Mering, C. 2011. Techniques for quantifying the accuracy of gridded elevation models and for mapping uncertainty in digital terrain analysis. *Progress in Physical Geography: Earth and Environment*, **35**, 739–764, <https://doi.org/10.1177/0309133311409086>.
- Handwerger, A.L., Huang, M.-H., Fielding, E.J., Booth, A.M. and Bürgmann, R. 2019. A shift from drought to extreme rainfall drives a stable landslide to catastrophic failure. *Scientific Reports*, **9**, 1569, <https://doi.org/10.1038/s41598-018-38300-0>.
- Haneberg, W.C. 1991. Observation and analysis of pore pressure fluctuations in a thin colluvium landslide complex near Cincinnati, Ohio. *Engineering Geology*, **31**, 159–184, [https://doi.org/10.1016/0013-7952\(91\)90004-5](https://doi.org/10.1016/0013-7952(91)90004-5).
- Haneberg, W.C. 2006. Effects of Digital Elevation Model Errors on Spatially Distributed Seismic Slope Stability Calculations: An Example from Seattle, Washington. *Environmental and Engineering Geoscience*, **12**, 247–260, <https://doi.org/10.2113/gsegeosci.12.3.247>.
- Haneberg, W.C. 2008. Elevation errors in a LIDAR digital elevation model of West Seattle and their effects on slope-stability calculations. In: *Landslides and Engineering Geology of the Seattle, Washington, Area*, [https://doi.org/10.1130/2008.4020\(03\)](https://doi.org/10.1130/2008.4020(03)).
- Haneberg, W.C. 2017. Insight from the statistics of nothing: estimating limits of change detection using inferred nochange areas in DEM difference maps and application to landslide hazard studies. In: American Geophysical Union Fall Meeting, New Orleans.
- Haneberg, W.C. 2018. Repeat AUV MBES Surveys for Deepwater Seafloor Change Detection. In: *Offshore Technology Conference – Offshore Technology Conference*, Houston, Texas, USA, <https://doi.org/10.4043/28738-MS>.
- Haneberg, W.C. and Gokce, A.O. 1994. *Rapid Water-Level Fluctuations in a Thin Colluvium Landslide West of Cincinnati, Ohio*. Report **2059–CU**. S. Geological Survey Bulletin, <https://doi.org/10.3133/b2059C>.
- Hildebrand, F.B. 1987. *Introduction to Numerical Analysis*, 2nd ed.
- Hinge, L., Gundorph, J., Ujang, U., Azri, S., Anton, F. and Abdul Rahman, A. 2019. Comparative analysis of 3D photogrammetry modeling software packages for drones survey. *The International Archives of the Photogrammetry, Remote Sensing and Spatial Information Sciences*, **XLII-4/W12**, 95–100, <https://doi.org/10.5194/isprs-archives-XLII-4-W12-95-2019>.

- Holmes, K.W., Chadwick, O.A. and Kyriakidis, P.C. 2000. Error in a USGS 30-meter digital elevation model and its impact on terrain modeling. *Journal of Hydrology*, **233**, 154–173, [https://doi.org/10.1016/S0022-1694\(00\)00229-8](https://doi.org/10.1016/S0022-1694(00)00229-8).
- Jaboyedoff, M., Oppikofer, T., Abellán, A., Derron, M.-H., Loye, A., Metzger, R. and Pedrazzini, A. 2012. Use of LIDAR in landslide investigations: a review. *Natural Hazards*, **61**, 5–28, <https://doi.org/10.1007/s11069-010-9634-2>.
- James, M.R., Robson, S. and Smith, M.W. 2017. 3-D uncertainty-based topographic change detection with structure-from-motion photogrammetry: precision maps for ground control and directly georeferenced surveys: 3-D uncertainty-based change detection for SfM surveys. *Earth Surface Processes and Landforms*, **42**, 1769–1788, <https://doi.org/10.1002/esp.4125>.
- Knight, C. 2021. 2 Years and \$17.6 million: Columbia Parkway landslide project completed. *Cincinnati Enquirer*.
- Koralegedara, N.H. and Maynard, J.B. 2017. Chemical, mineralogical and textural properties of the Kope Formation mudstones: How they affect its durability. *Engineering Geology*, **228**, 312–322, <https://doi.org/10.1016/j.enggeo.2017.08.025>.
- Lacroix, P., Dehecq, A. and Taïpe, E. 2020a. Irrigation-triggered landslides in a Peruvian desert caused by modern intensive farming. *Nature Geoscience*, **13**, 56–60, <https://doi.org/10.1038/s41561-019-0500-x>.
- Lacroix, P., Handwerger, A.L. and Bièvre, G. 2020b. Life and death of slow-moving landslides. *Nature Reviews Earth & Environment*, **1**, 404–419, <https://doi.org/10.1038/s43017-020-0072-8>.
- Lan, H., Zhao, X., et al. 2021. The cyclic expansion and contraction characteristics of a loess slope and implications for slope stability. *Scientific Reports*, **11**, 2250, <https://doi.org/10.1038/s41598-021-81821-4>.
- Lane, S.N., Westaway, R.M. and Murray Hicks, D. 2003. Estimation of erosion and deposition volumes in a large, gravel-bed, braided river using synoptic remote sensing. *Earth Surface Processes and Landforms*, **28**, 249–271, <https://doi.org/10.1002/esp.483>.
- Leshchinsky, B., Olsen, M.J., et al. 2017. Mitigating coastal landslide damage. *Science*, **357**, 981–982, <https://doi.org/10.1126/science.aao1722>.
- Mansour, M.F., Morgenstern, N.R. and Martin, C.D. 2011. Expected damage from displacement of slow-moving slides. *Landslides*, **8**, 117–131, <https://doi.org/10.1007/s10346-010-0227-7>.
- Mirus, B.B., Ebel, B.A., Mohr, C.H. and Zegre, N. 2017. Disturbance Hydrology: Preparing for an Increasingly Disturbed Future. *Water Resources Research*, **53**, 10007–10016, <https://doi.org/10.1002/2017WR021084>.

Nappo, N., Peduto, D., Mavrouli, O., van Westen, C.J. and Gullà, G. 2019. Slow-moving landslides interacting with the road network: Analysis of damage using ancillary data, in situ surveys and multi-source monitoring data. *Engineering Geology*, **260**, 105244, <https://doi.org/10.1016/j.enggeo.2019.105244>.

Okyay, U., Telling, J., Glennie, C.L. and Dietrich, W.E. 2019. Airborne lidar change detection: An overview of Earth sciences applications. *Earth-Science Reviews*, **198**, 102929, <https://doi.org/10.1016/j.earscirev.2019.102929>.

Olsen, M.J., Raugust, J.D., Roe, G.V., National Cooperative Highway Research Program, National Cooperative Highway Research Program Synthesis Program, Transportation Research Board, and National Academies of Sciences, Engineering, and Medicine. 2013. *Use of Advanced Geospatial Data, Tools, Technologies, and Information in Department of Transportation Projects*, <https://doi.org/10.17226/22539>.

Palmer, J. 2017. Creeping earth could hold secret to deadly landslides. *Nature*, **548**, 384–386, <https://doi.org/10.1038/548384a>.

Podobnikar, T. 2016. Combination of error characterization and spatial error model to improve quality of digital elevation models. In: *Proceedings of Spatial Accuracy 2016 – Spatial Accuracy 2016*. 241–248.

Qin, R., Tian, J. and Reinartz, P. 2016. 3D change detection – Approaches and applications. *ISPRS Journal of Photogrammetry and Remote Sensing*, **122**, 41–56, <https://doi.org/10.1016/j.isprsjprs.2016.09.013>.

Riestenberg, M.M. 1994. *Anchoring of Thin Colluvium by Roots of Sugar Maple and White Ash on Hillslopes in Cincinnati*. Report **2059E** U.S. Geological Survey Bulletin, <https://doi.org/10.3133/b2059E>.

Schaffrath, K.R., Belmont, P. and Wheaton, J.M. 2015. Landscape-scale geomorphic change detection: Quantifying spatially variable uncertainty and circumventing legacy data issues. *Geomorphology*, **250**, 334–348, <https://doi.org/10.1016/j.geomorph.2015.09.020>.

Schulz, W.H., Coe, J.A., Ricci, P.P., Smoczyk, G.M., Shurtleff, B.L. and Panosky, J. 2017. Landslide kinematics and their potential controls from hourly to decadal timescales: Insights from integrating ground-based InSAR measurements with structural maps and long-term monitoring data. *Geomorphology*, **285**, 121–136, <https://doi.org/10.1016/j.geomorph.2017.02.011>.

Sibson, R. 1981. A Brief Description of Natural Neighbor Interpolation. In: *V. Barnett (Ed.). Interpreting Multivariate Data*. 21–36.

Sparling, H. 2019. Columbia Parkway landslides: Is this a new normal? *Cincinnati Enquirer*.

- Tang, A.-M., Cui, Y.-J. and Barnel, N. 2008. Thermo-mechanical behaviour of a compacted swelling clay. *Géotechnique*, **58**, 45–54, <https://doi.org/10.1680/geot.2008.58.1.45>.
- Turner, D., Lucieer, A. and de Jong, S. 2015. Time Series Analysis of Landslide Dynamics Using an Unmanned Aerial Vehicle (UAV). *Remote Sensing*, **7**, 1736–1757, <https://doi.org/10.3390/rs70201736>.
- US Geological Survey. 2005. *Landslide Hazards – a National Threat*. **2005–3156**U.S. Geological Survey Fact Sheet.
- Varnes, D.J. 1978. Slope Movement Types and Processes. In: *Schuster, R.L. and Krizek, R.J., Eds., Landslides, Analysis and Control*. Transportation Research Board, Special Report No. 176, 11–33.
- Warrick, J.A., Ritchie, A.C., Adelman, G., Adelman, K. and Limber, P.W. 2017. New Techniques to Measure Cliff Change from Historical Oblique Aerial Photographs and Structure-from-Motion Photogrammetry. *Journal of Coastal Research*, **331**, 39–55, <https://doi.org/10.2112/JCOASTRES-D-16-00095.1>.
- Warrick, J.A., Ritchie, A.C., Schmidt, K.M., Reid, M.E. and Logan, J. 2019. Characterizing the catastrophic 2017 Mud Creek landslide, California, using repeat structure-from-motion (SfM) photogrammetry. *Landslides*, **16**, 1201–1219, <https://doi.org/10.1007/s10346-019-01160-4>.
- Wechsler, S.P. 2007. Uncertainties associated with digital elevation models for hydrologic applications: a review. *Hydrol. Earth Syst. Sci.*, **20**, <https://doi.org/10.5194/hess-11-1481-2007>.
- Wheaton, J.M., Brasington, J., Darby, S.E. and Sear, D.A. 2009. Accounting for uncertainty in DEMs from repeat topographic surveys: improved sediment budgets. *Earth Surface Processes and Landforms*, n/a-n/a, <https://doi.org/10.1002/esp.1886>.
- Xiong, L., Wang, G., Bao, Y., Zhou, X., Sun, X. and Zhao, R. 2018. Detectability of Repeated Airborne Laser Scanning for Mountain Landslide Monitoring. *Geosciences*, **8**, 469, <https://doi.org/10.3390/geosciences8120469>.
- Zekkos, D., Greenwood, W., Lynch, J., Manousakis, J., Athanasopoulos-Zekkos, A., Clark, M. and Saroglou, C. 2018. Lessons Learned from The Application of UAV-Enabled Structure-From-Motion Photogrammetry in Geotechnical Engineering. *International Journal of Geoengineering Case Histories*, **4**, 254–274, <https://doi.org/10.4417/IJGCH-04-04-03>.

### References Chapter 3

- Antonov, Anton. 2016. "Importance of Variables Investigation Guide." MathematicaForPrediction blog at GitHub. <https://github.com/antononcube/MathematicaForPrediction/blob/master/Documentation/Importance-of-variables-investigation-guide.pdf>.
- Baum, Rex L., and Arvid M. Johnson. 1996. "Overview of Landslide Problems, Research, and Mitigation, Cincinnati, Ohio, Area." Report 2059A. U.S. Geological Survey Bulletin. Washington, D.C. USGS Publications Warehouse. <https://doi.org/10.3133/b2059A>.
- Berg, Richard C., Kelsey E. MacCormack, and Hazen A.J. Russell. 2019. "Benefit-Cost Analysis for Building 3D Maps and Models." AER/AGS Special Report 112 8104. <https://doi.org/10.4095/299022>.
- Bergen, Karianne J., Paul A. Johnson, Maarten V. de Hoop, and Gregory C. Beroza. 2019. "Machine Learning for Data-Driven Discovery in Solid Earth Geoscience." *Science* 363 (6433): eaau0323. <https://doi.org/10.1126/science.aau0323>.
- Bernknopf, Richard L., David S. Brookshire, David R. Soller, Michael J. McKee, John F. Sutter, Johnathan C. Matti, and Russell H. Campbell. 1993. "Societal Value of Geologic Maps." Circular. U.S. Geological Survey Circular 1111.
- Bhagwat, Subhash B., and Viju C. Ipe. 2000. "Economic Benefits of Detailed Geologic Mapping to Kentucky." Special Report Special Report 3. Illinois State Geological Survey.
- Breiman, Leo. 2001. "Random Forests." *Machine Learning* 45 (1): 5–32. <https://doi.org/10.1023/A:1010933404324>.
- Cox, D. R. 1958. "The Regression Analysis of Binary Sequences." *Journal of the Royal Statistical Society. Series B (Methodological)* 20 (2): 215–42.
- Cracknell, Matthew J., and Anya M. Reading. 2013. "The Upside of Uncertainty: Identification of Lithology Contact Zones from Airborne Geophysics and Satellite Data Using Random Forests and Support Vector Machines." *GEOPHYSICS* 78 (3): WB113–26. <https://doi.org/10.1190/geo2012-0411.1>.
- . 2014. "Geological Mapping Using Remote Sensing Data: A Comparison of Five Machine Learning Algorithms, Their Response to Variations in the Spatial Distribution of Training Data and the Use of Explicit Spatial Information." *Computers & Geosciences* 63 (February): 22–33. <https://doi.org/10.1016/j.cageo.2013.10.008>.
- Crawford, Matthew M. 2012. "Using LiDAR to Map Landslides in Kenton and Campbell Counties, Kentucky." *Kentucky Geological Survey Report of Investigations 24 Series XII*, 18. <https://doi.org/10.13023/kgs.ri24.12>.

Crawford, Matthew M., Jason M. Dortch, Hudson J. Koch, Ashton A. Killen, Junfeng Zhu, Yichuan Zhu, Lindsey S. Bryson, and William C. Haneberg. 2021. "Using Landslide-Inventory Mapping for a Combined Bagged-Trees and Logistic-Regression Approach to Determining Landslide Susceptibility in Eastern Kentucky, USA." *Quarterly Journal of Engineering Geology and Hydrogeology* 54 (4): qjagh2020-177. <https://doi.org/10.1144/qjagh2020-177>.

De Reu, Jeroen, Jean Bourgeois, Machteld Bats, Ann Zwertvaegher, Vanessa Gelorini, Philippe De Smedt, Wei Chu, et al. 2013. "Application of the Topographic Position Index to Heterogeneous Landscapes." *Geomorphology* 186 (March): 39–49. <https://doi.org/10.1016/j.geomorph.2012.12.015>.

Derouin, Sarah. 2021. "Detailed Geologic Mapping Helps Identify Health Hazards." *Eos* 102 (July). <https://doi.org/10.1029/2021EO161039>.

Dhingra, Cheshta. 2020. "A Visual Guide to Gradient Boosted Trees." Towards Data Science. 2020. <https://towardsdatascience.com/a-visual-guide-to-gradient-boosted-trees-8d9ed578b33>.

Dou, Jie, Ali P. Yunus, Dieu Tien Bui, Abdelaziz Merghadi, Meheub Sahana, Zhongfan Zhu, Chi-Wen Chen, Khabat Khosravi, Yong Yang, and Binh Thai Pham. 2019. "Assessment of Advanced Random Forest and Decision Tree Algorithms for Modeling Rainfall-Induced Landslide Susceptibility in the Izu-Oshima Volcanic Island, Japan." *Science of The Total Environment* 662 (April): 332–46. <https://doi.org/10.1016/j.scitotenv.2019.01.221>.

Durrell, R.H. 1982. *A Recycled Landscape*. Cincinnati Museum of Natural History Popular Publication Series. Cincinnati Museum of Natural History. <https://books.google.com/books?id=Xc6btgAACAAJ>.

Forman, George, and Martin Scholz. 2010. "Apples-to-Apples in Cross-Validation Studies: Pitfalls in Classifier Performance Measurement." *SIGKDD Explor.* 12: 49–57.

Friedman, Jerome H. 2001. "Greedy Function Approximation: A Gradient Boosting Machine." *The Annals of Statistics* 29 (5): 1189–1232.

Gandhi, Rohith. 2018. "Naive Bayes Classifier." Towards Data Science. 2018. <https://towardsdatascience.com/naive-bayes-classifier-81d512f50a7c>.

Granger, D. E., and A.L. Smith. 1998. "Early Laurentide Glaciation and Creation of Ohio River Dated by Radioactive Decay of Cosmogenic Al-26 and Be-10 in Proglacial Sediments." In *Geological Society of America Abstracts with Programs*, v. 30, n. 7, p. 298. Vol. v. 30.

Grohmann, Carlos Henrique, Mike J. Smith, and Claudio Riccomini. 2011. "Multiscale Analysis of Topographic Surface Roughness in the Midland Valley, Scotland." *IEEE Transactions on Geoscience and Remote Sensing* 49 (4): 1200–1213. <https://doi.org/10.1109/TGRS.2010.2053546>.

GSA. 2022. “GSA Position Statement: The Value of Geologic Mapping.” The Geological Society of America.

[https://www.geosociety.org/GSA/Science\\_Policy/Position\\_Statements/Current\\_Statements/gsa/positions/position3.aspx](https://www.geosociety.org/GSA/Science_Policy/Position_Statements/Current_Statements/gsa/positions/position3.aspx).

Hammond, Maxwell, Matthew A. Massey, William Andrews, Steven L. Martin, and Antonia Bottoms. 2017. “Annual Workflow of the STATEMAP-Funded Digital Surficial Geologic Mapping Program at the Kentucky Geological Survey.” In , 291134. <https://doi.org/10.1130/abs/2017NE-291134>.

Haneberg, W.C., A.L. Creighton, E.W. Medely, and D.A. Jonas. 2005. “Use of LiDAR to Assess Slope Hazards at the Lihir Gold Mine, Papua New Guinea.” In *O. Hungr, R. Fell, R. Couture, and E. Eberhardt, Editors, Landslide Risk Management: Proceedings of International Conference on Landslide Risk Management*. Vol. Supplementary CD. Vancouver, Canada.

Johnson, S. E., W. C. Haneberg, L. S. Bryson, and M. M. Crawford. 2023. “Measuring Ground Surface Elevation Changes in a Slow-Moving Colluvial Landslide Using Combinations of Regional Airborne Lidar, UAV Lidar, and UAV Photogrammetric Surveys.” *Quarterly Journal of Engineering Geology and Hydrogeology*, February, qjgegh2022-078. <https://doi.org/10.1144/qjgegh2022-078>.

KGS. 2021. “Kentucky Geological Survey 2020-2021 Annual Report.” Annual Report. Lexington, Kentucky: University of Kentucky. <https://storymaps.arcgis.com/stories/5adadf024bef4e779dab2fcc1e0251eb>.

———. 2023. “Kentucky Geologic Map Service.” Kentucky Geological Survey. <https://kgs.uky.edu/kygeode/geomap/>.

Kirkwood, Charlie. 2022. “Geological Mapping in the Age of Artificial Intelligence.” *Geoscientist* 32 (3): 16–23. <https://doi.org/10.1144/geosci2022-023>.

Kirkwood, Charlie, Mark Cave, David Beamish, Stephen Grebby, and Antonio Ferreira. 2016. “A Machine Learning Approach to Geochemical Mapping.” *Journal of Geochemical Exploration* 167 (August): 49–61. <https://doi.org/10.1016/j.gexplo.2016.05.003>.

Kirkwood, Charlie, Theo Economou, Nicolas Pugeault, and Henry Odbert. 2022. “Bayesian Deep Learning for Spatial Interpolation in the Presence of Auxiliary Information.” *Mathematical Geosciences* 54 (3): 507–31. <https://doi.org/10.1007/s11004-021-09988-0>.

Kuhn, Stephen, Matthew J. Cracknell, and Anya M. Reading. 2018. “Lithologic Mapping Using Random Forests Applied to Geophysical and Remote-Sensing Data: A Demonstration Study from the Eastern Goldfields of Australia.” *GEOPHYSICS* 83 (4): B183–93. <https://doi.org/10.1190/geo2017-0590.1>.



Lark, R. M., R. S. Lawley, A. J. M. Barron, D. T. Aldiss, K. Ambrose, A. H. Cooper, J. R. Lee, and C. N. Waters. 2015. "Uncertainty in Mapped Geological Boundaries Held by a National Geological Survey:Eliciting the Geologists' Tacit Error Model." *Solid Earth* 6 (2): 727–45. <https://doi.org/10.5194/se-6-727-2015>.

Massey, M.A. 2017. "Surficial Geologic Map of the De Mossville 7.5-Minute Quadrangle, North-Central Kentucky (1:24,000)." Kentucky Geological Survey Contract Report 8-13, 1 Sheet. Kentucky Geological Survey.

Massey, M.A., M. III Hammond, A.E. Bottoms, and S.L. Martin. 2019. "Surficial Geologic Map of the Pitts Point 7.5-Minute Quadrangle, North-Central Kentucky (1:24,000)." Kentucky Geological Survey Contract Report 20-13, 1 Sheet. Kentucky Geological Survey.

"Mathematica." 2022. Mathematica. Champaign, Illinois: Wolfram Research, Inc. [www.wolfram.com/mathematica](http://www.wolfram.com/mathematica).

McDowell, Robert C. 1986. "The Geology of Kentucky - A Text to Accompany the Geologic Map of Kentucky." Professional Paper 1151-H. U.S. Geological Survey Professional Paper. USGS. <https://pubs.usgs.gov/pp/p1151h/about.html>.

Metelka, Václav, Lenka Baratoux, Mark W. Jessell, Andreas Barth, Josef Ježek, and Seta Naba. 2018. "Automated Regolith Landform Mapping Using Airborne Geophysics and Remote Sensing Data, Burkina Faso, West Africa." *Remote Sensing of Environment* 204 (January): 964–78. <https://doi.org/10.1016/j.rse.2017.08.004>.

Potter, Paul Edwin. 2007. "Exploring the Geology of the Cincinnati/ Northern Kentucky Region." *Kentucky Geological Survey*, Special Publication, Special Publication 8.

Smith, William. 1815. "A Delineation of the Strata of England and Wales, with Part of Scotland; Exhibiting the Collieries and Mines, the Marshes and Fen Lands Originally Overflowed by the Sea, and the Varieties of Soil According to the Variations in the Substrata, Illustrated by the Most Descriptive Names."

Weiss, Andrew D. 2001. "Topographic Position and Landforms Analysis." Presented at the ESRI User Conference, San Diego, CA.

Winchester, Simon. 2009. *The Map That Changed the World: William Smith and the Birth of Modern Geology*. Repr. New York, NY: Harper Perennial.

Zhu, Junfeng, and William P. Pierskalla. 2016. "Applying a Weighted Random Forests Method to Extract Karst Sinkholes from LiDAR Data." *Journal of Hydrology* 533 (February): 343–52. <https://doi.org/10.1016/j.jhydrol.2015.12.012>.

## VITA

Sarah E. Johnson

### EDUCATION

M.S., Geology, Purdue University, 1997, advisor: Arvid M. Johnson

B.S., summa cum *laude*, Geology, 1993, City College of New York

### PROFESSIONAL EXPERIENCE

**Senior Lecturer in Geology**, Northern Kentucky University, Department of Physics, Geology and Engineering Technology. 2002 – present

**Geology Program Director**, Northern Kentucky University, Department of Physics, Geology and Engineering Technology. 2018 – 2020

**Engineering Geologist**, H.C. Nutting (now Terracon), Cincinnati, 2000 – 2002

**Marine Geophysicist**, Schlumberger, Houston, TX, 1998 – 2000

### REFEREED PAPERS PUBLISHED

**Johnson, S.E.**, Haneberg, W. C, Crawford, M., Bryson, S., **2023**, Measuring ground surface elevation changes in a slow-moving colluvial landslide using combinations of regional airborne lidar, UAV lidar, and UAV photogrammetric surveys. *Quarterly Journal of Engineering Geology and Hydrogeology*. <https://doi.org/10.1144/qjegh2022-078>.

McGlue, M. M., Dilworth, J. R., Johnson, H. L., Whitehead, S. J., Thigpen, R., Yeager, K. M., Woolery, E. W., Brown, S. J., **Johnson, S. E.**, Cearley, C. S., Clark, G., Dixon, T. S., Goldsby, R., Helfrich, A. L., Hodelka, B. N., Lo, E. L., Domingos Luz, L., Powell, N. E., Rasbold, G. G., Swanger, W. R., 2023, Dam emplacement and water level changes affect sublacustrine geomorphology and recent sedimentation in Jackson Lake, Grand Teton National Park (Wyoming, USA), *Earth Systems Science and Society*, <https://doi.org/10.3389/esss.2023.10066>

**Johnson, S. E.**, Swallom, M. L., Thigpen, J. R., McGlue, M. M., Dortch, J. M., Gallen, S., Woolery, E. W., Yeager, K., 2022, The influence of glacial topography on fluvial efficiency in the Teton Range, Wyoming (USA). *Earth and Planetary Science Letters* 592 (117643), <https://doi.org/10.1016/j.epsl.2022.117643>

Haneberg, W.C., **Johnson, S.E.**, Gurung, N., 2021, Response of the Laprak, Nepal, landslide to the 2015 M<sub>w</sub> 7.8 Gorkha earthquake. *Natural Hazards* 111, 567-584, <https://doi.org/10.1007/s11069-021-05067-z>.

**Johnson, S.E.**, 1997, 1996 Tumalt Creek debris flows and debris avalanches in the Columbia River Gorge east of Portland, Oregon, in Chen, Cheng-lung, editor, *First International Conference on Debris-flow Hazards Mitigation; Mechanics, Prediction and Assessment*. American Society of Civil Engineers, New York, NY, 395-404.

#### PUBLISHED CONFERENCE ABSTRACTS

Goldsby, R., Swallow, M., Thigpen, R., **Johnson, S. E.**, Dortch, J., Brown, S., Woolery, E., McGlue, M., Yeager, K., 2022, Linking Teton and East Gallatin fault motion across the Yellowstone hotspot track, Wyoming USA: Implications for ongoing extension beneath Yellowstone and the northern continuation of the active Teton fault. *Geological Society of America Abstracts with Programs* (54)5, <https://doi.org/10.1130/abs/2022AM-381527>

Haneberg, W.C., **Johnson, S. E.**, Gurung, N., 2022, Laprak revisited: Understanding the response of a large Himalayan landslide to the 2015 Gorkha earthquake. *AEG News* 65(4), 74.

**Johnson, S. E.**, Haneberg, W.C., 2021, Elevation change detection thresholds in a slow-moving colluvium landslide in the Cincinnati area using combinations of regional LiDAR, structure from motion photogrammetry, and UAV-LiDAR. 2021 AGU Fall Meeting, abstract NH33A-09.

**Johnson, S.**, Swallow, M. L., Thigpen, J. R., McGlue, M. M., Woolery, E. W., Dortch, J., Gallen, S., Yeager, K. 2021, Post-glacial fluvial inefficiency. *Geological Society of America Abstracts with Programs* 53(6), <https://doi.org/10.1130/abs/2021AM-371378>

McGlue, M., Dilworth, J. R., Johnson, H., Yeager, K., Thigpen, J. R., Woolery, E. W., Brown, S. J., Cearley, C. S., Clark, G., Dixon, T. S., Goldsby, R., Helfrich, A. L., Hodelka, B. N., **Johnson, S.**, Domingos Luz, L., Powell, N. E., Rasbold, G. G., Swanger, W., Whitehead, S. J., 2021, Sublacustrine geomorphology and deepwater chemostratigraphy reveal effects of dam installation at Jackson Lake (Wyoming, USA). *Geological Society of America Abstracts with Programs* 53(6), <https://doi.org/10.1130/abs/2021AM-365379>

**Johnson, S.**, and Haneberg, W.C., 2020, Documenting decadal scale landslide movement using sequential LiDAR and structure from motion digital elevation models in the Cincinnati and Northern Kentucky metropolitan area. 2020 AGU Fall Meeting, abstract NH009-0004

**Johnson, S.**, Swallow, M., Thigpen, J. R., McGlue, M. M., and Woolery, E. W., 2020. A comparison of post-glacial sediment volumes from source to sink in Moran and

Snowshoe Canyons, Teton Range, Wyoming. *Geological Society of America Abstracts with Programs* 52(6), <https://doi.org/10.1130/abs/2020AM-356159>

Helfrich, A. L., Swallom, M., **Johnson, S.**, Thigpen, J. R., McGlue, M. M., Woolery, E. W., Brown, S. J., McQuarrie, N., 2019, Utilizing apatite (U-Th)/He analysis, landscape and kinematic modeling to examine the relative efficacy of climatic and tectonic forcing in an active tectonic system, Teton Range, WY. *Geological Society of America Abstracts with Programs* 51(5), <https://doi.org/10.1130/abs/2019AM-338520>

**Johnson, S.**, Thigpen, J. R., McGlue, M. M., Woolery, E.W., 2019. Preliminary quantification of sediment storage in Moran and Avalanche Canyons in Grand Teton National Park, Wyoming, USA. *Geological Society of America Abstracts with Programs* 51(3), <https://doi.org/10.1130/abs/2019SE-327584>

**Johnson, S.**, Edwards, T., Johnson, M., Brown, C., Peterson, C., 2018, Landslide inventory of Northern Kentucky using differential elevation maps derived from sequential LiDAR surveys. *Geological Society of America Abstracts with Programs* 50(6), <https://doi.org/10.1130/abs/2018AM-323773>

Roenker, B., Olson R., Faller, T., Ivey, Z., **Johnson, S.**, Wang, H., 2018, Using sequential LiDAR data to identify and landslides in Kenton and Campbell counties in Northern Kentucky, *Geological Society of America Abstracts with Programs* 50(3), <https://doi.org/10.1130/abs/2018SE-312623>

Haneberg, W. C., **Johnson, S.**, 2017, Double gaussian filtering to suppress noise and improve identification of new landslides on DEM difference maps. *Geological Society of America Abstracts with Programs* 49(6), <https://doi.org/10.1130/abs/2017AM-305313>

**Johnson, S.**, Olson R., Roenker, B., 2017, Using sequential LiDAR to monitor and catalog recently active landslides in Kenton and Campbell counties in Northern Kentucky. *Geological Society of America Abstracts with Programs* 49(6), <https://doi.org/10.1130/abs/2017AM-306512>

**Johnson, S.**, Amundsen, J.\*, 2011, Identification and delineation of previously unreported landslides in Cincinnati and Northern Kentucky using LiDAR-derived maps. *AEG News* 54 (Annual Meeting Program with Abstracts), p. 88.

Brackman, T., **Johnson, S.**, Rouse, K., Pullammanappallil, S., 2011, Using LiDAR and ReMi for location and delineation of landslides in northern Kentucky. *AEG News* 54 (Annual Meeting Program with Abstracts), p. 68.

Amundsen, J., **Johnson, S.**, 2009, Improving approximations of the Mohr-Coulomb failure envelope. *Geological Society of America Abstracts with Programs* 41(7), p. 673.

Engel N., **Johnson S.**, 2005, The Quaternary geology and geomorphology of Big Bone Lick State Park, Kentucky”, poster presented at the Geological Society of America National Meeting, Salt Lake City, UT. *Geological Society of America Abstracts with Programs* 37(7), p. 427.

**Johnson, S.**, Andrews, W.M., 2005, Inter-disciplinary cooperative investigations at Big Bone Lick State Park, northern Kentucky. *Geological Society of America Abstracts with Programs* 37(5), p.14.

#### OTHER PRESENTATIONS

**Johnson, S.**, and Haneberg, W.C., 2021. Documenting decadal scale landslide movement using sequential LiDAR and structure from motion digital elevation models in the Cincinnati and Northern Kentucky Metropolitan Area, poster presented at the Kentucky Geological Survey Annual Seminar, May 20, 2021.

Dortch, Jason M., Hammond, M., **Johnson, S.**, and Koch, H., 2021. LASTiff, what is it and why do I need it?, Kentucky Geological Survey Seminar Series, January 15, 2021.

**Johnson, S.** 2019. Using LiDAR, unmanned aerial vehicles and structure from motion to detect and monitor landslides in Kentucky. Presented at the Geoscience Alumni Research Symposium, University of Kentucky, October 3, 2019.

**Johnson, S.**, 2014 Coral Reefs: Exercises integrating geomorphology and sedimentary geology, Invited presentation at the National Association of Geoscience Teachers conference “Innovative Approaches to Teaching Sedimentary Geology, Geomorphology, and Paleontology”, June 16-20, 2014, St. Paul, MN.

**Johnson, S.**, 2011, Landslide detection using LiDAR, presentation for the AEG Ohio River Valley section meeting.

**Johnson, S.**, 2010, Tumalt Creek, Oregon debris flows revisited, invited speaker, University of Cincinnati Geology Colloquium Series, February, 2010.

#### ACADEMIC SCHOLARSHIPS & HONORS

2019-2021, University of Kentucky, KGS-EES Commonwealth Research Assistantship in Earth and Environmental Sciences

2020-2021 University of Kentucky, Earth & Environmental Sciences Department, Ferm grant in support of graduate research

2019-2021 University of Kentucky, Earth & Environmental Sciences Department Brown McFarland grant in support of graduate travel to professional meetings

1996 Michael C. Gardener Memorial Award, in support of graduate research

1996 Cedric J. Newby Scholarship, in support of graduate research

1996 Linda Horn Memorial Fund Scholarship, in support of graduate research

1993 Award for Best Calculus Final at City College of New York

1993 Undergraduate Teaching Assistantship, City College of New York

Phi Beta Kappa